Land Subsidence and Groundwater Level Changes in the Dickenson – La Marque Area, Galveston County, Texas During the Past Two Decades

by
Meghan Eileen DiBacco

A thesis submitted to the Department of Earth and Atmospheric Sciences,
College of Natural Science and Mathematics
in partial fulfillment of the requirements for the degree of

Master of Science
in Geophysics

Chair of Committee: Guoquan Wang

Committee Member: Juan Carlos Fernandez - Diaz

Committee Member: Jonny Wu

University of Houston
December 2020

DEDICATION

To my family.

ACKNOWLEDGMENTS

I would like to first express my gratitude to my committee for their patience and continuous involvement in my project. I would like to express my gratitude to my thesis advisor, Dr. Guoquan Wang, for his guidance and dedication to his research and students. Without his commitment, this project would not have been possible. Thank you as well to my committee members Dr. Jonny Wu and Dr. Juan Carlos Fernandez-Diaz for your continued involvement and insight into my project. The efforts of my committee improved not only the quality of this project but taught me valuable lessons along the way.

Thank you to the Harris-Galveston Subsidence District (HGSD), United States Geological Survey (USGS), and National Geodetic Survey (NGS) for providing the raw groundwater and geodetic data utilized for this study. The public availability of their data archives allows the scientific community to conduct important research. I hope that the research completed in this work will provide insight and aid in the efforts of a local organization to better understand linked subsidence and groundwater issues occurring in Houston.

Finally, to my parents David and Maryellen DiBacco for their unwavering love, patience, and support throughout the course of my research. My sister Kathleen thank you for all the support and words of encouragement. To all my family, friends, and fellow students that have helped me along, I cannot thank you enough.

ABSTRACT

Subsidence has plagued the greater Houston Galveston area and prompted the creation of the Houston Galveston Subsidence District (HGSD). Subsidence in the cities of Dickenson and La Marque, in Galveston County, Texas, was extremely rapid (several centimeters per year) during the 1960s and 1970s but has declined to a rate of less than 5 mm per year since the 1990s as a result of the groundwater regulations enforced by HGSD. The United States Geological Survey (USGS), HGSD, National Geodetic Survey (NGS), and the University of Houston (UH) have been continuously monitoring land subsidence and groundwater levels in this area since the 1970s.

This study investigated the long-period groundwater, extensometer, and GPS datasets and (1) delineated the regional groundwater heads, (2) studied the compaction and inflation of shallow aquifers, (3) studied the interaction of land subsidence and groundwater level changes in both short-term (days to seasonal) and long-term (several years to a decade), and (4) assessed the effectiveness of the groundwater regulations in the study area. According to this study, the ongoing subsidence rate derived from GPS observations in the area is below 5 mm per year. The regional preconsolidation heads of the Chicot and Evangeline aquifers are approximately at 30 meters below the land surface. The results of this study provide essential information for future urban development, utilization of groundwater resources, and the minimization of urban geological hazards, and guidelines for slowing and finally ceasing the ongoing moderate (a few millimeters per year) to rapid (a few centimeters per year) subsidence that is occurring in the western and northern parts of the Houston metropolitan region.

TABLE OF CONTENTS

LIST OF TABLES

LIST OF FIGURES

1. INTRODUCTION AND MOTIVATION

Subsidence occurs commonly in populated urban and industrial areas as a result of groundwater withdrawals for municipal, industrial, and irrigation use. The consequences of land subsidence include infrastructure damage, increased flood risk, induced faulting, and a reduction in the total aquifer storage. Presently, widespread subsidence occurs throughout most of the Greater Houston Galveston area, however, the mitigation of subsidence in the Dickenson La Marque area provides an ideal case study that will provide guidelines for slowing and ceasing the ongoing subsidence in the surrounding Houston area. The aforementioned consequences motivated this study, to investigate the relationship between ground deformation, specifically, groundwater levels, land rebound trends of shallow aquifers, and sediment compaction. The regional groundwater heads will be derived through this relationship. Additionally, this study will discuss the effectiveness of local groundwater regulations from the Harris Galveston Subsidence District (HGSD).

The Houston-Galveston region represents one of the largest areas of subsidence. This study more specifically looks at the Dickenson - La Marque area located 10 miles northwest of Galveston Island, next to Texas City in Galveston County, Texas as seen in Figure 1-1 (Coplin and Galloway, 1999). This area is a large bay-estuary-lagoon system comprised of the Trinity, Galveston, and the East and West bays which are separated from the Gulf of Mexico by Galveston Island and Bolivar Peninsula, allowing tidal exchanges through the barrier-island and peninsula complex (Coplin and Galloway, 1999). The area is underlain by sequences of unconsolidated fine grain sands and clays. Sediment in the area has an alluvial or deltaic origin, with some sediments that have been reworked by littoral currents to form beach deposits (Petitt and Winslow, 1957).

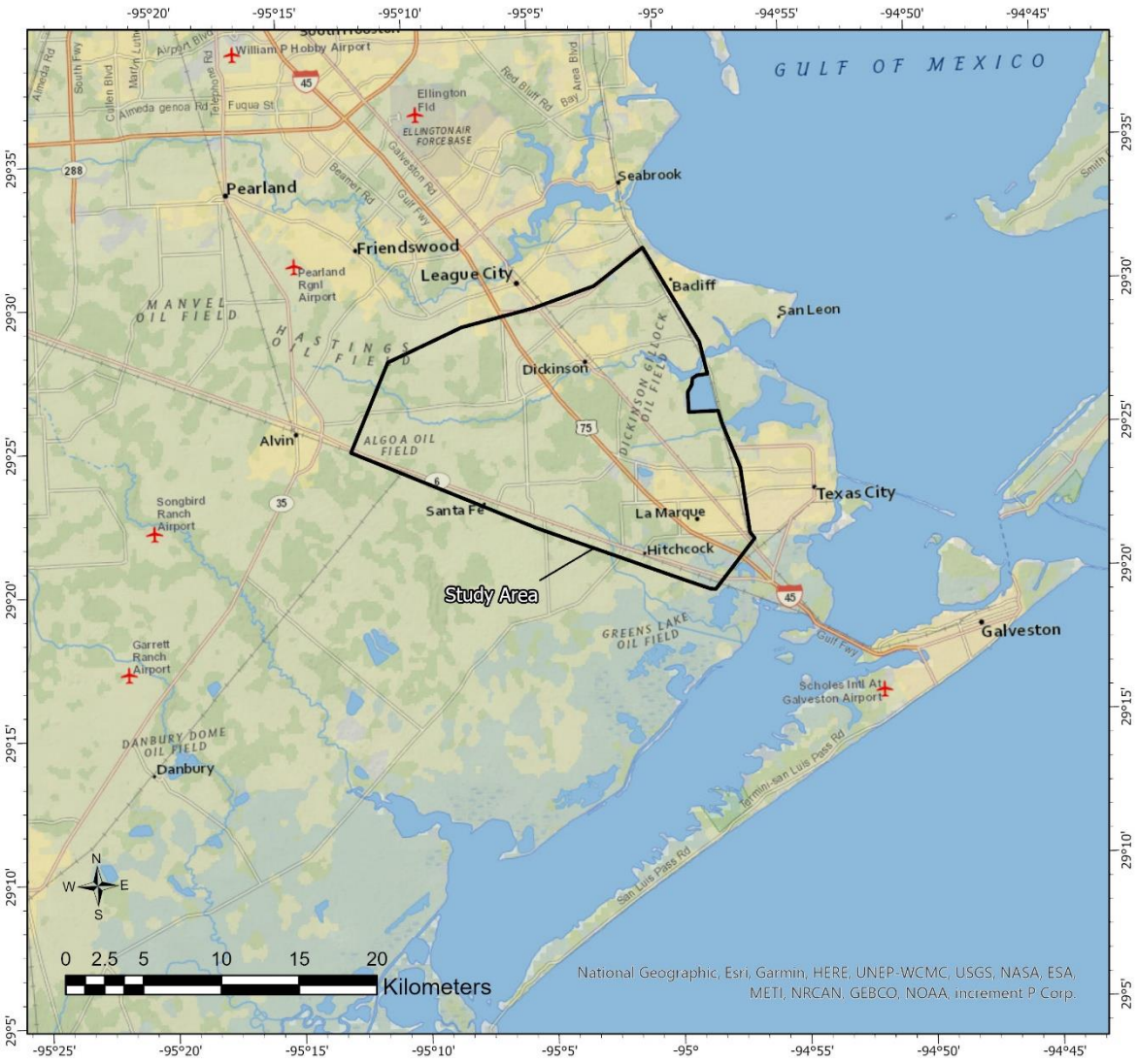

Figure 1-1: Map of the Study Area

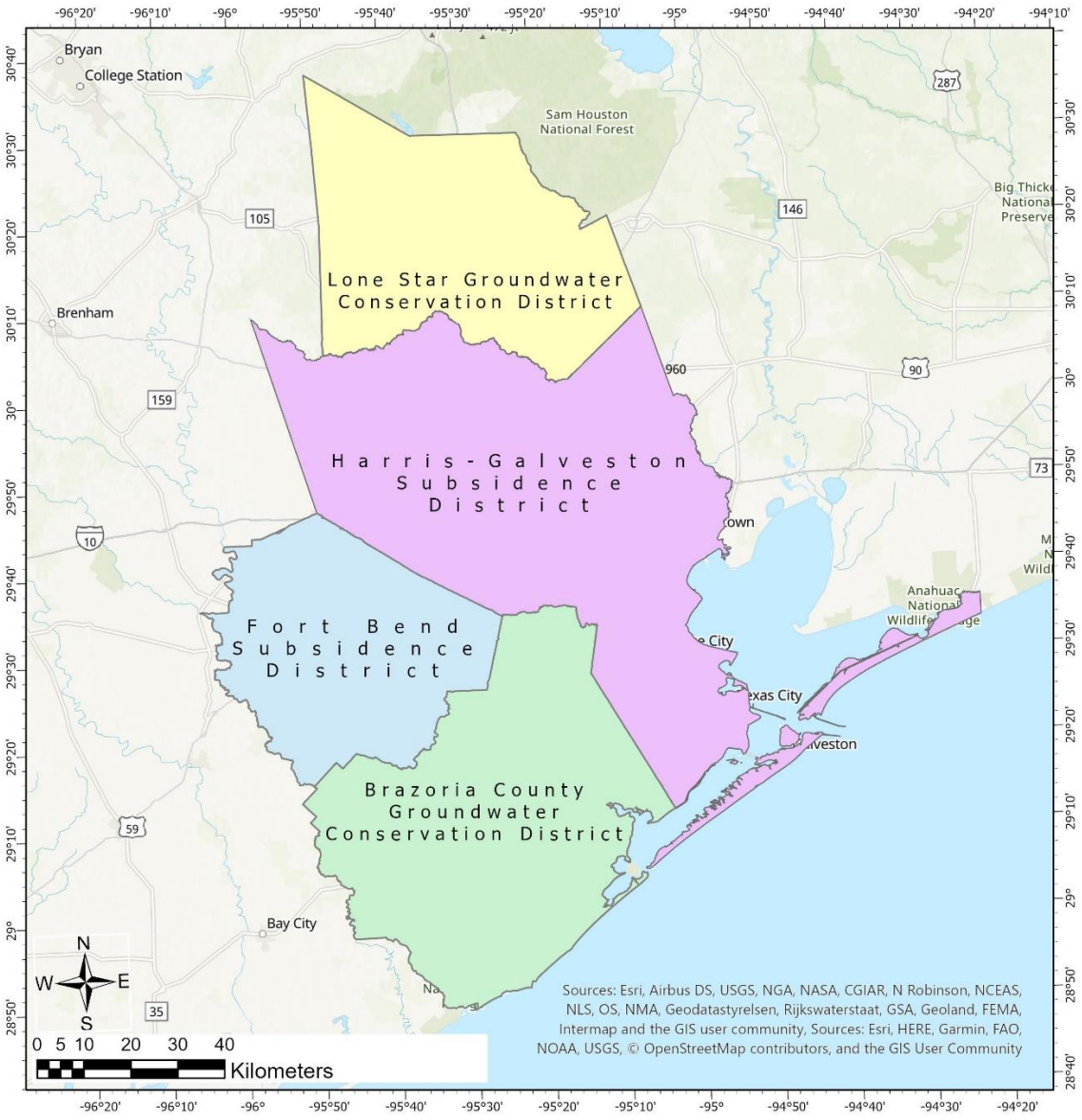

Figure 1-2: Greater Houston Area Subsidence Districts Outlines.

Aside from groundwater withdrawal, the Houston-Galveston area has experienced subsidence due to oil and gas extraction. The first experience with land subsidence was associated with shallow oil and gas extraction in the Goose Creek oil field in 1917. Before the 1940s, the localized subsidence seen in the area was due to the removal of oil, gas, and

associated exploration byproducts (Coplin and Galloway, 1999). Near Texas City lies the Goose Creek oil field, which removed millions of barrels of oil resulting in the center of the oil field, the low land, becoming submerged with water due to its proximity to Galveston Bay. This was due, in a large part, to the more than three feet of subsidence in the area close to two and a half miles by one and a half miles. In this area, vegetation was flooded, killed and the peninsula which was near the center of the field was gone. Ultimately, a consequence of this subsidence was faulting that subsequently followed (Coplin and Galloway, 1999).

In response to the mining of water, oil, and gas in the Gulf Coast area, the Harris Galveston Coastal Subsidence District was created in 1975. This would be the first of many subsidence districts to be established, including the Fort Bend Subsidence District, Brazoria County Groundwater Conservation District, and the Montgomery County Subsidence District (Coplin and Galloway, 1999). Figure 1-2 displays the boundaries of the subsidence districts in the Greater Houston area. These were created to minimize the ground subsidence through regulating and reducing groundwater withdrawal. A shift from groundwater to surface water took place due to these regulations (Khan et al., 2014). With the increased awareness of the side effects of subsidence, researchers began using new technologies such as GPS, and boreholes to monitor groundwater levels. The importance of this study is best stated by Coplin and Galloway in their explanation of how subsidence "has increased the frequency of flooding, caused extensive damage to industrial and transportation infrastructure, motivated major investments in levees, reservoirs and surface water distribution facilities and caused a substantial loss of wetland habitat(s)" (Coplin and Galloway, 1999).

2. REGIONAL GEOLOGY AND HYDROGEOLOGY

2.1 Structural Evolution of the Gulf of Mexico Basin

Houston, Texas is located on the northwestern corner of the Gulf of Mexico Basin, which is a small ocean basin between the North American plate and the Yucatan block. The Gulf of Mexico basin was the result of crustal extension and seafloor spreading which began during the Mesozoic breakup of Pangea. (Galloway, 2008). The process began with extension and stretching of the continental crust producing a series of basement grabens, half grabens, and topographic lowlands; this process preceded the breakup of Pangea which, occurred during the late Jurassic and early Cretaceous (Galloway, 2008). This continued stretching in the Bathonian and Callovian time produced a broad sag, which ephemerally opened the basin to the Pacific Ocean. Water did not fill the basin entirely, resulting in a shallow-water coverage over the thin continental crust. This led to the deposition of the Louann Salt formation and associated evaporites in the basin beginning around 163 Ma and terminated with the onset of seafloor spreading about 161-160 Ma (Bird et al., 2005; Galloway, 2008). Rifting continued and eventually split apart the salt deposits as oceanic crust began to form, allowing the basin to fill with water of a normal salinity. The rotational seafloor spreading moved the Yucatan Block to the south and the Florida-Bahama Block to the southeast resulting in the opening of the Gulf of Mexico (Bird et al., 2005). Seafloor spreading eventually ceased in the area by the early Cretaceous, around 140 Ma, and sediment from the surrounding continents deposited in the basin covered the salt formations (Bird et al., 2005; Galloway, 2008). During the Cenozoic, the structural evolution of the Gulf of Mexico was dominated by loading subsidence, clastic

sedimentation, and growth faults which began with the stretching and cooling of the basin crust (Galloway, 2008).

2.2 Depositional Environment

The depositional history of the Gulf of Mexico is marked by the subsidence of the crust, eustatic changes in sea-level and sedimentation from the continent north of the Gulf Coast plane (Galloway, 1989; Chowdhury and Turco, 2006). Repeated sea level changes and natural basin subsidence produced discontinuous beds of sand, silt, clay, and gravel. This was caused by alternating periods of deposition and non-deposition in the stratigraphic record. Early Cenozoic depositional events were drawn from erosion resulting from the uplift from the Laramide orogeny. From the late Eocene to the Miocene crustal heating, volcanism, and erosion in the southwestern United States and central Mexico filled the depositional episodes. Uplift and tilting of the western High Plains during the Pliocene further rejuvenated northwestern sediment sources from the Rocky Mountains, which is identified as the predominant sediment source for the fluvial-deltaic and shore-zone depositional systems in the Coastal Plains and the northern part of the Gulf of Mexico Basin (Galloway, 2005).

The depositional environment of the Gulf Coast Aquifer system alternated between shallow marine and fluvial-deltaic sedimentary environments. These aquifers include the Chicot, Evangeline, and Jasper aquifers. Repeated sea level changes and basin subsidence caused the cyclic sedimentary deposits composed of sand, silt, clay, and gravel (Kasmarek and Robinson, 2004). When sea level lowered continental sediments were deposited in a fluvial-deltaic depositional environment, whereas marine sediments were deposited in times of an elevated sea level (Kasmarek and Strom, 2002). These alternating sequences of fluvial-deltaic

and shallow marine environments led to the alternating deposition of aquifer and aquitard sediments (Kasmarek and Strom, 2002).

2.3 Hydrogeological Setting of Houston

The Texas Gulf Coast Aquifer System is also known as the coastal lowland aquifer system. This aquifer system is comprised of Miocene and younger unconsolidated sediments in layers of confining and water-bearing units (Ryder and Ardis, 2002). The cross-section displayed in Figure 2-1 provides the hydrogeologic units, their geometry, and depths of the individual units making up the Gulf Coast aquifer system. The units making up the Gulf Coast Aquifer System are the Chicot aquifer, Evangeline aquifer, Burkeville confining unit, Jasper aquifer, Catahoula Sandstone confining unit, Anahuac Formation, and Frio Formation. These hydrogeologic units dip perpendicularly towards the coastline (Chowdhury and Turco, 2006). Although the focus of this study will be on the Chicot and Evangeline aquifer, it is essential to take into consideration the other units making up the aquifer system. The water-bearing units are composed of laterally and vertically discontinuous fine to coarse-grained sands and gravels with interbedded silts and clays. The Chicot and Evangeline aquifer are not separated by a confining section; therefore, they are hydrologically connected (Ashworth and Hopkins, 1995). Due to the strata and gentle dipping of the coastal plains, the main water recharging this system is rainfall. Groundwater entering the system flows downward and laterally through the system from the northwest Greater Houston Area to the southeast towards the Gulf of Mexico. Typically, close to 47 inches of rain a year entering the outcrops in the northwestern area recharge the Gulf Coast Aquifer System (Bawden et al., 2012; Petitt and Winslow, 1957; Coplin and Galloway, 1999).

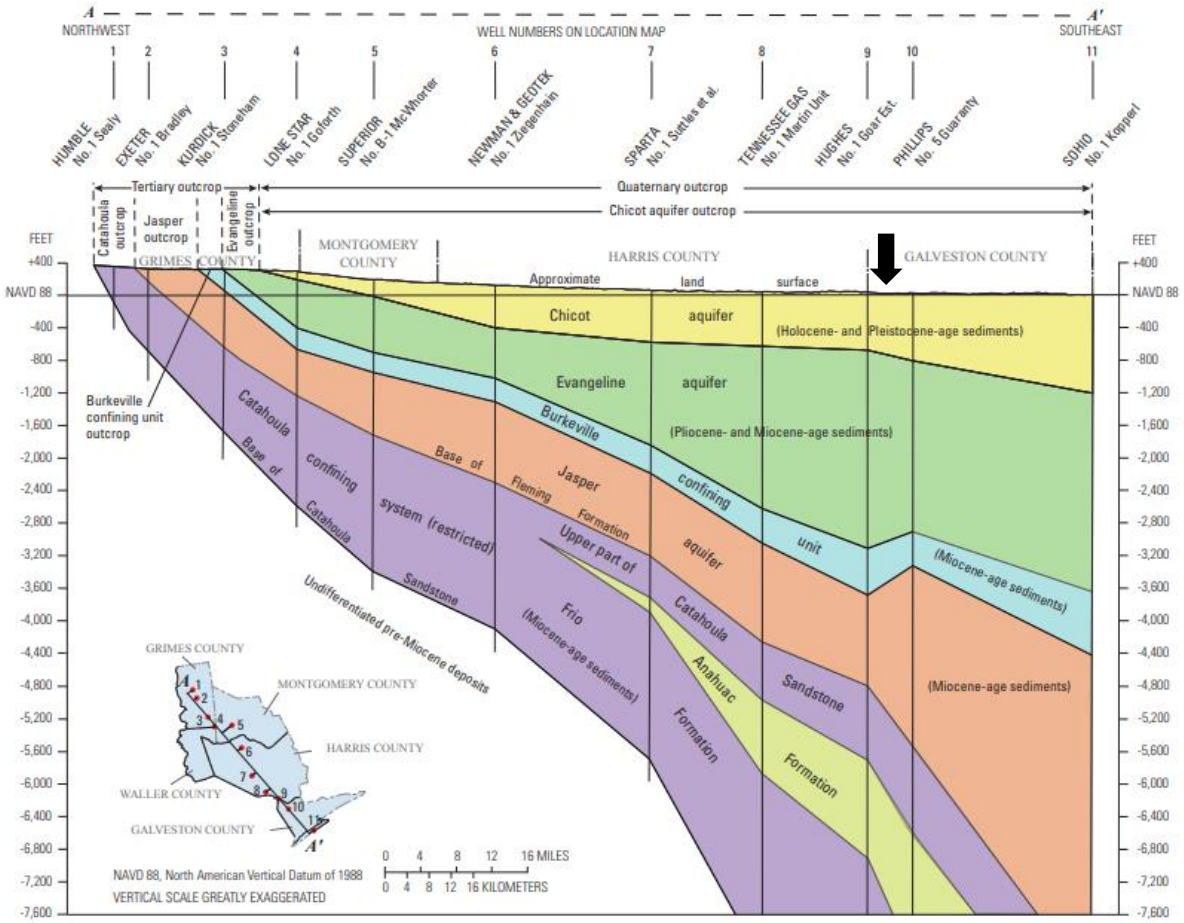

Figure 2-1: Hydrogeologic section of the Gulf Coast Aquifer System with study area marked in Harris, Galveston, and adjacent counties, Texas From (Kasmarek et al., 2015).

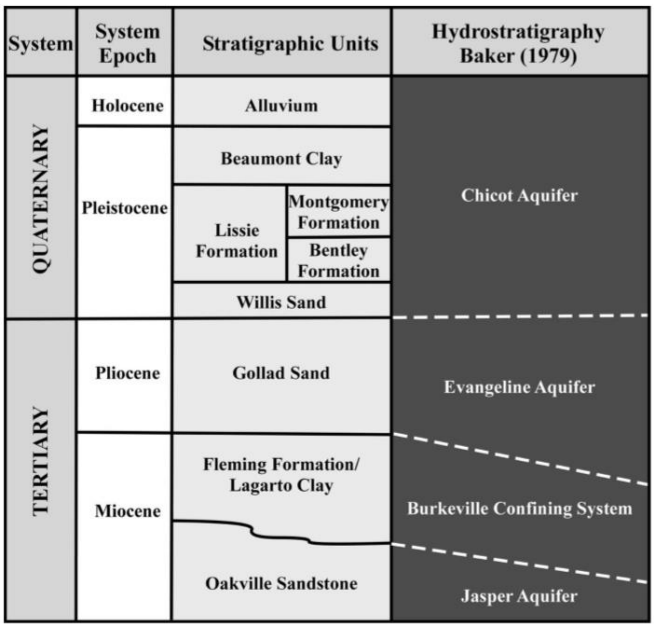

Figure 2-2: Gulf Coast Aquifer System and corresponding stratigraphic units (Baker 1979).

The Jasper Aquifer is the deepest and oldest aquifer of the Gulf Coast Aquifer System. The Jasper Aquifer is confined above by the Burkeville and below by the Catahoula unit making it the only fully confined aquifer unit in the Gulf Coast Aquifer System (Baker, 1978). The Jasper aquifer was deposited during the early Miocene comprising of the lower part of the Fleming Formation (Kasmarek and Strom, 2002). The Burkeville confining unit is predominately clay and was deposited between the middle and late Miocene. The Burkeville is comprised of the middle section of the Fleming Formation which is displayed in Figure 2-2 (Galloway, 2008). The Jasper Aquifer is not generally utilized for groundwater production.

The Evangeline aquifer is a semi-confined aquifer above the Burkeville confining unit and has been in use as a source of freshwater since the 20th century. The Evangeline aquifer was deposited starting from the late Miocene through the Pliocene (Baker, 1978). The depositional environment alternated between fluvial-deltaic and shallow marine, which resulted

in sands and gravels being interbedded with clays and silts (Kasmarek and Strom, 2002). Figure 2-2 displays the stratigraphic formations making up the Evangeline aquifer including the Fleming Formation and the Goliad Sand (Baker, 1978). Figure 2-3 displays the outcrop limits of the Evangeline aquifer.

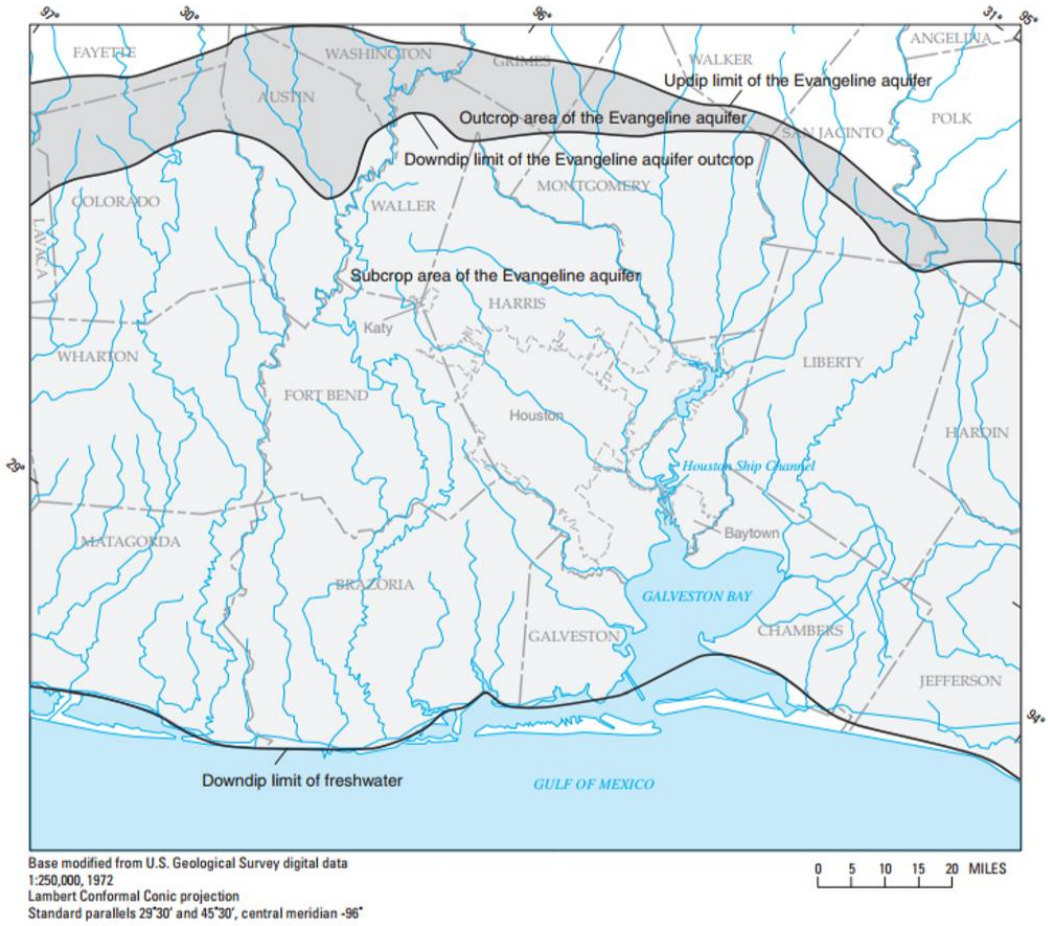

Figure 2-3: Regional outcrop of the Evangeline Aquifer (Kasmarek and Strom, 2002).

The Chicot aquifer is the shallowest aquifer of the Gulf Coast Aquifer System. The Chicot lies directly on top of the Evangeline aquifer without a distinct confining unit in between. Due to the complexity of its interlayered composition and the regional extent of its outcrop, the Chicot aquifer behaves as an unconfined aquifer near the surface and as a semi-confined aquifer

at depth (Kasmarek and Robinson, 2004). There is minimal hydrogeologic connectivity between the Chicot aquifer and the land surface (Kasmarek and Strom, 2002). The Chicot aquifer is composed of Pleistocene to Holocene-aged interbedded, discontinuous layers of sand, gravel, silt, and clay deposited in fluvial-deltaic to shallow marine paleo-environments, similar to the Evangeline aquifer (Baker, 1979). Figure 2-2 displays the stratigraphic formations making up the Chicot including the Beaumont Clay, Lissie Formation, Willis Sand, and Holocene alluvium. The Chicot aquifer outcrops regionally and terminates in the Gulf of Mexico. Figure 2-4 displays the outcrop limits of the Chicot aquifer.

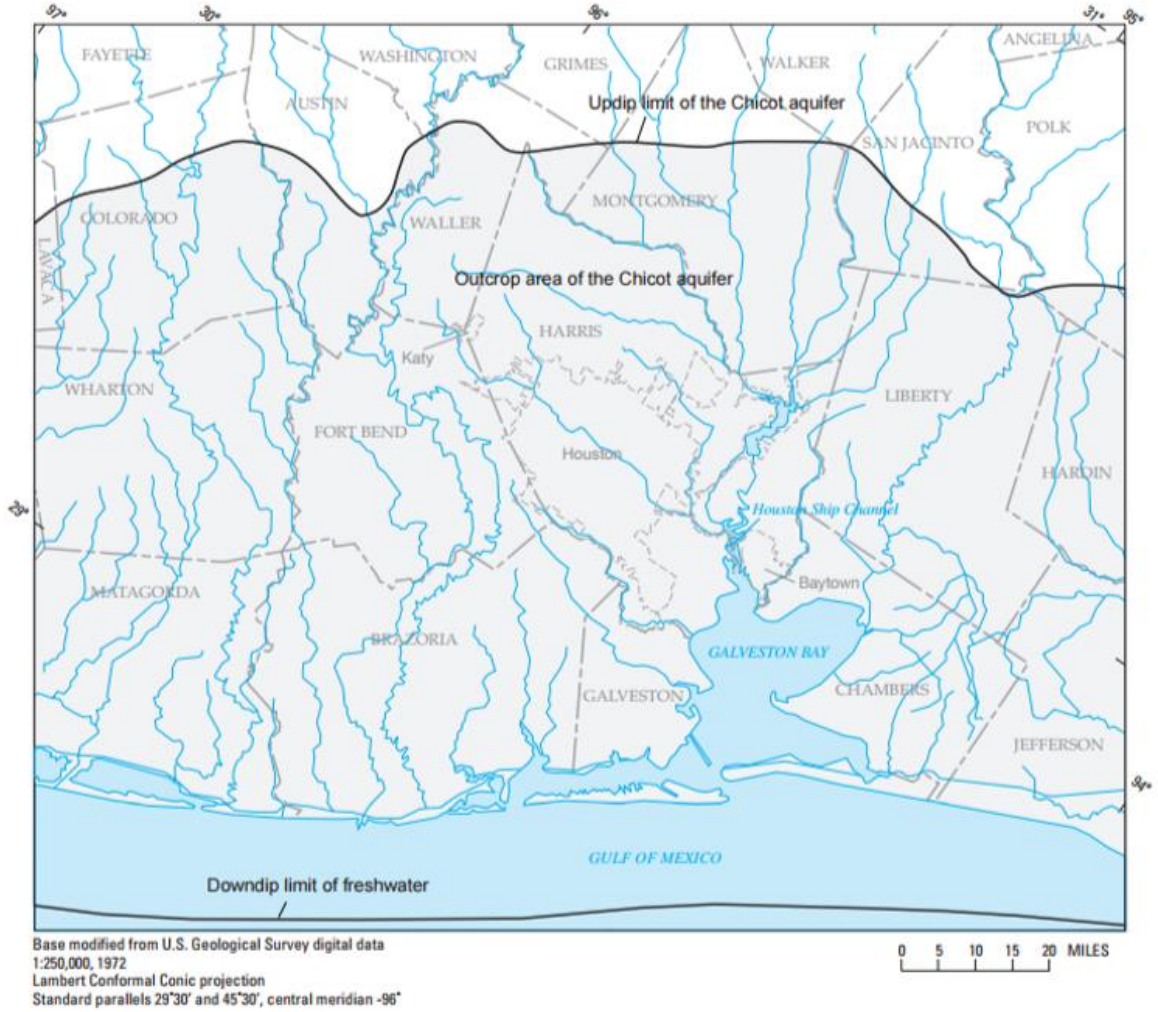

Figure 2-4: Regional outcrop of the Chicot Aquifer (Kasmarek and Strom, 2002).

3. LAND DEFORMATION MONITORING AND DATA

3.1 Geodetic Data

3.1.1 GPS Instruction

The Global Positioning System (GPS) is a satellite-based radio-navigation system that provides continuous three-dimensional positioning and navigation globally. Satellite navigation dates back to the Soviet launch of Sputnik 1 in the 1950s where two researchers at John Hopkins Applied Physics laboratory were monitoring the microwave signals that were being transmitted from Sputnik. During this analysis, they found that it is possible to delineate the satellite's orbit and its position by utilizing the Doppler effect (Guier and Weiffenbach, 1997). A GPS satellite was first introduced in 1978 in response to the United States Department of Defense's need for an accurate military navigation system. Although it was first introduced for the military, the civilian need quickly became apparent following the 1983 Korean Air Lines (KAL) Flight 007 incident. President Ronald Reagan decided that GPS technology was too valuable and opened GPS for dual use for military and civilians in 1983. Once GPS was released to the public deliberate degraded data was released for use by civilians through a feature known as selective availability (SA). SA's intentional degradation of data was for national security, but in 1998 President Bill Clinton decided that the removal of the SA feature would not pose a significant threat to national security and would allow for a wide variety of applications on a national and global scale.

GPS is divided into three areas of study: space segment, control segment, and user segment. The space segment includes a constellation of 24 operational satellites as well as three spares that are in high altitude orbit (El-Rabbany, 2006). The control segment or operational

control system monitors the space segment by tracking the GPS satellites. This includes monitoring their transmissions, behavior of their atomic clock, performance analysis, and sends commands or data to the satellite constellations. The control segment includes a worldwide network of tracking stations that includes a mater control station located in Colorado Springs, CO. The user segment is the receiver that interprets the microwave signals broadcasted by the satellite.

Conceptually GPS is based on satellite ranging or the distance from a satellite to the point observed on Earth. If at least four satellites are known a unique position can be determined through trilateration. The fourth satellite is necessary for timing corrections. Trilateration utilizes distances to measure the exact location on Earth. Satellite ranges conceptually can be determined by the kinematic equation:

$$x = vt$$

where x is distance, v is velocity and t is time.

3.1.2 Utilizing GPS for Subsidence Monitoring in Houston

The Harris-Galveston Subsidence District (HGSD) and National Geodetic Survey (NGS) have worked together to establish a network of GPS stations for use in monitoring land subsidence. This network includes a group of GPS stations that are designed as Continually Operating Reference Stations (CORS), which are permanent, and others that are designed to be portable and operate intermittently which are Port-A-Measure (PAM) (Zilkoski et al., 2003). While CORS are continuously monitored PAM stations utilize a campaign-style data collection (Zilkoski et al., 2003). In 2012, another network of continuously operating GPS stations, known as HoustonNet, was established to further aid in monitoring land subsidence. This project was

granted to the University of Houston under Dr. Guoquan Wang by the National Science Foundation (NSF). This network includes 67 continuously operating permanent GPS monitoring sites whose design and construction was supported by UNAVCO. Data from all HoustonNet sites are archived and publicly available through UNAVCO's data archive library. Figure 3-1 displays the locations of the GPS stations in the Greater Houston area. These GPS stations provide three-component positional and displacement measurements at regular sampling intervals of 15 s.

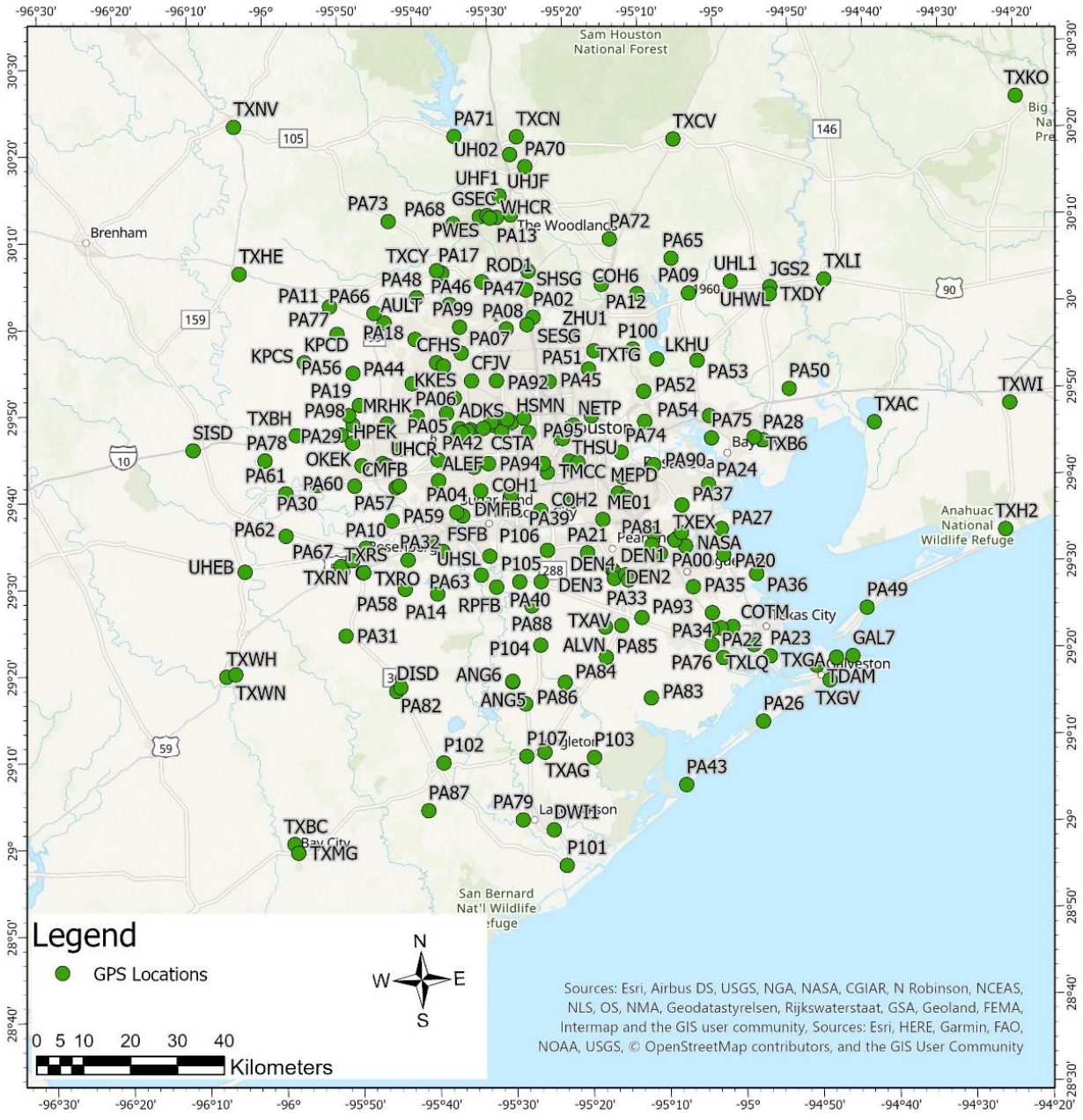

Figure 3-1: Position of all the GPS Stations located in the Greater Houston Area

Included in the HoustonNet network are stations located at the University of Houston's Coastal Center (UHCC) which is 300 acres and is located about 14 miles northwest of Galveston Island. UHCC includes a permanent continuously monitoring vertical GPS array and

weather sensor to actively monitor the subsidence in the area. The GPS array located at UHCC includes four permanent stations. These are antenna poles that are anchored to concrete plugs at different depths below the surface. Numerous stations in the Greater Houston area were utilized in this study including the stations UHC1, UHC2, UHC3, and UHC0, which are located on the UHCC's property. Each stations name represents an estimate of the depth at which it is located: UHC1 has a base at roughly 10 feet below the surface, UHC2's base is 20 feet below the surface, UHC3 is 30 feet below the surface, and UHC0 is roughly one foot below the surface, Figure 3-2 shows a three-dimensional view of the UHCC GPS array. This array allows for the measurement of the compaction at different ranges below the surface. Figure 3-3 and Figure 3-4 shows a site photo of the UHCC GPS Array.

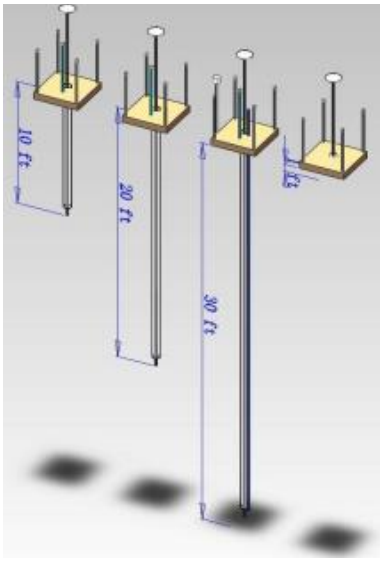

Figure 3-2: Conceptual diagram of the UHCC Vertical GPS array. From left to right: UHC1, UHC2, UHC3, and UHC0.

Figure 3-3: Site photo of UHCC Vertical GPS Array. From left to right: UHC1, UHC2, UHC3, and UHC0.

Figure 3-4: Aerial View of UHCC GPS Array.

The GPS receivers stationed around Houston, specifically at UHCC, provide a three-component ground position, absolute latitudinal (X), longitudinal (Y), and ellipsoid height (Z) coordinates each with measurements taken at regular sampling intervals of 15 seconds. Ellipsoid height is the distance perpendicularly between the surface of a reference ellipsoid and the point of a measurement. This study investigates ground deformation over a 20-year period between 2000 and 2020. Figure 3-5 displays the geographical locations of all GPS stations

utilized in this study to derive the regional vertical ground movements. Figure 3-6 displays a closer view of all the GPS units located in the study area where more detailed information will be derived. Figure 3-7 and 3-8 display an example of the X, Y, and Z motion of two GPS units used in this study, UHC1 and TXLM. Using the X, Y, and Z motion of GPS units and applying a linear regression model the overall trend of movement is displayed. Specifically looking at TXLM there is a distinct change in 2014 when looking at the vertical displacement time-series plot. Figure 3-9 displays the change in TXLM vertical displacement time-series graph that is seen post 2014. Comparing Figure 3-8 vertical component and Figure 3-9 it shows the decrease in the rate of the subsidence from the date of installation to 2020. Negative slopes represent land subsidence, whereas positive slope values represent land rebound or uplift when looking at the vertical component. The individual vertical displacement time-series graphs for each GPS station located within the study area are provided in Appendix I.

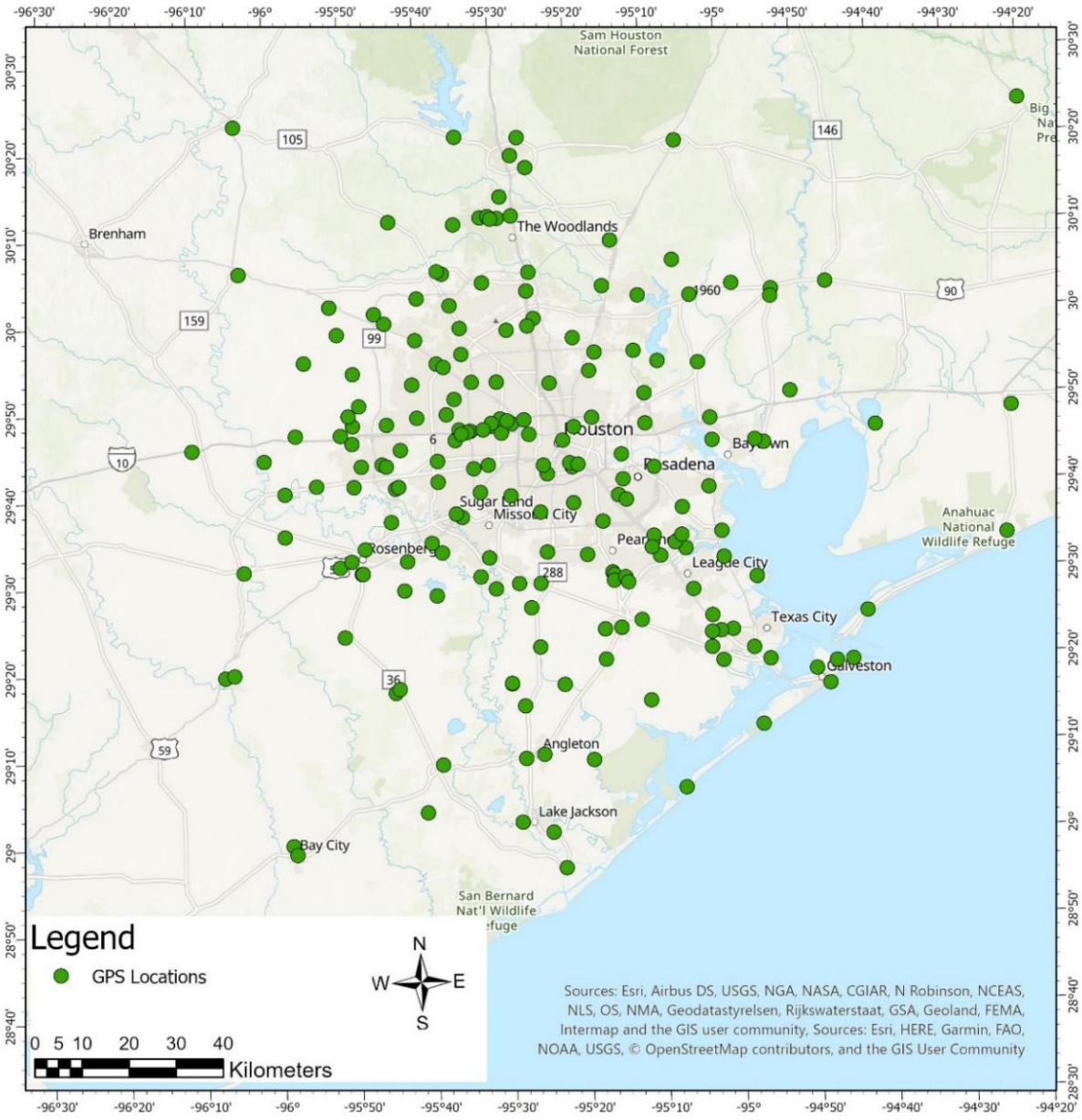

Figure 3-5: Locations of all GPS units utilized in the study.

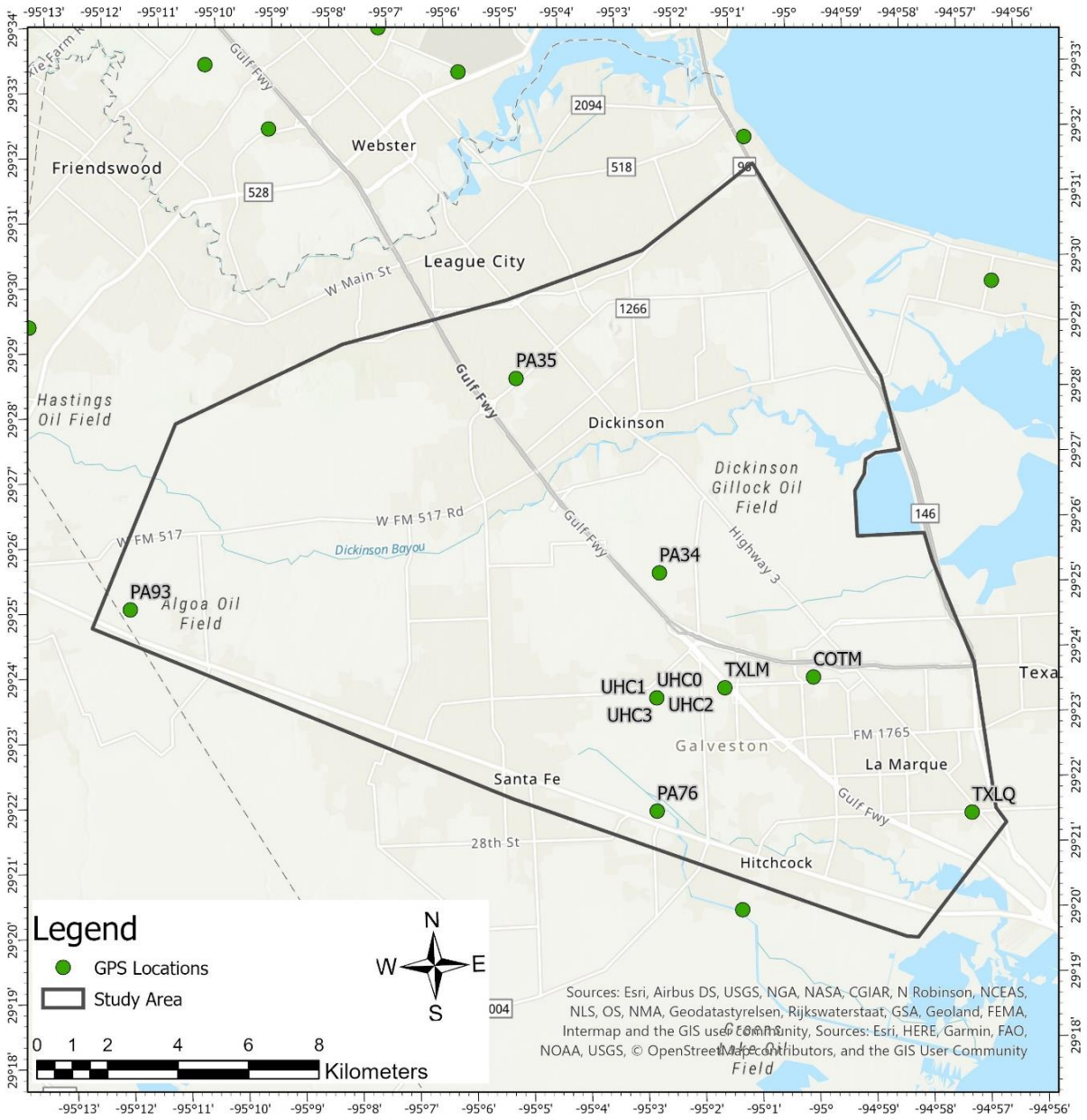

Figure 3-6: Study area with GPS sites labeled.

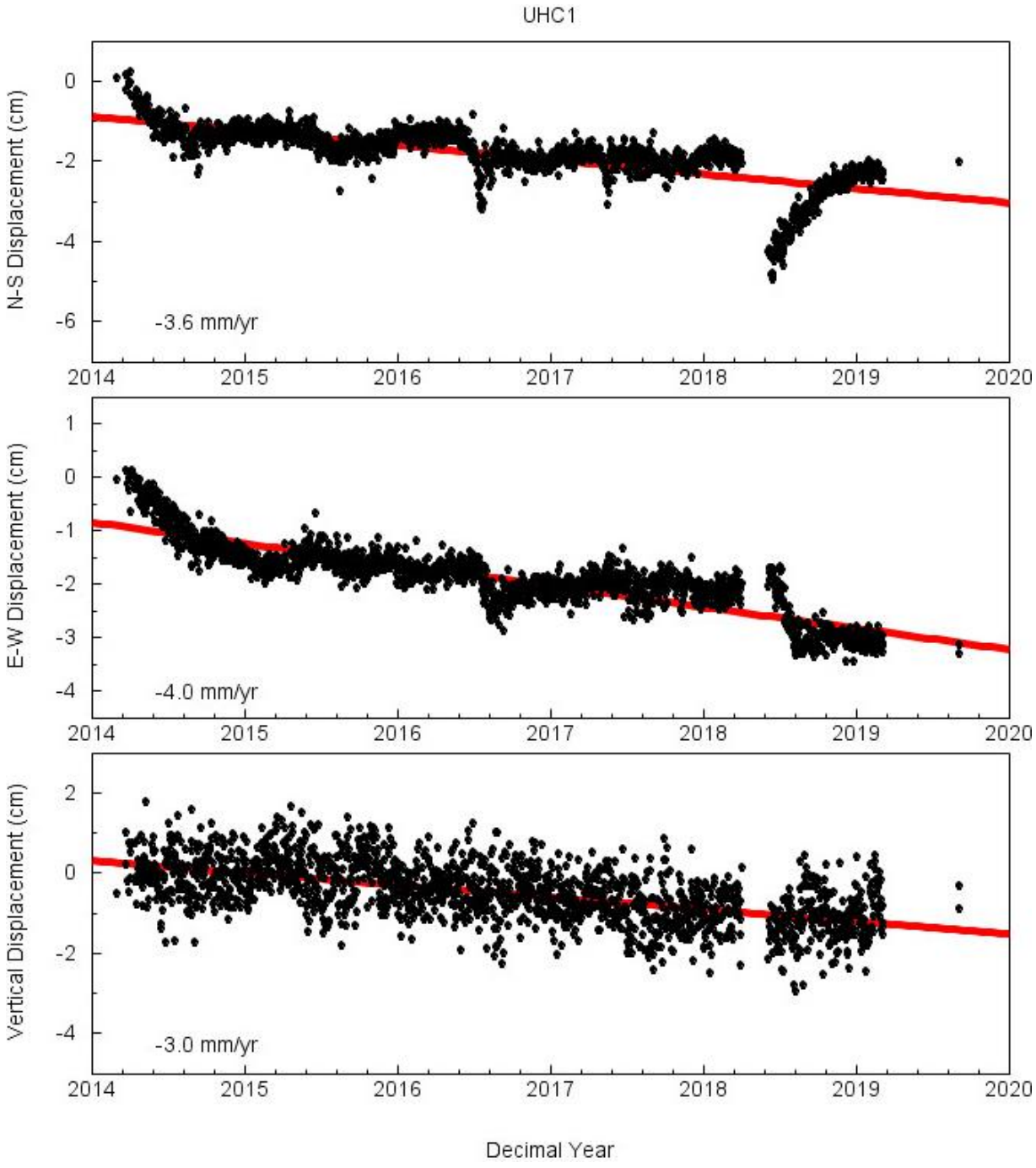

Figure 3-7: UHC1 Example of GPS three position time series analysis in the Houston20 Reference Frame.

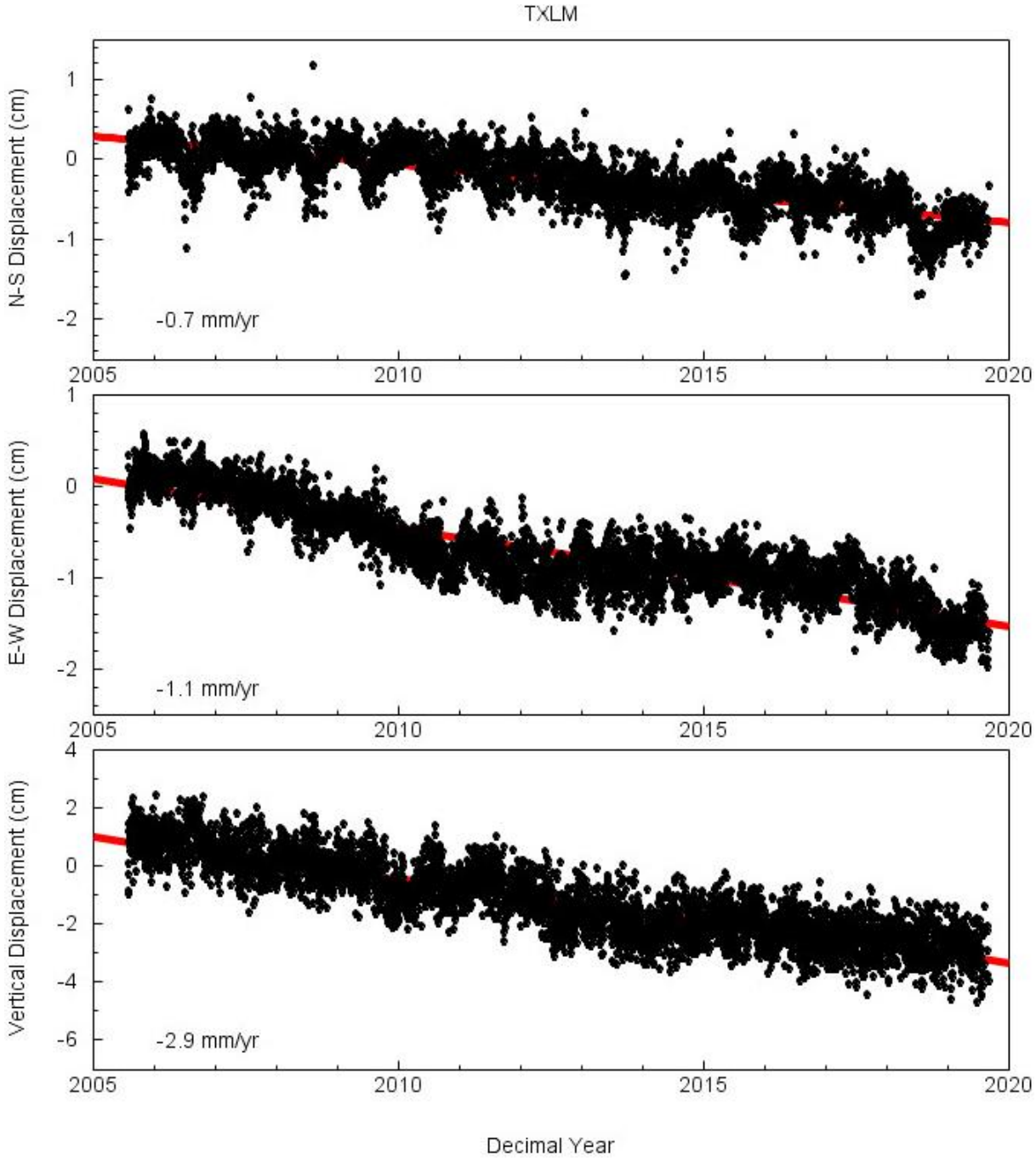

Figure 3-8: TXLM Example of GPS three position time series analysis in the Houston20 Reference Frame.

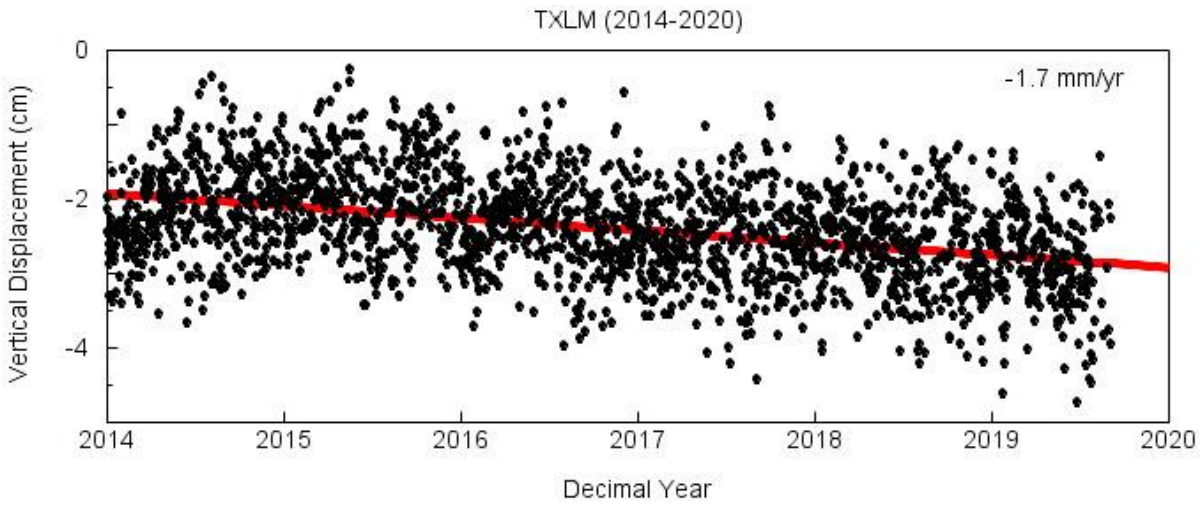

Figure 3-9: TXLM GPS Vertical Time series analysis displaying the change in slope from 2014 to 2020 in the Houston20 Reference Frame.

3.1.3 GPS Data Processing

Survey grade GPS units provide high quality data, but further processing and error reduction is necessary for high-quality data for ground deformation studies. The microwave range frequency signals that travel through the atmosphere from the satellite to the receiver allows for error to be introduced. Satellites transmit two signals known as the L1 and L2 carrier signals, 1575.42 MHz, and 1227.60 MHz, respectively, to be utilized to remove errors (El-Rabbany, 2006 and Trimble Monitoring Solutions). Aside from the signal, the timing information is essential for high accuracy and precision data when conducting ground deformation research.

GPS data post-processing is used for minimizing errors through a variety of techniques. Two of the main approaches for fixed solutions are relative positioning and absolute positioning; these are the methods of double differencing and Precise Point Positioning (PPP), respectively. Double differencing has historically been the most utilized but over the past

decade, PPP has become widely popular. The relative GPS positioning method utilizes simultaneous observations from two or more GPS units with a known location to correct for errors. However, PPP does not require any reference or base station due to the processing parameters, which has led it to becoming largely popular (Wang et al. 2017). The processing parameters are collected from a global distribution of GPS receivers which lends itself to the advantage of a single receiver being able to be processed without others in the area. As well, this reduces the processing power necessary for calculations and a greater consistency in positioning than the relative positioning method (Píriz et al., 2009; Zumberge et al., 1997). PPP utilizes the data from the global reference network of GPS reference ground stations to find precise satellite orbits and clock information to fix phase ambiguities for each position. The completed theoretical development of PPP can be referenced in Zumberge et al. (1997).

There are many GPS post-processing software packages and online tools that are currently available. These include GAMIT, GIPSY-OASIS II, OPUS, and AUSPOS for research. For this study, GNSS (Global Navigation Satellite System)-Inferred Positioning System and Orbit Analysis Simulation Software (GIPSY-OASIS II) was utilized to process GPS data. GIPSY-OASIS II is provided from the National Aeronautics and Space Administration (NASA) Jet Propulsion Laboratory in Pasadena, California. GIPSY-OASIS II utilizes a Precise Point Positioning (PPP) to process GPS data. The GPS data utilized in this study were processed using the PPP method. The precision of measurements post-processing under ideal conditions falls between 3 to 4 millimeters horizontally and 6 to 8 millimeters vertically (Wang et al., 2015).

3.1.4 Stable Houston Reference Frame Houston20

GPS data for ground deformation research requires a high level of accuracy. To achieve this level of accuracy GPS data must be related to an appropriate coordinate system or a stable reference frame. Primarily, GPS positions are provided as a set of coordinates that are with respect to a reference frame, these reference frames may be global, regional, or local. A global geodetic reference frame is realized with an approach to minimize the overall movement of a group of selected reference stations that are distributed worldwide (Rebischung et al., 2012). An example of a global geodetic reference frame is the International GNSS Service reference frame of 2014 (IGS14). This results in the GPS derived movements at a specific site being dominated by factors such as long-term drift and rotation of a tectonic plate where it is located. Ultimately, this means that localized temporal ground deformation such as subsidence and fault creeping could be obscured or biased by the common motions such as glacial isostatic adjustment and other minor circular motions. Therefore, a stable regional reference frame is designed to exclude those common ground motions and highlight localized ground deformation.

In this study, the Stable Houston Reference Frame of 2020 referred to as Houston20 is used. This was developed by Agudelo et al. (2020) to continue the investigation of ground deformation in the Greater Houston area. Houston20 utilizes a group of 25 stable GPS reference sites located outside of the City of Houston with histories spanning at a minimum of eight years. This is an update from the Stable Houston Reference Frame of 2016 (Houston16) because stations that were no longer operational or have poor data quality were removed and additional reference stations were added. These reference stations are assessed for their vertical and

horizontal stability (Wang et al., 2019). Figure 3-10 displays the reference station locations and respective horizontal velocity vectors with respect to IGS14.

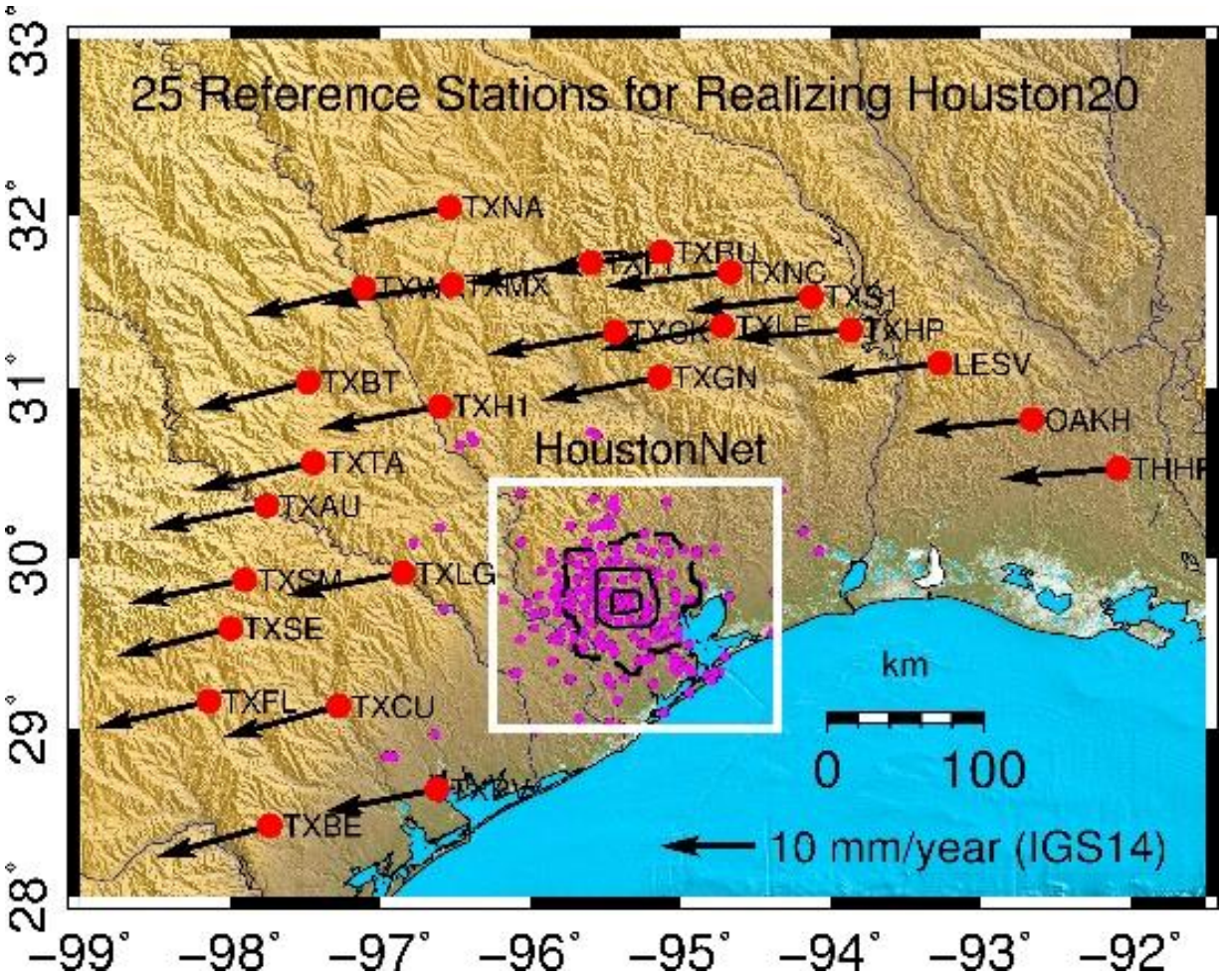

Figure 3-10: Locations and horizontal velocity vectors (relative to IGS14) of 25 reference stations utilized to realize the stable Houston Reference Frame "Houston20" (Agudelo et al., 2020).

Primary GPS coordinates are defined in the Earth-Centered-Earth-Fixed (ECEF) Cartesian coordinate system that represents positions in X, Y, and Z. ECEF-XYZ coordinates can be transformed to Houston20 by first being referenced to IGS14 by using GIPSY-OASIS II for post-processing and then transformed to Houston20. The Helmert transformation is

utilized in geodesy to produce distortion free transformations between ECEF-XYZ and other reference frames such as Houston20. The Helmert transformation for a position from an arbitrary reference frame A to B can be expressed as:

$$\begin{bmatrix} X_B \\ Y_B \\ Z_B \end{bmatrix} = \begin{bmatrix} T_x \\ T_y \\ T_z \end{bmatrix} + (1+s) \times \begin{bmatrix} 1 & -R_z & R_y \\ R_z & 1 & -R_x \\ -R_y & R_x & 1 \end{bmatrix} \times \begin{bmatrix} X_A \\ Y_A \\ Z_A \end{bmatrix}$$

where X_A, Y_A, and Z_A are the XYZ coordinates with respect to the original reference frame A and X_B, Y_B, and Z_B are the transformed XYZ coordinates with respect to the new reference frame B; T_X, T_Y, and T_Z are three translational shifts between the two reference frames along the x, y, z coordinate axes, respectively; R_X, R_Y, and R_Z are three rotations around the x, y, and z coordinate axes, respectively; and s is a scale factor. These seven parameters are typically computed using a minimum of three "common points" with known coordinates with respect to both systems. Ideally, more common points (reference stations) are used to solve the inverse problem by using the least-squares method. Typically, the scale factor is set to zero in reference frame transformations between global and regional reference frames. The coordinate transformation of the GPS-derived position time-series from IGS14 to Houston20 can be calculated using the following set of equations:

$$X(t)_{H20} = X(t)_{IGS14} + T'_x \cdot (t - t_0) + R'_z \cdot (t - t_0) \cdot Y(t)_{IGS14} - R'_y \cdot (t - t_0) \cdot Z(t)_{IGS14}$$

$$Y(t)_{H20} = Y(t)_{IGS14} + T'_y \cdot (t - t_0) - R'_z \cdot (t - t_0) \cdot X(t)_{IGS14} + R'_x \cdot (t - t_0) \cdot Z(t)_{IGS14}$$

$$Z(t)_{H20} = Z(t)_{IGS14} + T'_z \cdot (t - t_0) + R'_y \cdot (t - t_0) \cdot X(t)_{IGS14} - R'_x \cdot (t - t_0) \cdot Y(t)_{IGS14}$$

Where t_0 expressed a specific time epoch to align the two reference frames, Houston20 and IGS14. $X(t)_{IGS14}$, $Y(t)_{IGS14}$, and $Z(t)_{IGS14}$ are the ECEF-XYZ coordinates with respect to the

global reference frame IGS14; $X(t)_{H20}$, $Y(t)_{H20}$, and $Z(t)_{H20}$ are the ECEF-XYZ coordinates with respect to Houston20 T'_x, T'_y, T'_z R'_x, R'_y, and R'_z are constant parameters indicating the rates or one-time derivatives of three translational shifts and rotations between the Houston20 and IGS14 reference frames (Agudelo, 2020). Table 3-1 displays the seven parameters: t_0, T'_x, T'_y, T'_z, R'_x, R'_y, and R'_z, and the values required for the Houston20 Helmert Transformation equation provided above (Agudelo et al., 2020).

Table 3-1: Seven parameters for transforming ECEF-XYZ coordinates from IGS14 to Houston20 (Agudelo et al., 2020).

Parameters	Units	IGS14 to Houston20
t_0	Year	2016.0
T'_x	m/year	1.4040400E-02
T'_y	m/year	9.6139040E-04
T'_z	m/year	7.2404862E-03
R'_x	radian/year	-9.8590126E-10
R'_y	radian/year	-1.7311089E-09
R'_z	radian/year	1.3205311E-09

3.2 Hydrologic Data

3.2.1 Aquifer Wells and Locations

Groundwater hydraulic heads in the Greater Houston area are closely monitored for research purposes in conjunction with GPS and extensometer data to understand the relationship

between groundwater levels and subsidence. There are over 600 groundwater wells in the Greater Houston-Galveston area that are monitored by the USGS and three are monitored at UHCC for research purposes. These wells are completed in the Chicot and, Evangeline aquifers. Observational wells are completed at various depths within the Gulf Coast Aquifer System to provide additional information at sites such as extensometer locations. The groundwater well histories and sampling intervals vary, unlike GPS and borehole extensometer data. Some sites date back as far as the 1920s. Aside from varying site histories, data coverage varies at these locations because some measurements are taken by hand while others have been automated. All hydraulic-head measurements are given as a negative number which represents the depth below the surface. The larger the magnitude of a number the deeper the hydraulic head is. Groundwater data for the Greater Houston Area is publicly available through the USGS Groundwater Watch. Figure 3-11 displays the location of all groundwater wells completed in the Chicot and Evangeline aquifers utilized in this study. The red locations are wells completed in the Evangeline aquifer and the yellow locations are wells completed in the Chicot aquifer. Figure 3-12 displays all of the groundwater wells and site names within the study area of Dickenson - La Marque.

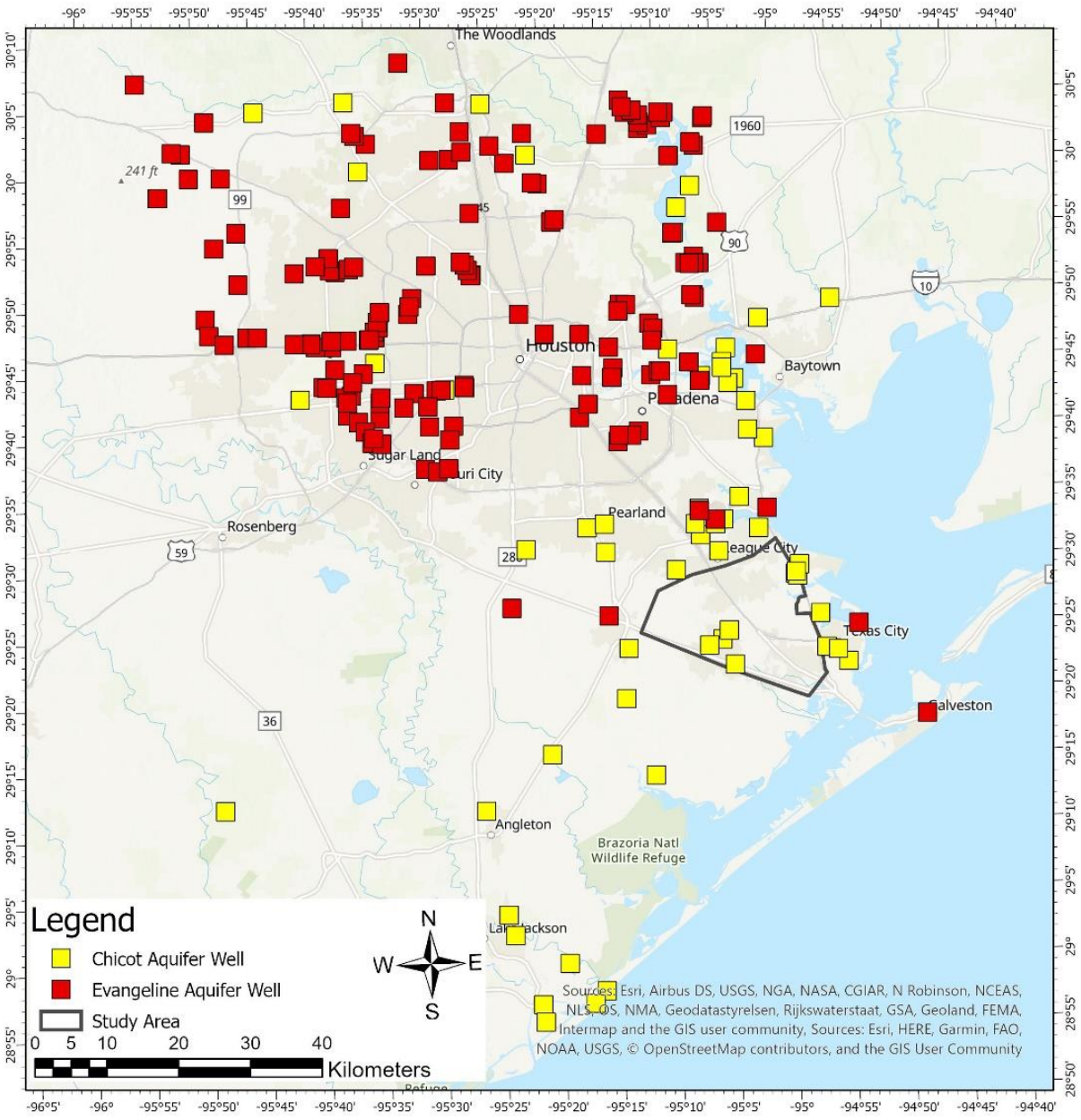

Figure 3-11: Locations of Groundwater wells used in this study

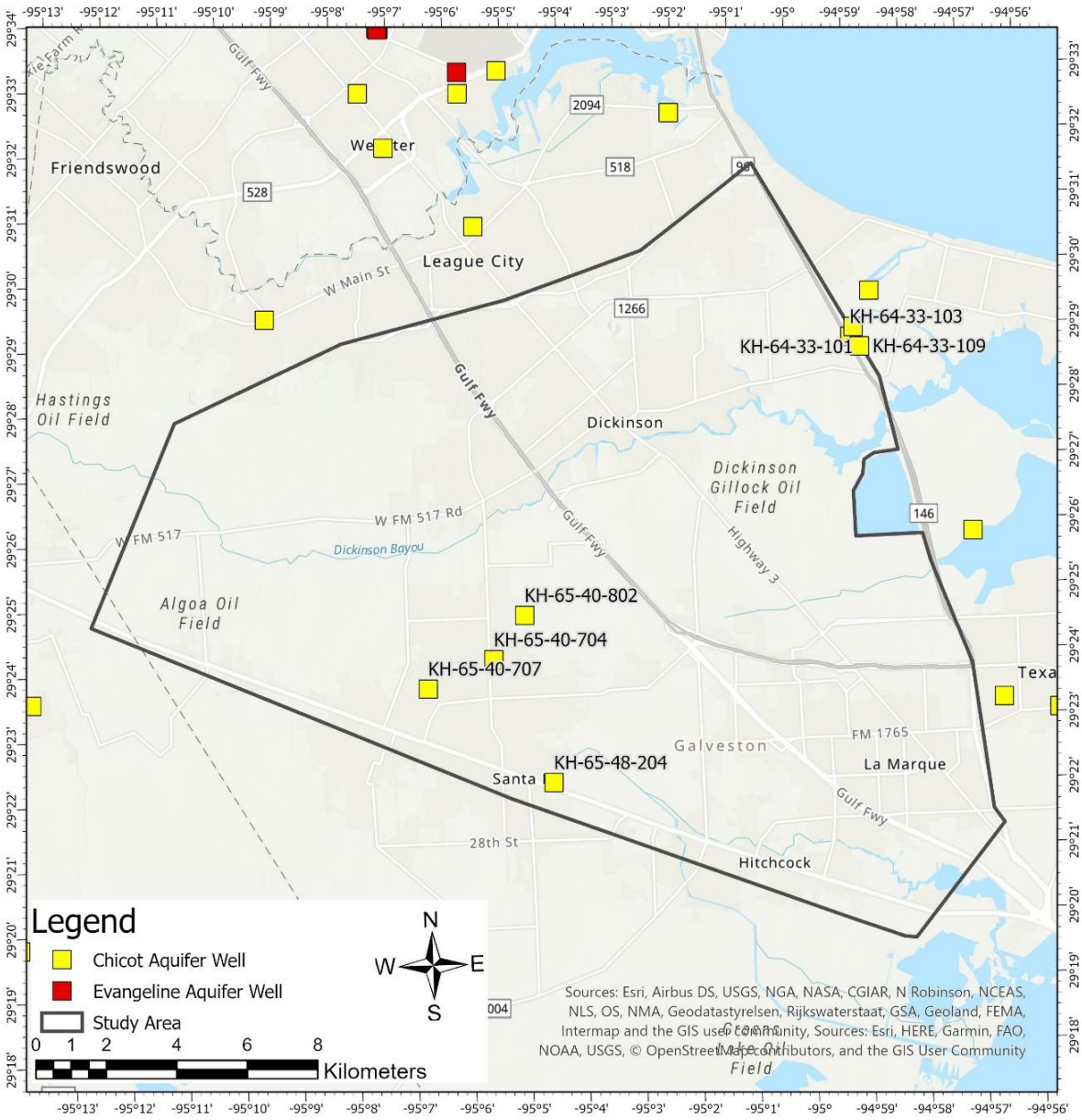

Figure 3-12: Location of Groundwater wells and site names in the study area

More specifically there are three groundwater wells located at UHCC. These are known as the Red, Blue, and Gray well. The Gray well is collocated at UHC3, and the Red and Blue wells are set off to the east on a separate but adjacent aquifer. Figure 3-13 displays the Red and Blue wells location in reference to each other, they are separated by about 18 m. These wells

are measured manually using the Solinst Water Level Meter Model 102 about every month. The water level meter measures in decimal feet and water level measurements are taken to the inside of the white PVC pipe rather than the red or blue outer casing. Figure 3-14 displays the Solinst Water Level Meter Model 102 and Blue well for reference.

Red Blue

Figure 3-13: Field image of the Red and Blue wells at UHCC.

Figure 3-14: Field image of Blue well with Solinst water level meter Model 102 and inner PVC pipe.

Groundwater level measurements from the Chicot and Evangeline aquifers will be utilized in this study. Only sites with histories spanning at a minimum of 5 years are utilized for data. Entire histories of groundwater measurements are used for investigation of long-period trends while subsets of site histories such as one to two-year periods are selected to more closely study the short-period trends. These groundwater level measurements are used to see the relationship of the aquifer levels over time and the subsidence rate.

3.2.2 Borehole Extensometer Data

In the Houston-Galveston area, there is a network of 13 borehole extensometers that were installed beginning in 1973, the locations of all the borehole extensometers are displayed in Figure 3-15. Each of these extensometers are collocated with groundwater wells completed in the Chicot and Evangeline aquifers. These borehole extensometers were established and are monitored and maintained by the USGS and HGSD. Extensometers provide information about the sediment compaction by measuring the land surface with respect to a fixed datum. The borehole extensometers allow groundwater to freely flow and as a result, they function as a piezometer to monitor the groundwater level within the respected aquifer it is terminated in (Kearns et al., 2015).

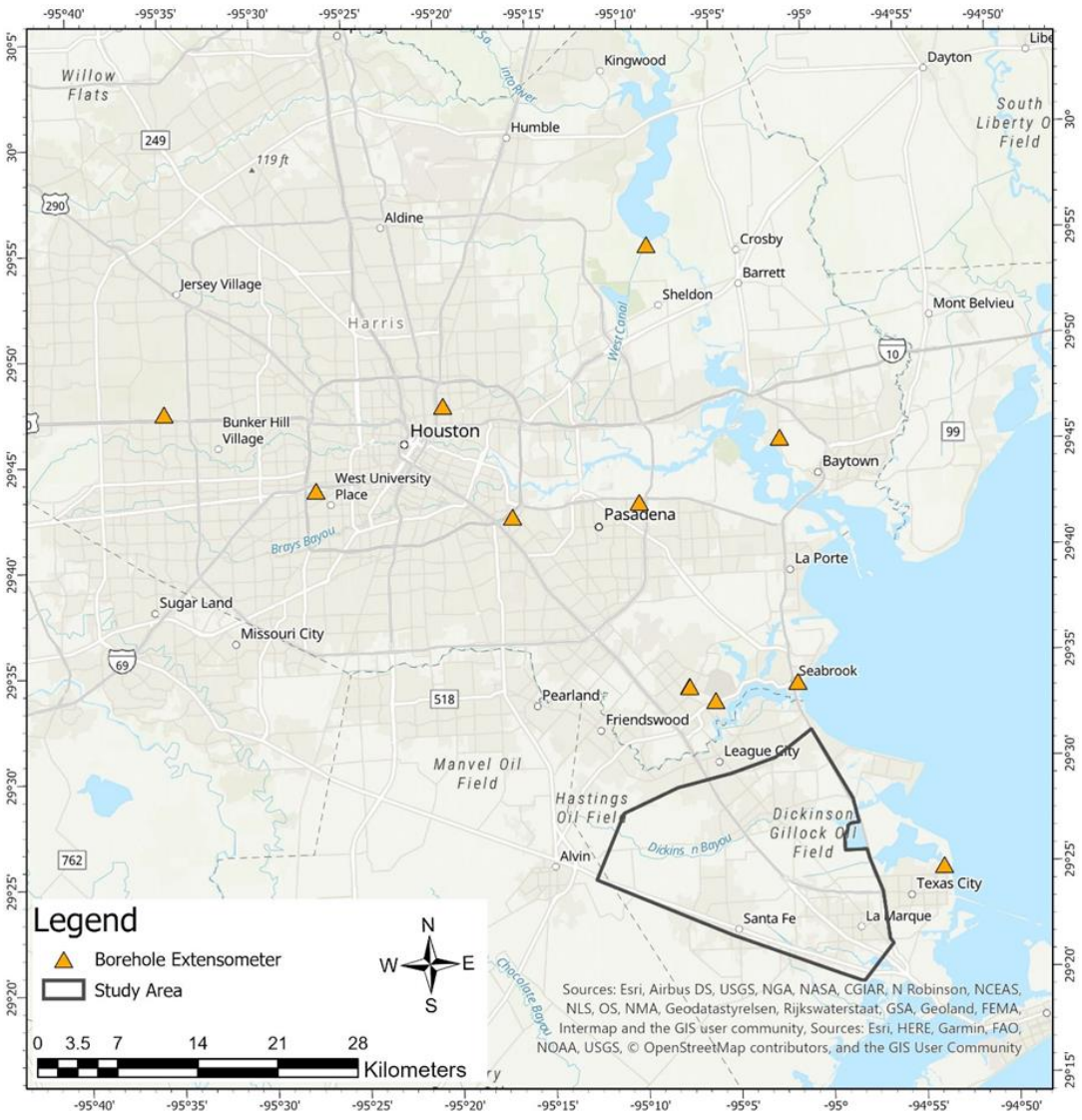

Figure 3-15: Locations of all Borehole Extensometers in the Greater Houston Area.

Borehole extensometers in the Houston-Galveston area are designed as “double pipe wells”, as seen in Figure 3-16 to provide information on compaction (Yu, 2014). Borehole extensometers are employed to measure the total compaction of sediment in reference to a fixed datum. This fixed datum acts as a stable benchmark below the level of compaction, and these measurements provide information about the amount of compaction in a given area. The

compaction of the area between the land surface and the bottom of the inner pipe is continuously monitored by an analog recorder (Yu, 2014). If the distance between the datum and land surface increases, then there is compaction, and if there is a decrease it is symptomatic of expansion or uplift (Wang et al., 2014). Extensometer sites may be capable of detecting ground-level changes down to fractions of a millimeter in magnitude (Wang et al., 2014). The data obtained from the various extensometers provide information about the cumulative compaction that has occurred at the site.

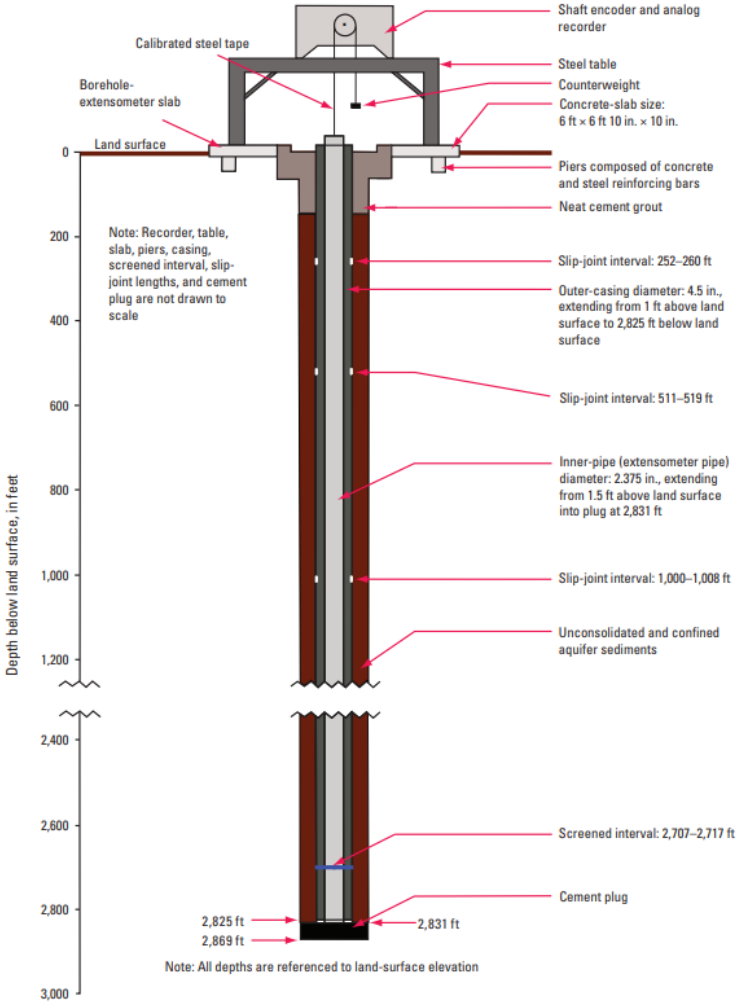

Figure 3-16: Schematic Diagram of a typical borehole extensometer utilized to quantify sediment compaction in the Greater Houston-Galveston Area (Kasmarek et al., 2012).

Previous studies by Wang indicate that there is a close relationship between borehole extensometers and GPS observations (Wang et al., 2014). In this study by Wang, the Addicks borehole extensometer data is collocated with GPS data from PA05 and ADKS. The borehole extensometer measures sediment compaction and land subsidence at depths that are associated with the Chicot and Evangeline aquifers. The ADKS GPS station that is fixed to the outer casing of the borehole extensometer displays the sediment compaction occurring beneath the Addicks borehole extensometer while PA05 provides information about compaction within the aquifers. A schematic of the setup at the Addicks extensometer site is displayed in Figure 3-17. The close data correlation between the Addicks borehole extensometer and the PA05 GPS unit provides validation about the aquifer compaction in the Chicot and Evangeline aquifers. The ADKS time series analysis displays that there is no significant sediment compaction beneath the Chicot and Evangeline Aquifers. The correlation between the two GPS stations and the borehole extensometer is displayed in Figure 3-18. The flatness ADKS time-series indicates that there is no compaction happening below the interval measured by the Addicks extensometer

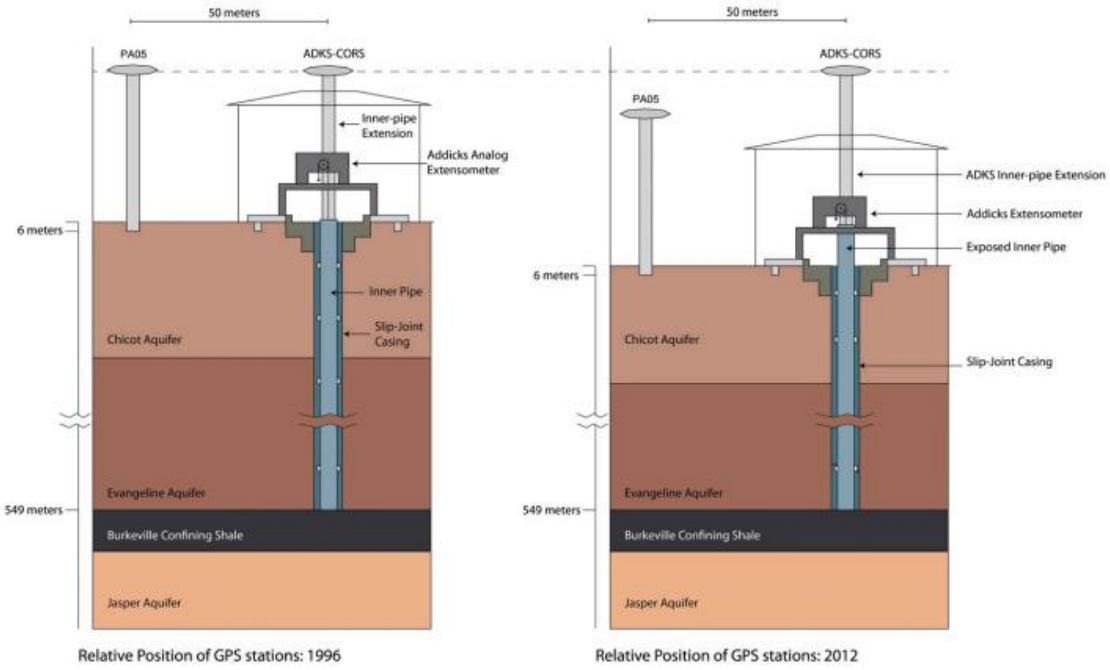

Figure 3-17: Schematic of GPS and Extensometer subsidence monitoring system at Addicks, Texas (Wang et al.,2014).

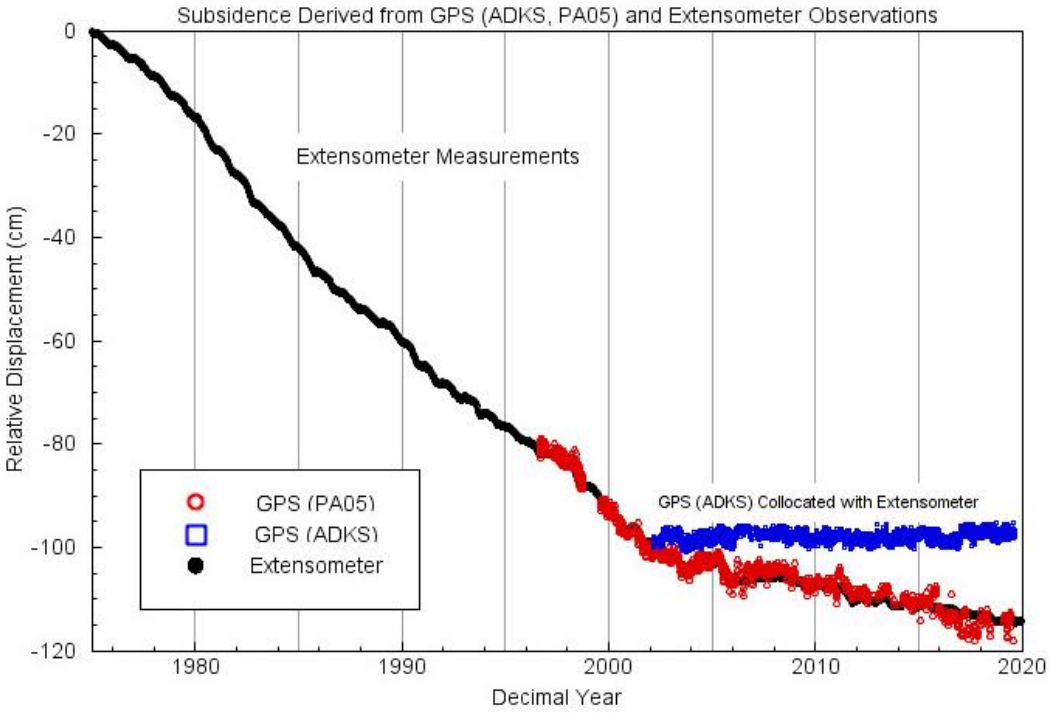

Figure 3-18: Comparison of subsidence derived from GPS and Extensometer data at Addicks, Texas.

4. AQUIFER DEFORMATION

4.1 Groundwater Withdrawal and Subsidence

Historically, subsidence has been an issue in the Gulf Coast region of Texas, especially in the areas around La Marque. In this study, subsidence is defined as the combination of natural and manmade lowering of the ground surface level. Most subsidence in the Houston-Galveston region has occurred because of groundwater withdrawals for municipal, industrial, and irrigation use. The relationship between groundwater levels and aquifer compaction can be summarized by:

$$\sigma_e = \sigma_T - \rho$$

where σ_e is the effective stress, σ_T is the total stress or overburden, and ρ is the pore-fluid pressure (Terzaghi, 1925). The equation demonstrates that when there is a reduction in the pore fluid pressure there is an increase in the effective stress at a given point in the soil system. When groundwater is withdrawn from confined portions of an aquifer, the hydraulic pressure of the sediment decreases. This withdrawal causes compaction of the overlying layers of the aquifer sediments (Ryder and Ardis, 2002).

When an aquifer is pumped, water is drawn downward and creates a cone of depression in the vicinity of the well. Regarding an unconfined aquifer, like the Chicot aquifer, drawdown is the reduction of the water table as the groundwater is released from an aquifer by gravity drainage near the source of pumping (Lohman, 1965). The size of the cone of depression is dependent on the rate of pumping, groundwater release, recharge, and discharge (Ryder, 1996).

Figure 4-1 describes the groundwater withdrawal in terms of the effective stress equation. The weight of the overburden above the aquifer is supported by the pore pressure exerted by the fluid in the aquifer, the structural strength, and the sediments in the aquifer provide the aquifer skeleton to support the system, Figure 4-2 describes the compaction of sediments in an aquifer system during groundwater withdrawal (Bawden et al., 2012). When the aquifer is pumped seasonally and the hydraulic heads remain above the preconsolidation stress threshold, the aquifer expands and contracts without any subsidence and compaction remains elastic. Alternatively, when the groundwater levels drop below the preconsolidation stress threshold, the silt and sand in the aquifer system compact and permanent subsidence can occur (Bawden et al., 2012). Therefore, in studies of land subsidence, compaction is considered to be the result of an increase in the effective stress acting on a column of sediment, and is tied to changes in the groundwater preconsolidation head (Galloway and Burbey, 2011).

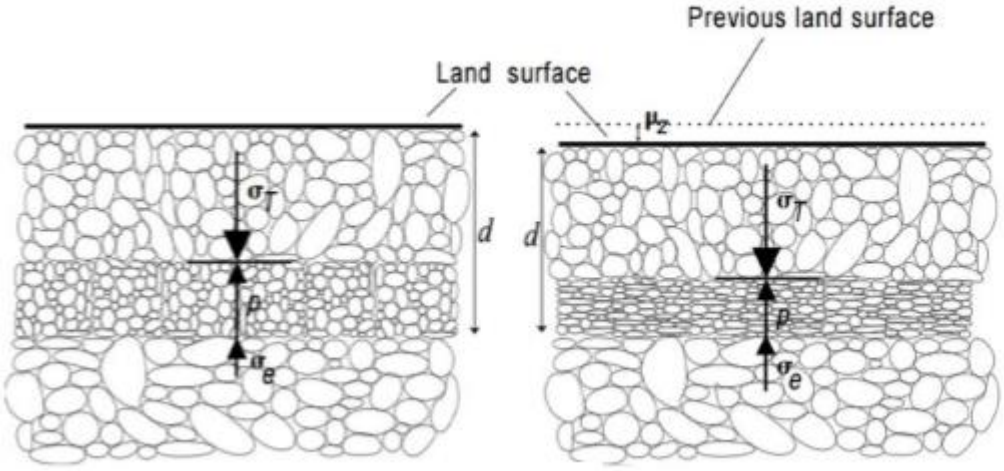

Figure 4-1: Conceptual diagram of land subsidence in terms of the Principle of Effective Stress. Modified from (Sneed and Galloway, 2000).

Previous work done at UHCC has displayed that there was a subsidence rate of 5-10 mm per year and that has since dropped to less than 5 mm per year. Between the years of 2014 and 2016, there was an inflation of the upper layer of sediments, but the lower layers of sediment continued to subside and were not restored to their original position (Lee et. al, 2014).

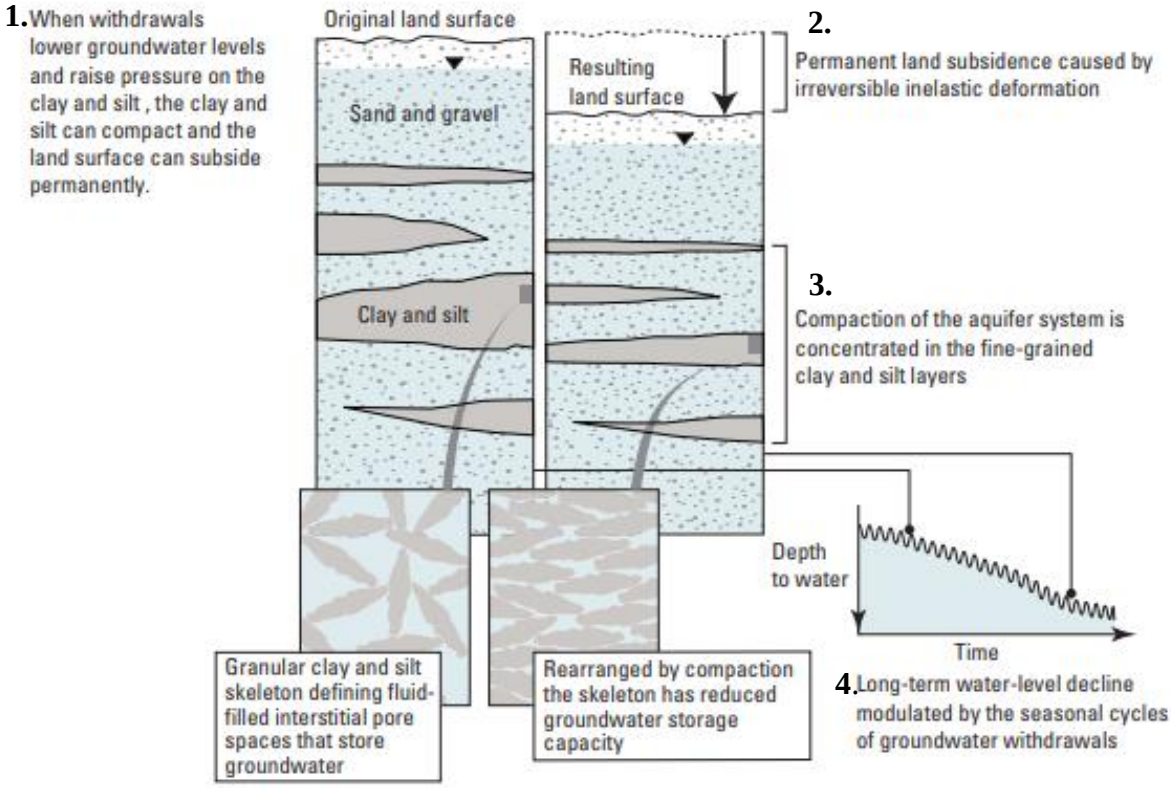

Figure 4-2: Diagram depicting the mechanism of subsidence in an aquifer composed of vertically discontinuous fine to coarse-grained sands and gravels with interbedded silts and clays. Numbers represent the order in which the process flows (Modified from Bawdin et al., 2012).

4.2 Preconsolidation Stress and Aquitard Drainage Model

Preconsolidation stress is defined as the maximum effective stress that a sediment volume has sustained previously. Upon exceeding this threshold, generally, the sediment volume will

experience permanent, inelastic deformation resulting from the realignment of its internal structure as seen in Figure 4-2 (Sneed and Galloway, 2000). Every time this maximum threshold is exceeded, the new maximum stress experienced becomes the new preconsolidation stress. Any applied stress to the sediment below the current preconsolidation stress will result in elastic deformation as it has previously (Sneed and Galloway, 2000).

The preconsolidation head is defined as the hydraulic head level that coincides with the preconsolidation stress (Leake, 1990). Terzaghi's Principle of Effective Stress and theory of hydrodynamic consolidation was used to create the aquitard drainage model to describe drainage of an aquifer system consisting of materials of variable permeability (Holzer, 1995). The hydrodynamic consolidation theory demonstrates the lag in the equilibration of pore pressure in aquitard units with adjacent draining aquifers. Otherwise put, as pore pressure in an aquifer declines due to groundwater production, there is a delay in the reduction of pore pressure in the adjacent aquitard due to its lower permeability (Schiffman, 1958). The aquitard material will continue to drain until the hydraulic pressure between both the aquifer and aquitard reaches equilibrium (Riley, 1998). When the effective stress experienced by aquitard material surpasses the initial preconsolidation stress, the aquitard material will be inelastically deformed. The primary factor of permanent land subsidence is the inelastic compaction of the slowly draining aquitard sediments (Tolman and Poland, 1940). As hydraulic heads in adjacent aquifers begin to recover it is common for aquitard sediments to continue compacting (Sneed and Galloway, 2000). Inelastic aquitard compaction will terminate only when hydraulic heads between aquitard and aquifer material reach equilibrium. The hydraulic head level at this equilibrium point signifies the new location of the preconsolidation head. Consequently, if the hydraulic head is not lowered past this new preconsolidation head, inelastic compaction or

permanent land subsidence would not be expected to occur or reinitiate (Holzer and Galloway, 2005).

The natural hydraulic head level in an aquifer system preceding anthropogenic groundwater production is known as predevelopment or native. The predevelopment preconsolidation stress is generally larger in magnitude than the natural effective stress experienced by an aquifer system before groundwater production. Additionally, current preconsolidation stress may not correspond with predevelopment preconsolidation stress, especially in systems that have experienced periods of lowered hydraulic heads and are affected by hydrodynamic lag (Galloway et al., 1999).

Figure 4-3 illustrates a conceptual model for groundwater withdrawal-induced land deformation and demonstrates the concept of hydrodynamic consolidation. When water is withdrawn from the aquifer, compaction increases gradually until the hydraulic heads drop below the preconsolidation level. Compaction is rapid until groundwater production is terminated at the time t_{stop}. Due to the difference in pressure between the aquifer and aquitard units, subsidence slowly continues as the hydraulic heads recover. Once the pressure has equalized, the hydraulic heads recover to the preconsolidation level and a slight rebound is observed.

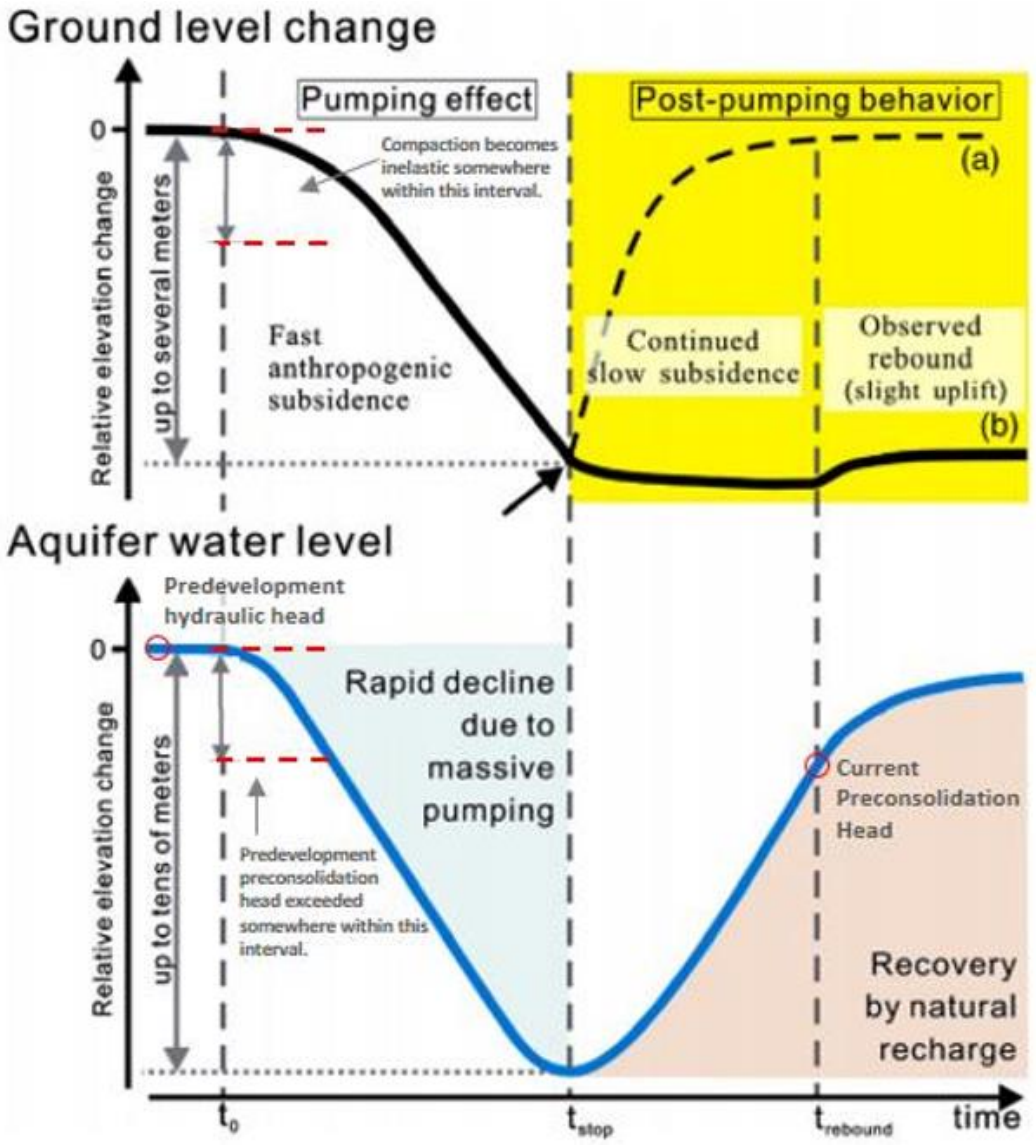

Figure 4-3: Conceptual model of ground deformation induced by groundwater withdrawal in a system experiencing hydrodynamic consolidation (Modified from Chen, 2007).

4.3 Groundwater Level and GPS Derived Subsidence in the Dickenson – La Marque Area

Water levels at several monitoring wells within the study areas were collected. GPS station data measuring the vertical component near these groundwater wells were analyzed in three

separate locations within the study area. A closer look into the Chicot and Evangeline water levels and the GPS station closest to those wells are described below in Figure 4-4 to Figure 4-6.

GPS stations located at UHCC were analyzed and displayed in Figure 4-4. Monitoring wells in the Chicot aquifer, Blue Well, Red Well, and KH-65-48-204 are the closest groundwater monitoring wells near these GPS stations. There is a steady slight water level rise from 2014 – 2020 within the Chicot aquifer at this location. Looking at the GPS vertical movement of units UHC0, UHC1, UHC2, and UHC3 there is less than a 1 cm per year rate of subsidence at the surface. The rise and fall of the GPS units at UHCC indicate seasonal variability. Seasonal variability exists where there is upward movement in the GPS station during spring when the Greater Houston area sees more rainfall, followed by downward movement during the summer when temperatures are higher, and precipitation is low. The water level increase and decrease in the Red and Blue well are consistent with student collected well data, seasonal groundwater changes, and groundwater levels that do not fall beyond the preconsolidation head. When looking at well measurements from KH-65-48-204 there is a steady increase in groundwater levels after a small rise and fall between 2014 and 2016 indicating that there is little to no natural recovery of groundwater taking place. The slow subsidence recorded can be from the inelastic compaction of sediments or swell that is naturally occurring, or small drawdowns within the Chicot aquifer. In conjunction with groundwater wells and GPS unit information while the GPS stations do show slight increase and decreased representing rebound and subsidence due to their changes in velocities, these velocities still need to consider the uncertainty of GPS positioning and the seasonal ground motions, thus

making each of these stations show a stable vertical velocity of 0 cm per year and subsidence due to groundwater withdrawal was mitigated in the UHCC area.

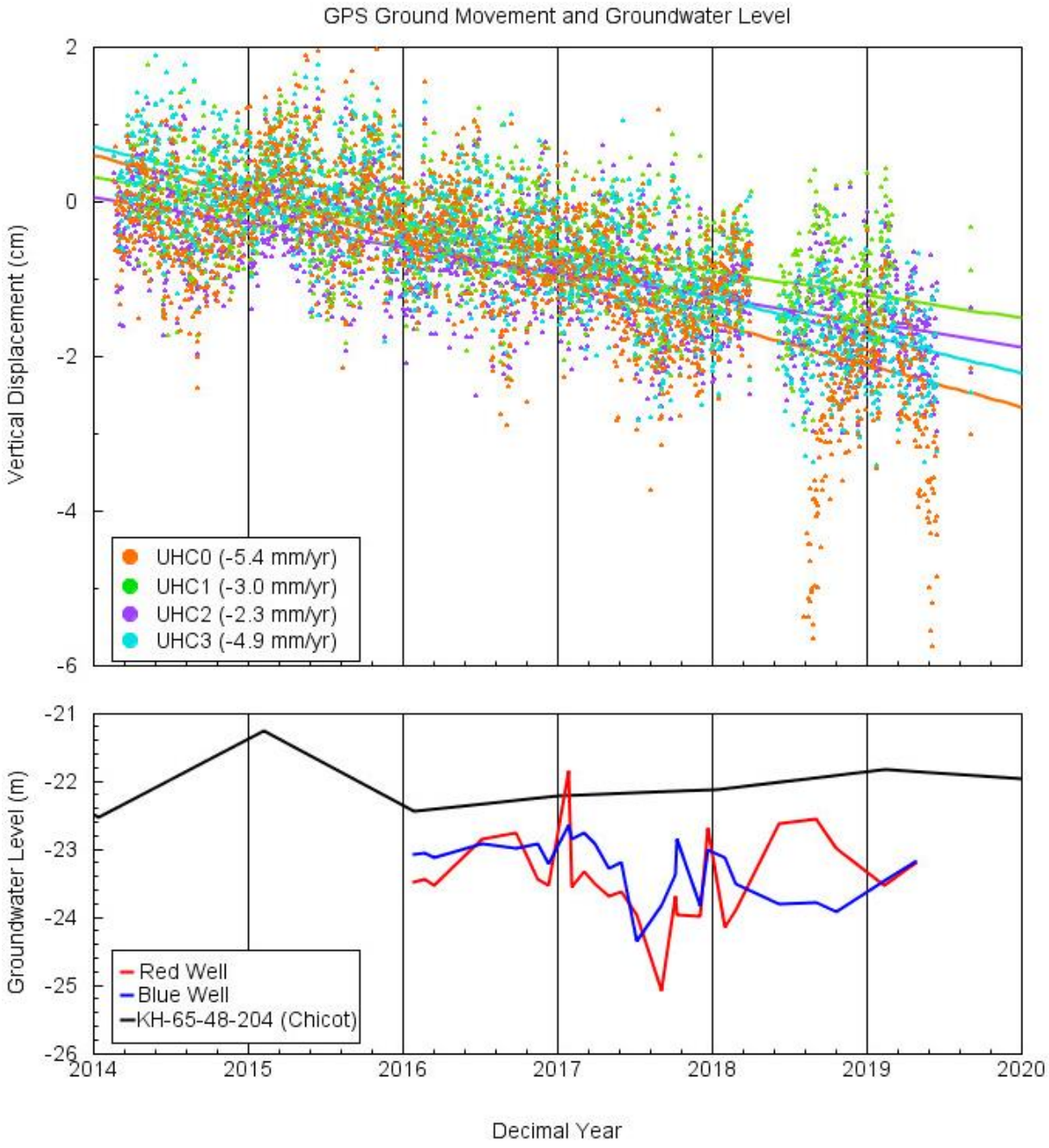

Figure 4-4: Comparison of Groundwater Levels and vertical GPS movement at UHCC and surrounding well location KH-64-48-204 in the Chicot aquifer. Groundwater levels display negative values representing depth below the surface. GPS negative values display subsidence while positive values display uplift or swell.

GPS stations located at TXLQ and COTM show a rebound of 0.3 mm per year and subsidence of 3.2 mm per year, respectively in Figure 4-5. When looking at the groundwater levels within the Chicot aquifer of the area at well KH-63-33-701 the groundwater level holds steady from 2012 to 2020. While these two stations do show a slight increase and decrease representing rebound and subsidence due to their changes in velocities, these velocities still need to consider the uncertainty of GPS positioning and the seasonal ground motions, thus making each of these stations show a stable vertical velocity and subsidence was mitigated due to groundwater withdrawal.

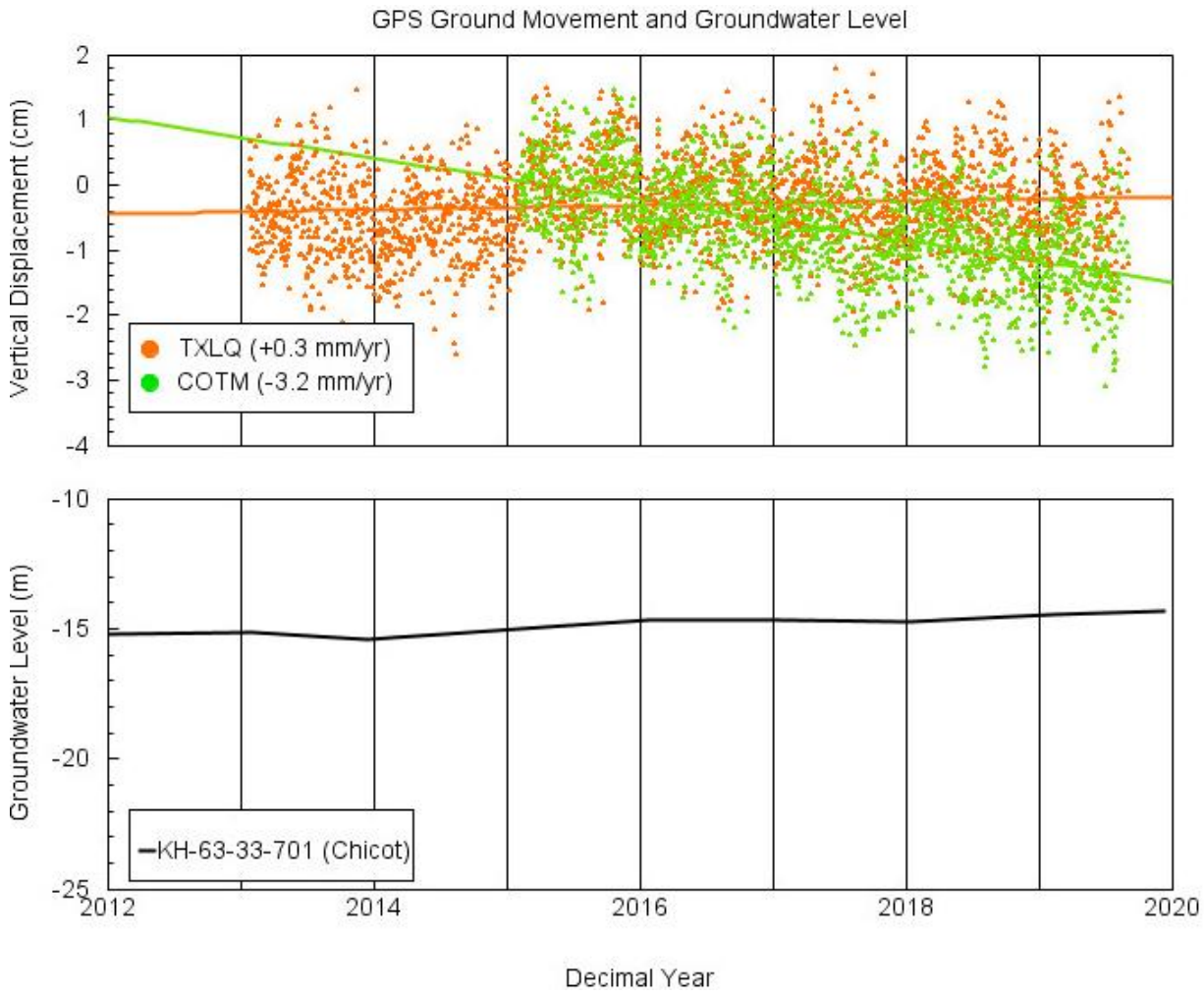

Figure 4-5: Comparison of Groundwater Levels and Vertical GPS movement at TXLQ and COTM and surrounding well location KH-63-33-701. Groundwater levels display negative values representing depth below the surface. GPS negative values display subsidence while positive values display uplift or swell.

GPS station located at NASA, Johnson Space Center, exhibits a rate of subsidence of 0.4 mm per year in Figure 4-6. When looking at the Chicot aquifer well LJ-65-32-401 which is collocated with the NASA borehole extensometer there is a steady groundwater level. While the GPS unit shows a negative velocity, which would be contributed to subsidence the uncertainty of the vertical GPS positioning and seasonal ground motions need to be taken into

consideration. This would prompt for the conclusion that there is a stable vertical velocity at the NASA site of 0 mm per year, which displays that subsidence has been mitigated due to groundwater withdrawal.

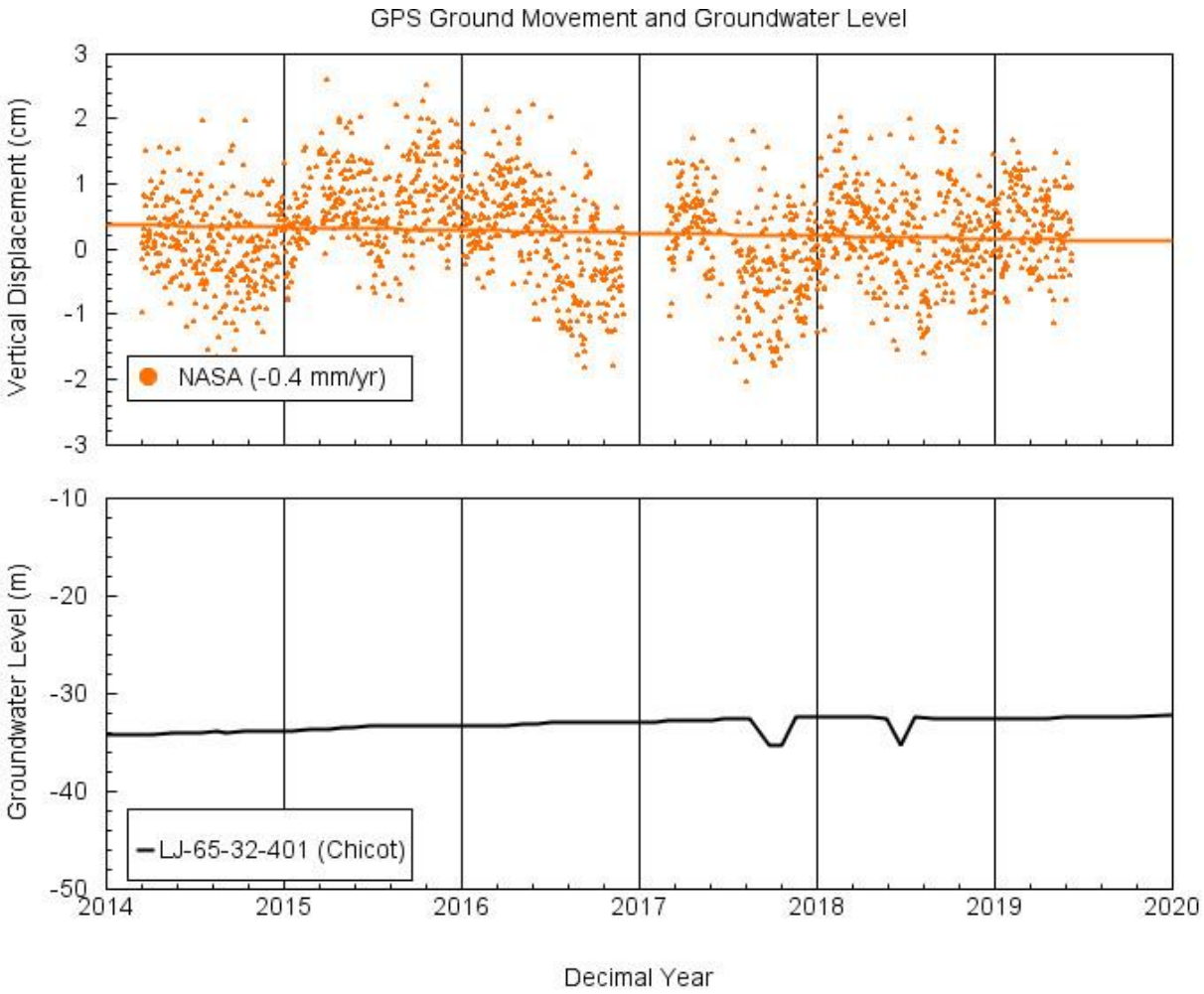

Figure 4-6: Comparison of Groundwater Levels and Vertical GPS movement at NASA and surrounding well location LJ-65-32-401. Groundwater levels display negative values representing depth below the surface. GPS negative values display subsidence while positive values display uplift or swell.

5. RECENT GROUND DEFORMATION AND COMPACTION TRENDS

5.1 Derivation of Ground Deformation Trends from GPS Data

Ground deformation trends in the Greater Dickenson - La Marque area are derived utilizing GPS data from various monitoring stations. These monitoring stations include those located in the CORS, PAM, and HoustonNet networks. GPS positions are referred to in ECEF-XYZ coordinates. Utilizing these coordinates, displacements can be calculated and analyzed as a single resultant vector or as individual vertical and horizontal components. Often studies regarding land subsidence assume the one-dimensional ground deformation model considering that horizontal displacements tend to be much smaller in magnitude compared to vertical displacements in areas experiencing land subsidence (Holzer, 1984). As well in the Greater Houston area, it has been well documented that the horizontal ground displacements are small, lack spatial consistency, and are not well correlated with vertical displacements (Kearns et al., 2015). As a result, for the purposes of this study, only the vertical component of the GPS data will be considered. An example of X, Y, and Z component measurements at the UHC0 various GPS station in the Greater Dickenson and La Marque area is provided in Figure 5-1.

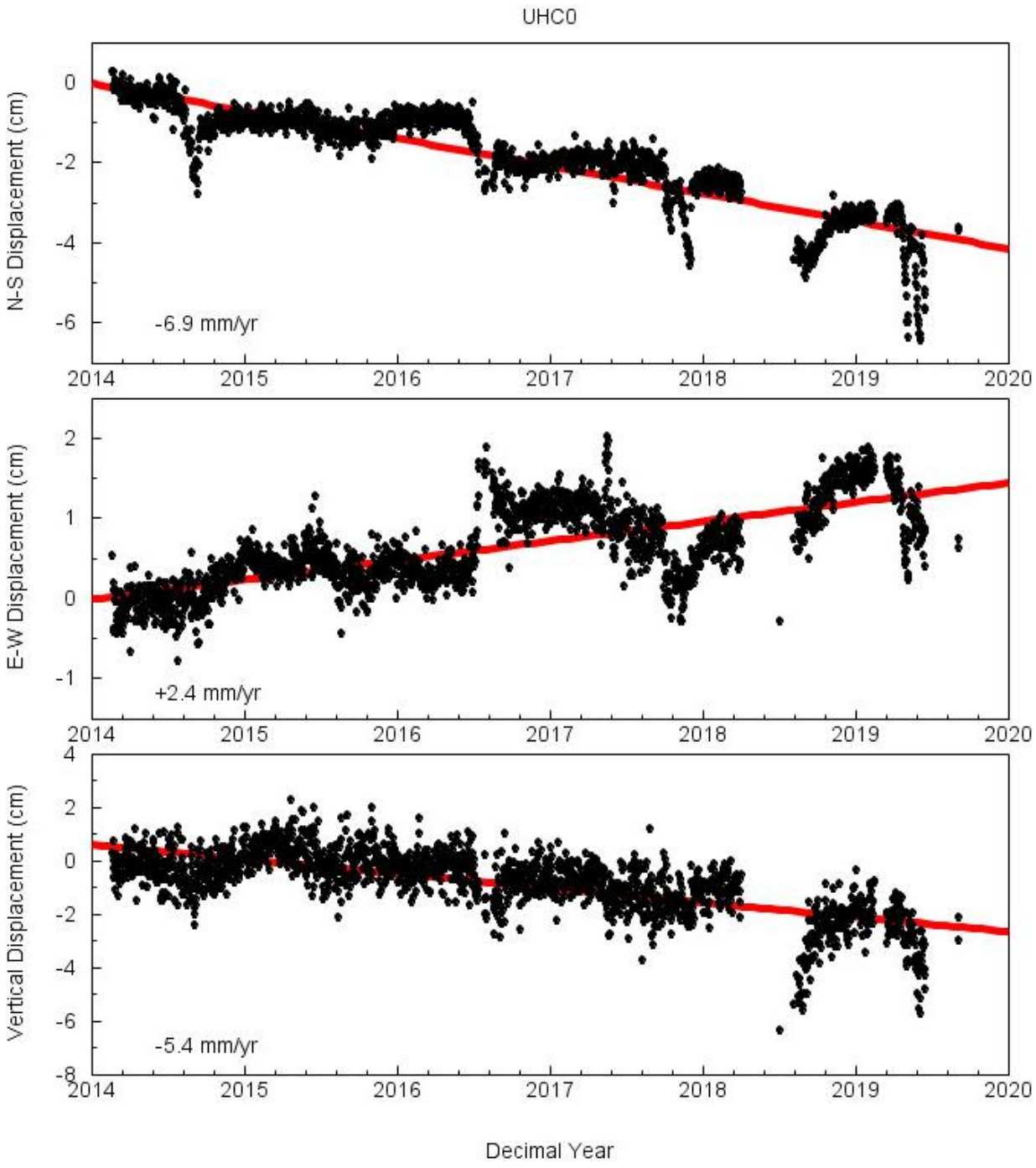

Figure 5-1: Example of a GPS Time Series plot. From top to bottom showing N-S movement, E-W movement, and Vertical movement.

In this study vertical velocity vectors were derived from the GPS observations from beginning of collection to 2020 were analyzed for ground deformation trends. Figure 5-2 displays the vertical velocity vectors that were derived and are referenced to the stable Houston Reference Frame Houston20. Here, it shows spatially the trends of uplift and subsidence that is occurring in the Dickenson - La Marque area.

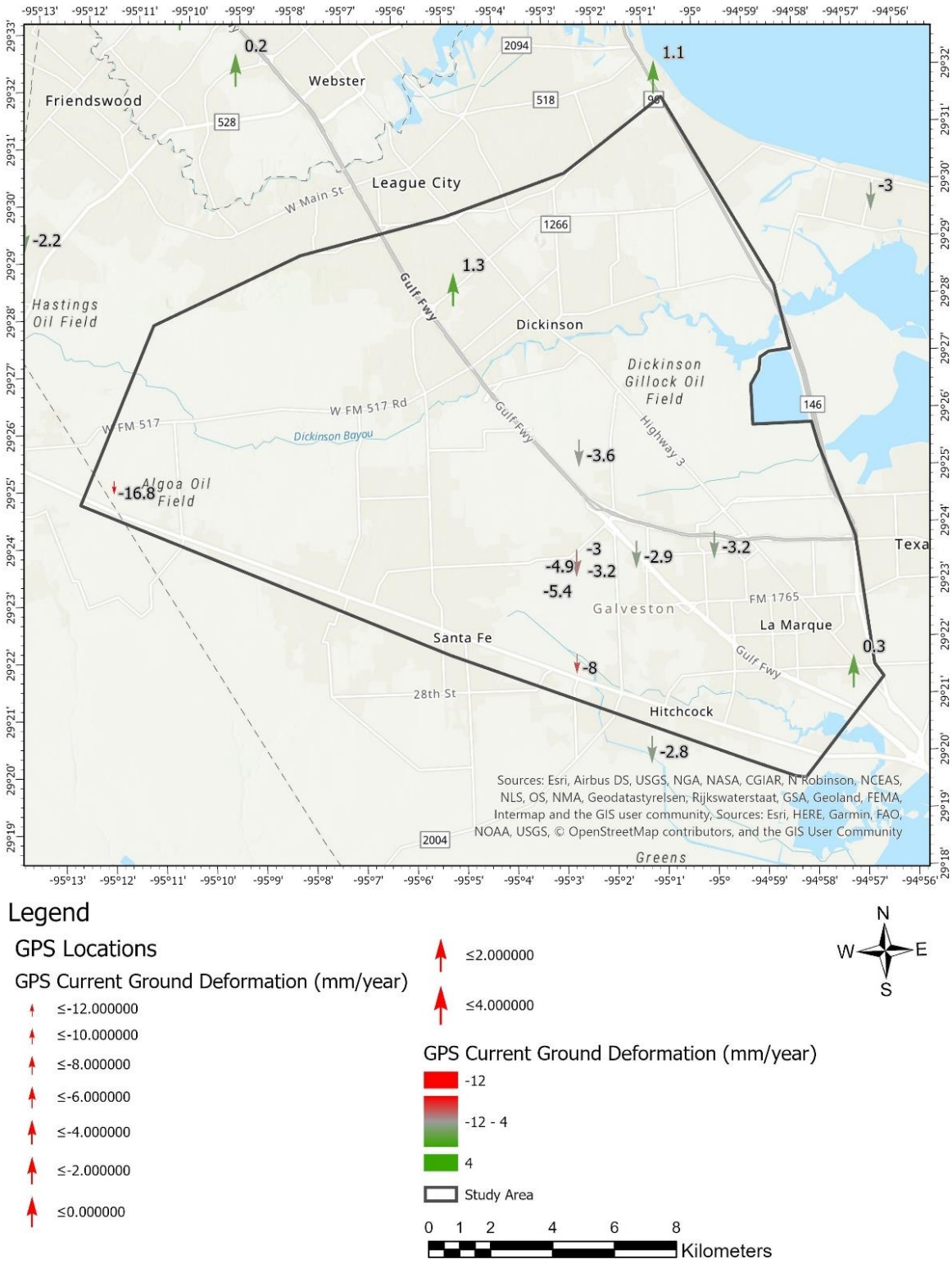

Figure 5-2: GPS Vertical Ground Deformation trends at GPS Locations in the Dickenson - La Marque area. Negative values display subsidence whereas positive values display uplift or swell.

In this study vertical displacement time-series plots for sites with data spanning from beginning of collection to 2020 were analyzed for ground deformation trends. The ground deformation trends are derived by applying a linear regression model to the vertical displacement time-series. Negative slopes represent land subsidence, whereas positive slope values represent land rebound or uplift. Individual displacement time-series graphs for each respective GPS station are provided in Appendix I.

Four of the GPS units are located at the University of Houston Coastal Center. These are part of the GPS Array and include units UHC0, UHC1, UHC2, and UHC3. Each antenna's name represents an estimate of the depth at which it is located: UHC1 has a base roughly 10 feet below the surface, UHC2's base is 20 feet below the surface, UHC3 is 30 feet below the surface and UHC0 is roughly one foot below the surface. Figure 5-3 provides the vertical time series plot for the UHCC GPS array. The GPS array shows a negative slope which is consistent with land subsidence. At 30 feet below the surface UHC3 is showing a subsidence rate of 4.88 mm per year. At both 10 and 20 feet below the surface there is a subsidence rate of 3.02 and 3.23 mm per year. The highest rate of subsidence of the array occurs at the surface or 1 foot below the ground surface at 5.42 mm per year, which is still a slow rate of subsidence for the area.

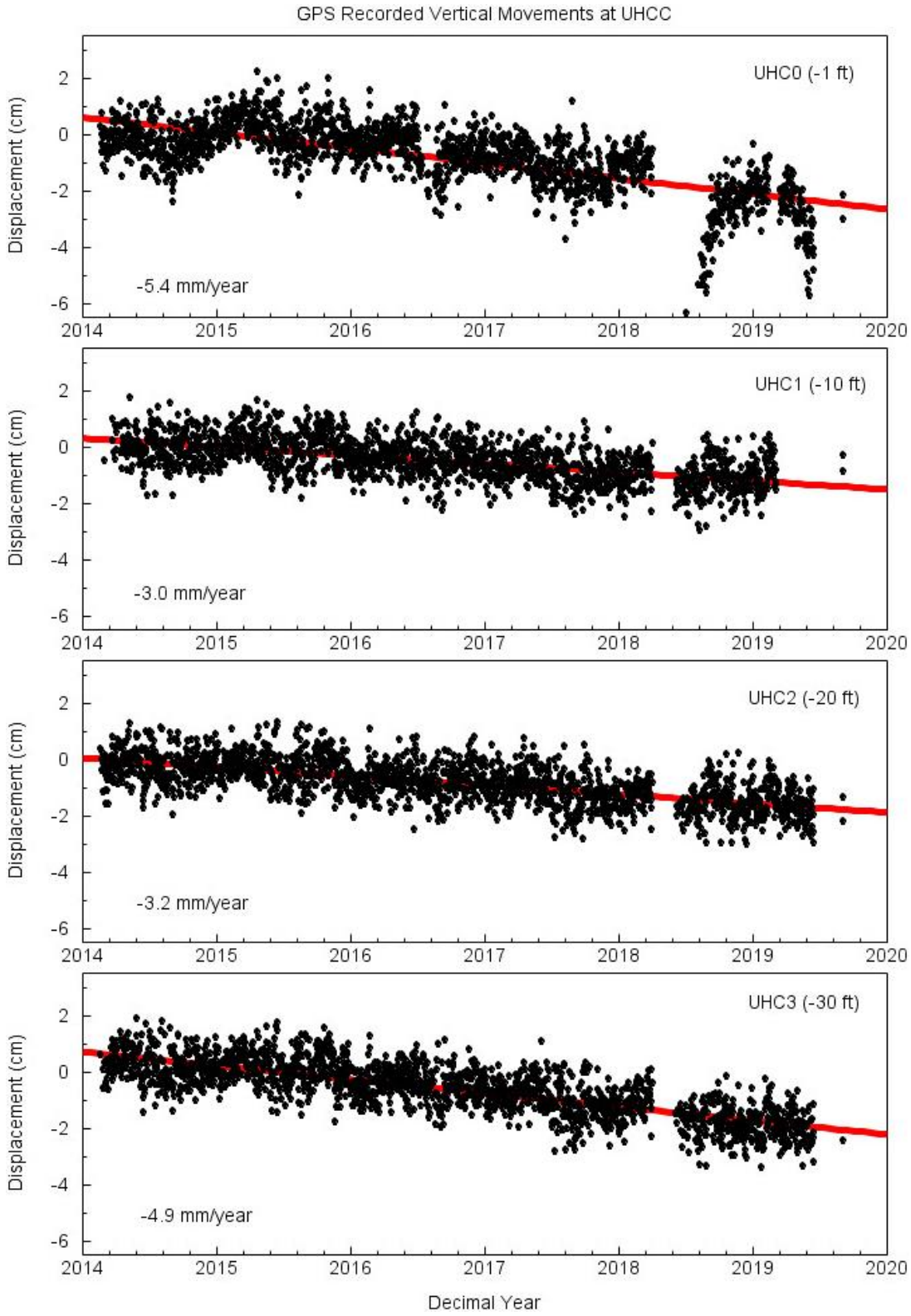

Figure 5-3: UHCC GPS Array Vertical Time Series analysis from installation to 2020. Negative values display subsidence whereas positive values display uplift or swell.

Closely spaced GPS units, like the UHCC GPS Array, share significant common errors and biases. The number of common errors and biases are decreased when the antenna-to-antenna distance is increased. To remove these errors and biases the double differential method is used in addition to precise point positioning (PPP) when evaluating vertical movement derived from the a GPS Array such as the one located at UHCC (Liu et al., 2019). Vertical displacement time series such as those displayed in Figure 5-3 are derived from the 24-hour precise point positioning (PPP) solutions with respect to Houston20 and a 24-hour carrier-phase double-difference (DD) solutions are with respect to UTEX, these are displayed in Figure 5-4 (Liu et al., 2019). The double-difference solution in Figure 5-4 is comparing the movement of the respected units in respect to UHC3 at 30 ft below the surface. Here, there is a display of swell in the middle sections of sediment. When looking at the data without double displacement this is hidden, and a slow subsidence rate is shown rather than a swell. Table 5-1 displays the linear trends of the times series of the GPS Array; DD denotes the double difference solution.

Table 5-1: Linear trends of UHCC GPS array

GPS Unit:	**Rate: (mm/year)**
UHC0:	-5.4
UHC1:	-3.0
UHC2:	-3.2
UHC3:	-4.9
UHC0 DD:	-2.1
UHC1 DD:	+1.6
UHC2 DD:	+1.6

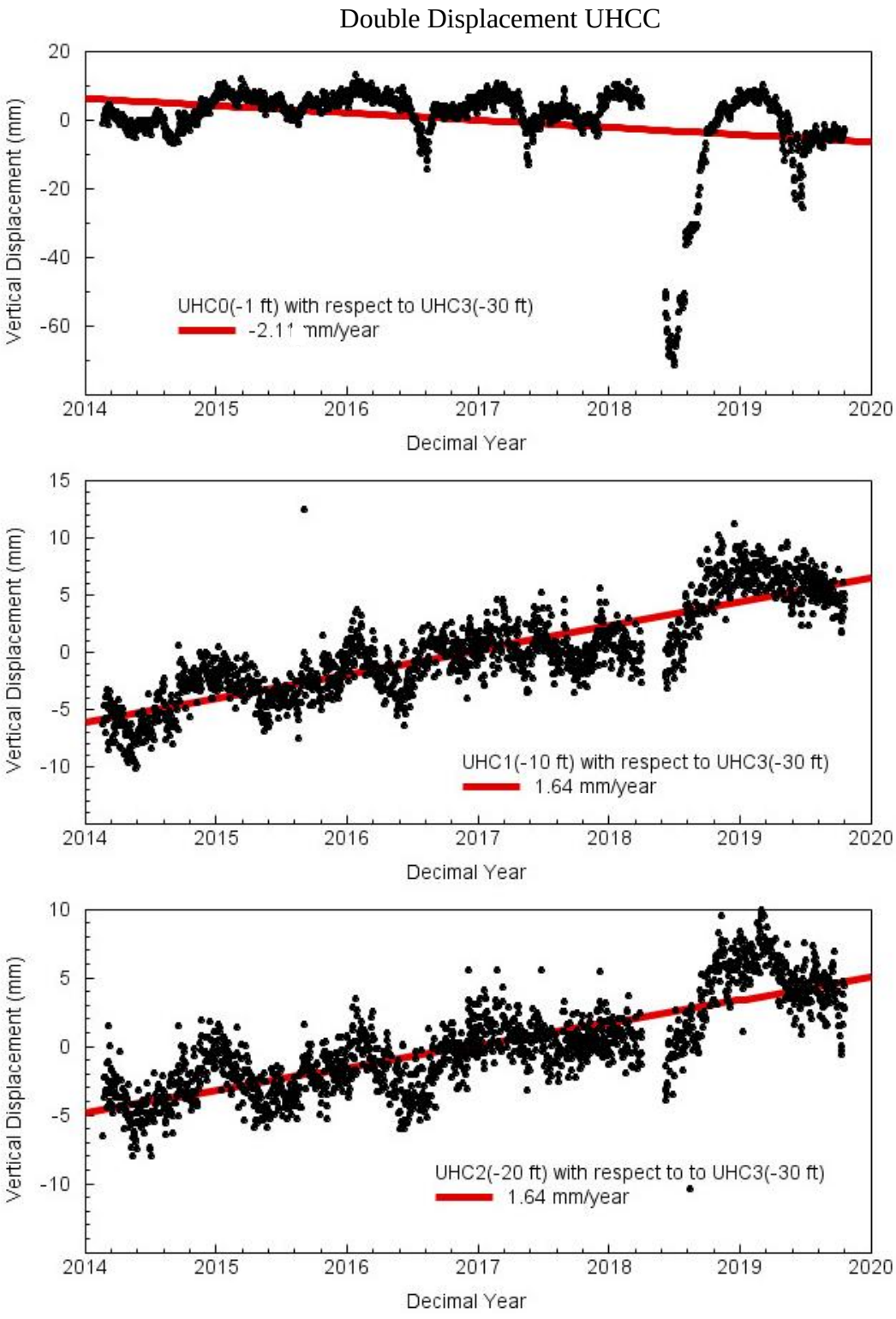

Figure 5-4: UHCC GPS Vertical Array Double Difference time series. GPS Array with respect to UHC3, 30 feet below the surface. Negative values display subsidence whereas positive values display uplift or swell.

Looking beyond the UHCC property subsidence there are areas of slowing subsidence of between 0.42 mm per year to 3.17 mm per year. Generally speaking, it appears that the subsidence in the Dickenson - La Marque area is slowing and converting to slight rebound depending on depth.

A map illustrating ground-deformation trends spatially throughout the area over the life of the units was generated by importing the regression data into ArcGIS Pro and then interpolating it throughout the region using the Inverse Distance Weighted (IDW) interpolation method shown in Figure 5-5. IDW is a weighted distance average therefore the average cannot be greater than the highest or lower than the lowest input values. Given the weighted average unless extremes are already sampled it will not create extremes (Watson and Philip, 1985). For the best results it is essential that sampling is dense and even, if not it may cause errors in the surface that is created (Watson and Philip, 1985). The map is colored to show the subsidence and rebound trends. Areas of subsidence are denoted by ranges of blue where dark blue represents the areas of slowest subsidence or swell (of about 1.5 mm per year max) and white represents the areas of subsidence.

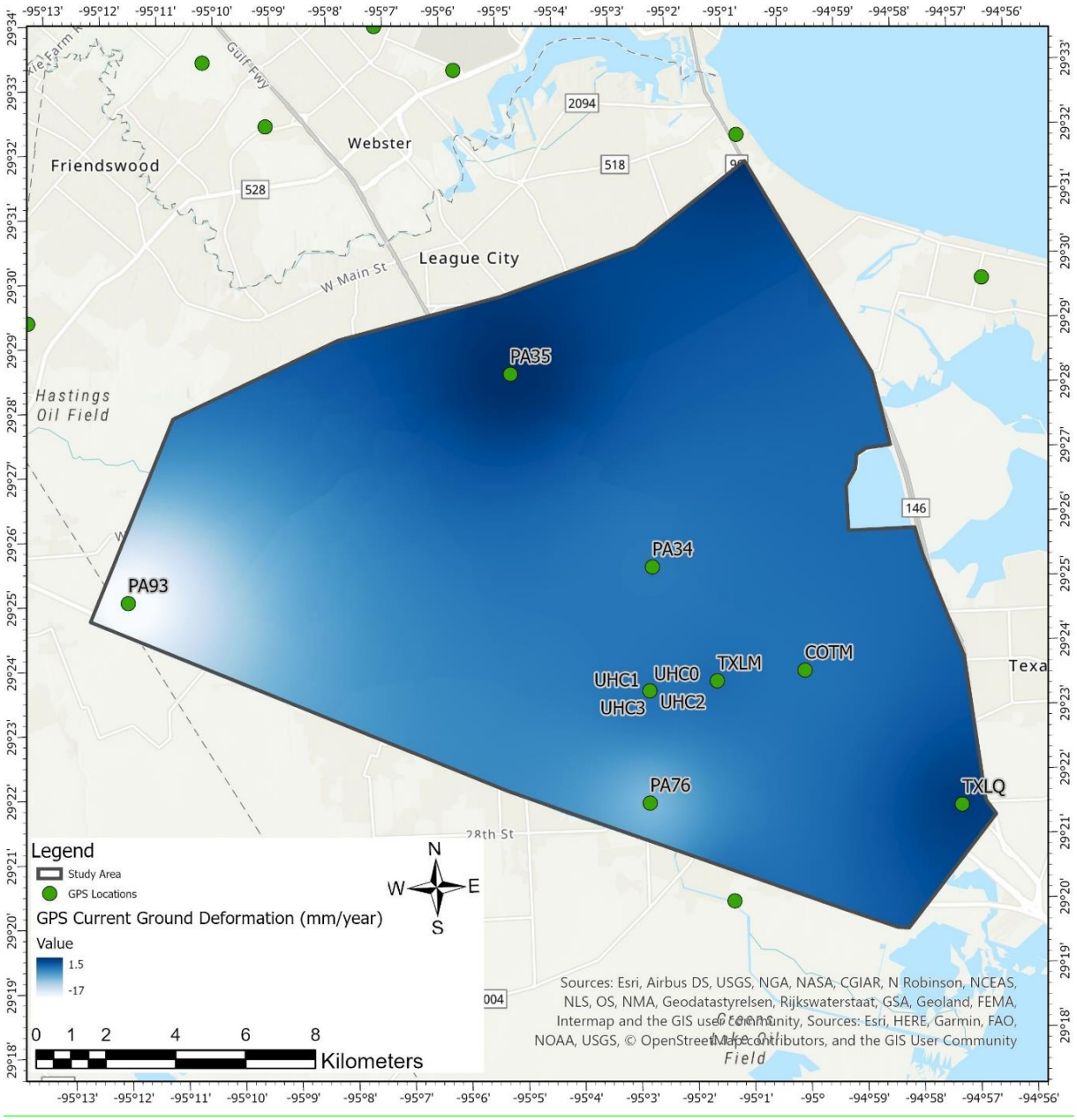

Figure 5-5: Potentiometric Surface of GPS derived current vertical ground deformation trends. Areas of dark blue represent areas with mitigated subsidence or swell and areas of white represent areas of subsidence.

5.2 Extensometer Compaction Data

In the Greater Houston area, the majority of the 13 borehole extensometers are located to the East and Southeast side of the City of Houston. Figure 3-15 displays the locations of all borehole extensometers in the Greater Houston area. Two sites, Clear Lake and Baytown have two extensometers completed at different depths to provide information about the depth where compaction is occurring. There are also a series of observational wells completed at each site to provide hydraulic head data from both the Chicot and Evangeline aquifers. For this study the borehole extensometers that will be used are the Texas City, Clear Lake, NASA, and Seabrook, which are displayed in Figure 5-6.

Figure 5-7 displays the long-period time-series (1962-2020) of aquifer compaction and groundwater head levels at the 4 extensometer sites. The rate of sediment compaction observed at each borehole extensometer site varies due to the varying ratios of subsurface sediments and rate of groundwater withdrawal (Kasmarek et al., 2012). At the four extensometer locations used in this study compaction has slowed, or even reversed, as groundwater heads have steadily risen over the past 35 to 40 years.

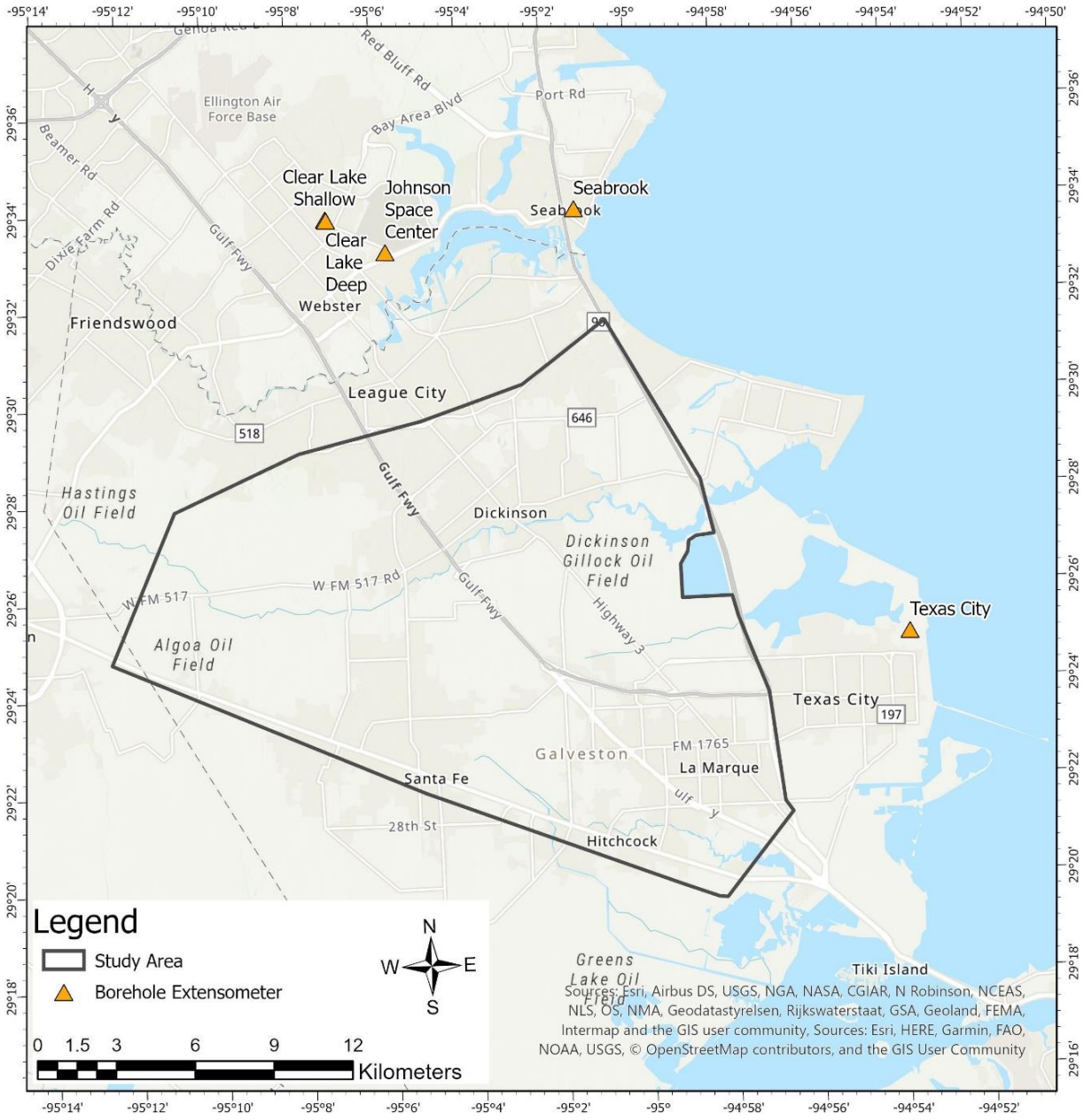

Figure 5-6: Location of the borehole extensometers used in this study.

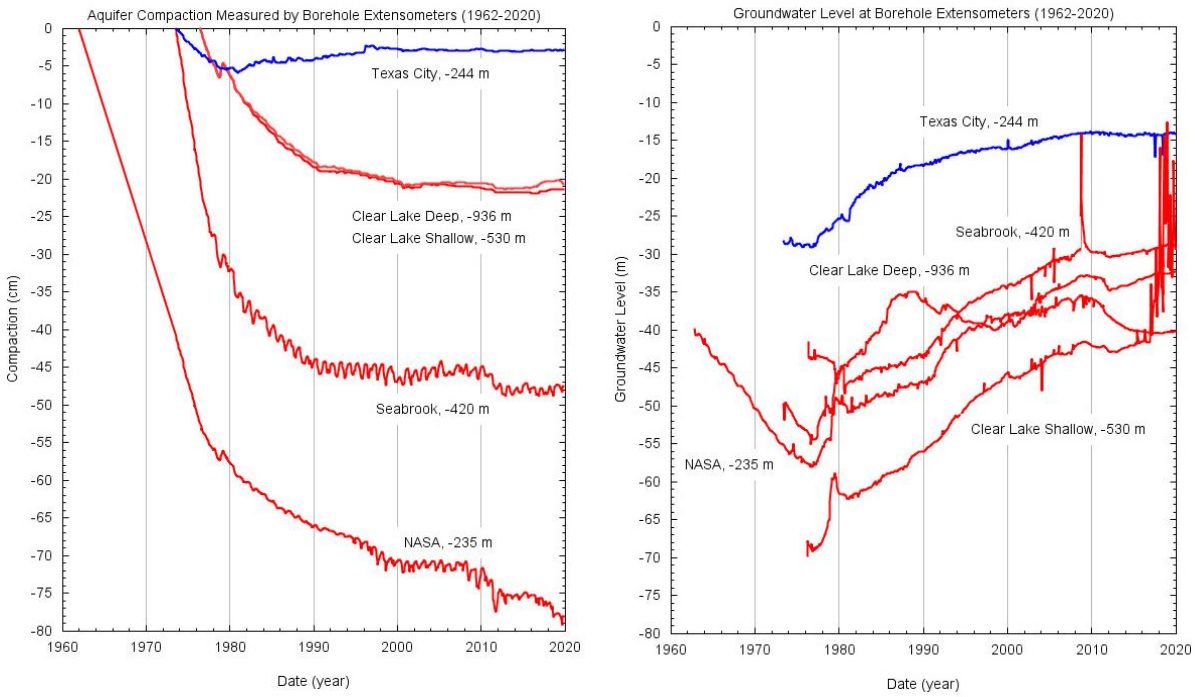

Figure 5-7: Plots depicting history of aquifer compaction (left) and corresponding groundwater head (right) at 4 extensometer sites close to the Dickenson - La Marque study area. The compaction depth of each extensometer is marked with the corresponding time-series. Blue and red lines represent boreholes that are completed within the Chicot and Evangeline aquifers, respectively.

Figure 5-8 A displays the compaction time-series for the two extensometers located in Clear Lake. Both extensometers at the Clear Lake location are completed within the Evangeline aquifer. The shallow extensometer is completed at 530 meters and the deep extensometer is completed at 936 meters below the land surface. These extensometers have recorded approximately the same amount of compaction between 1976 to 2020. This indicates that there was no significant aquifer compaction within the sediments between the 530- and 936-meter interval. This indicates that the compaction at the Clear Lake site occurs within sediments shallower than 530 m below the land surface, which includes the entire Chicot aquifer and the upper portion of the Evangeline aquifer. These observations provided by the Clear Lake

extensometers suggest that the majority of the compaction was limited to within the Chicot aquifer and the upper portion of the Evangeline aquifer.

The borehole extensometers located at both NASA and Seabrook, Figure 5-8 B and Figure 5-8 D respectively, have shown compaction which has slowed as hydraulic heads in the Chicot and Evangeline aquifers have increased from the time the site was established. Rapid aquifer compaction, which is greater than 2.5 cm per year, continued at these extensometer sites up until the late 1980s and early 1990s. After, aquifer compaction rates sharply decreased corresponding with the rising groundwater levels in both the Chicot and Evangeline aquifers. Currently, there is a component of inelastic compaction that can be seen at both sites due to the decreasing slope of compaction as a result of the increasing ground water level.

The Texas City extensometer is the only site that has seen a period of reversal of compaction. Initially, the Texas City extensometer displayed a rapid rate of compaction, greater than 2.5 cm per year, between the 1970's to the 1980's. Following the period of compaction, the Texas City extensometer experienced close to three centimeters of accumulated expansion between 1980 and 2000 as displayed in Figure 5-8 D. Hydraulic heads in both the Chicot and Evangeline aquifer have risen since 1977 at a rate of about 4 centimeters per year.

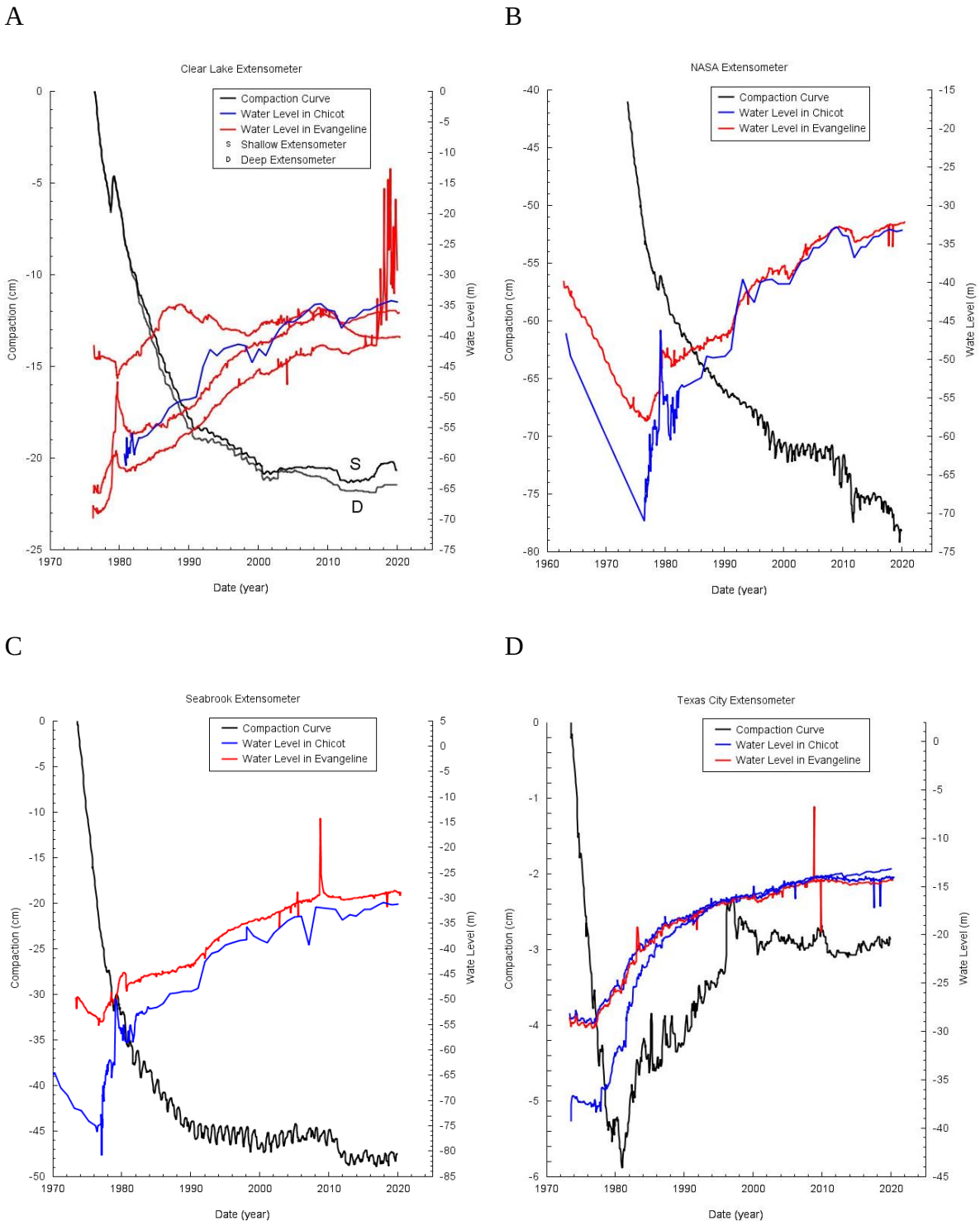

Figure 5-8: Extensometer compaction data plotted against measurements of the Chicot and Evangeline hydraulic heads from nearby observational wells.

5.3 Groundwater heads in the Chicot and Evangeline Aquifers

5.3.1 Derivation of Potentiometric Surface Contours

Data from local groundwater wells were analyzed for the derivation of the potentiometric surfaces of both the Chicot and Evangeline aquifer for 2000, 2005, 2010, 2015, and 2019. In the Chicot and Evangeline, a total of 33 and 21 wells were analyzed, respectively. These wells expand past the immediate study area to give a more detailed surface. A display of all the wells used to create the surface is displayed in Figure 3-11. The manual values of the Blue and Red well at UHCC are also included in the creation of the surface, the time series plot for these wells is displayed in Figure 5-9. Here we see that even though the two wells sit approximately 18 m away from each other they are completed in the same aquifer and have relatively similar groundwater levels. For each year, the average hydraulic head level was determined for each site. The position of all wells and their respective average hydraulic head levels were imported into ArcGIS Pro and interpolated using the IDW interpolation method. The interpolated potentiometric surface for the Chicot aquifer was used to create contours to represent the surface. These contours were overlain on the GPS derived vertical ground deformation data allowing for the clear analysis of the relationships between the change in hydraulic head levels and the ground deformation trends. Due to a lack of data coverage in the Dickenson - La Marque area, the Evangeline aquifer is evaluated at each well, respectively. The average hydraulic head level for each year is displayed as well as the GPS derived vertical ground deformation trend to make a clear analysis of the relationships between the change in hydraulic head levels and the ground deformation.

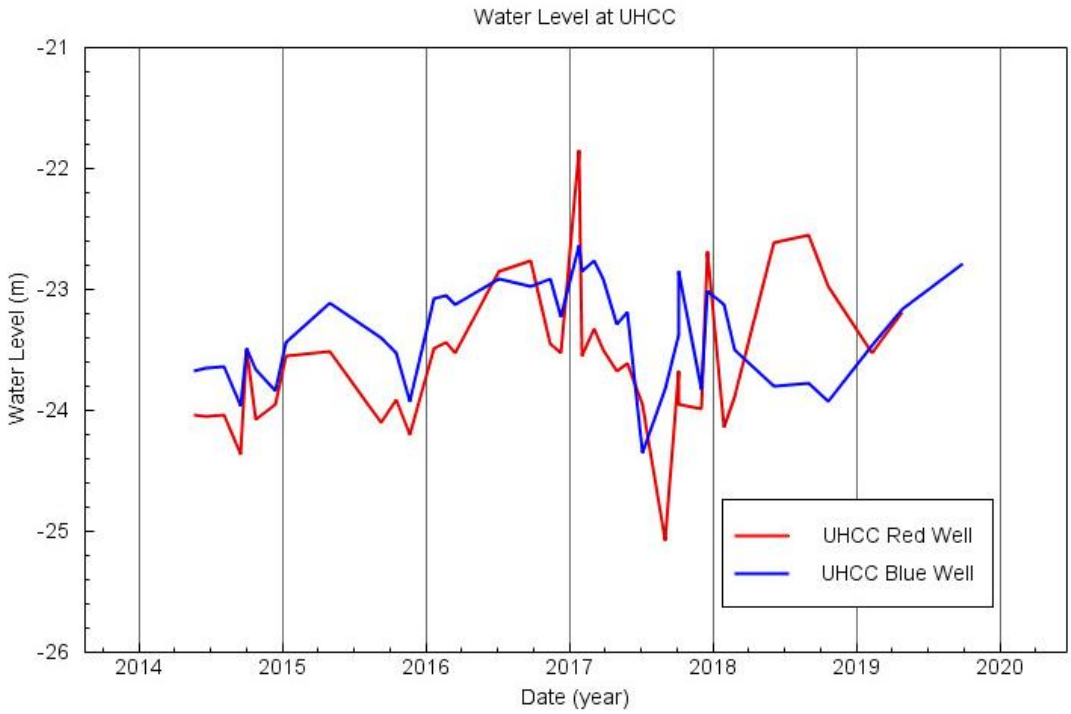

Figure 5-9: Groundwater levels below the surface for Red and Blue well located at UHCC. Wells are completed in the Chicot Aquifer and sit approximately 18 meters away from one another. Groundwater levels display negative values representing depth below the surface.

The Chicot aquifer surface determined as of 2000 is contoured in Figure 5-10. The contours show the groundwater levels in the aquifer during the year 2000 overlain on the current vertical GPS ground deformation trends. The aquifer contours display negative values representing depth below the surface. The hydraulic head levels of the Chicot aquifer are generally less than 35 meters below the land surface in the Greater Dickenson - La Marque area. The northwest corner of the study area exceeds 35 meters below land surface reaching 37 meters below the land surface. From the northwest to the southeast section of the Greater Dickenson - La Marque area the hydraulic head levels become shallower and mimic the sloping geometry towards the Gulf of Mexico.

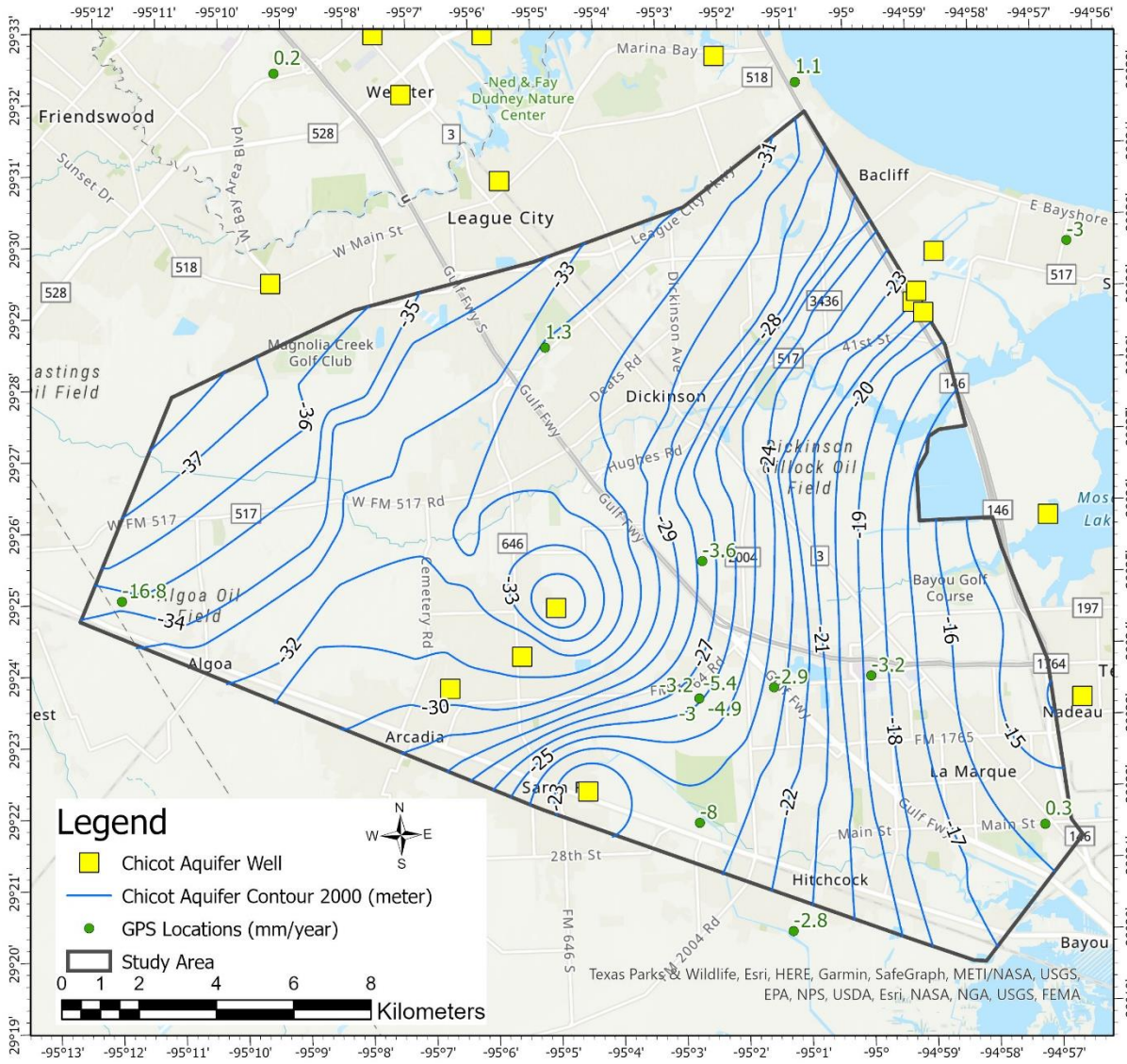

Figure 5-10: Chicot Aquifer hydraulic head levels in the year 2000. Contours show the groundwater levels in the aquifer during the year 2000 overlain on the current vertical GPS ground deformation trends. Aquifer contours display negative values representing depth below the surface. GPS negative values display subsidence while positive values display uplift or swell.

In order to see yearly and decade length groundwater change, the Chicot aquifer surface determined as of 2005 and 2010 is contoured in Figure 5-11 and Figure 5-12, respectively. The contours show the groundwater levels in the aquifer during the year 2005 and 2010 overlain on

the current vertical GPS ground deformation trends. The aquifer contours display negative values representing depth below the surface. In 2005 the hydraulic heads of the Chicot aquifer are less than 35 meters below the land surface in the Greater Dickenson - La Marque area. Whereas when evaluating the 2010 hydraulic head levels of the Chicot aquifer these were less than 34 meters below the surface with the hydraulic head levels being at about 35 meters below the surface on the boarder of the study area. Both in 2005 and 2010 from the northwest to the southeast section of the Greater Dickenson - La Marque area the hydraulic head levels become shallower and mimic the sloping geometry towards the Gulf of Mexico.

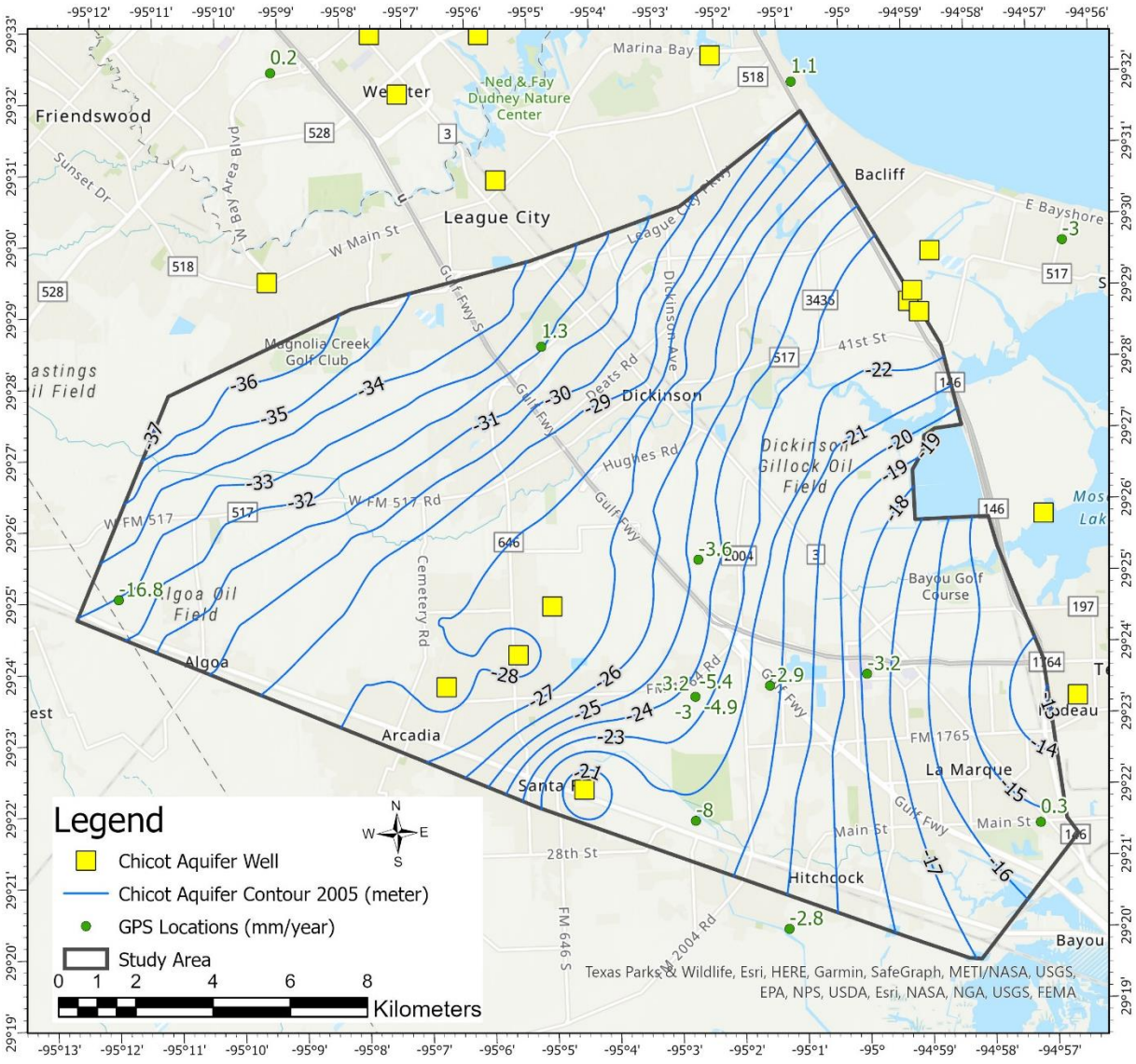

Figure 5-11: Chicot Aquifer hydraulic head levels in the year 2005. Contours show the groundwater levels in the aquifer during the year 2005 overlain on the current vertical GPS ground deformation trends. Aquifer contours display negative values representing depth below the surface. GPS negative values display subsidence while positive values display uplift or swell.

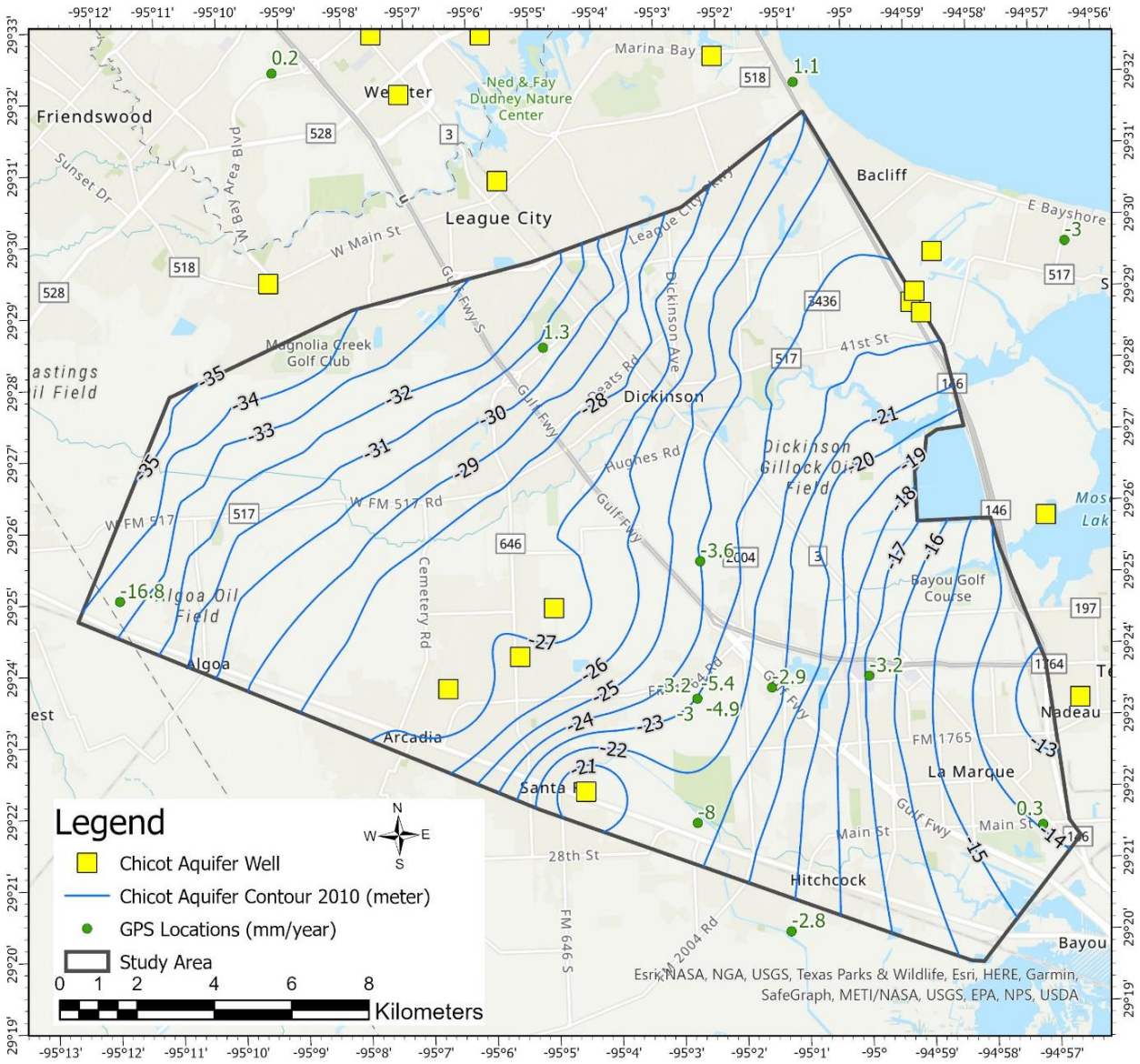

Figure 5-12: Chicot Aquifer hydraulic head levels in the year 2010. Contours show the groundwater levels in the aquifer during the year 2010 overlain on the current vertical GPS ground deformation trends. Aquifer contours display negative values representing depth below the surface. GPS negative values display subsidence while positive values display uplift or swell.

The Chicot aquifer surface determined as of 2015 is contoured in Figure 5-13. The contours show the groundwater levels in the aquifer during the year 2015 overlain on the current vertical GPS ground deformation trends. The aquifer contours display negative values

representing depth below the surface. The hydraulic head levels of the Chicot aquifer are generally less than 30 meters below the land surface in the Greater Dickenson - La Marque area. The northwest corner of the study area exceeds 30 meters below land surface reaching 35 meters below the land surface. From the northwest to the southeast section of the Greater Dickenson - La Marque area the hydraulic head levels become shallower and mimic the sloping geometry towards the Gulf of Mexico as it showed in 2010, 2005, and 2000.

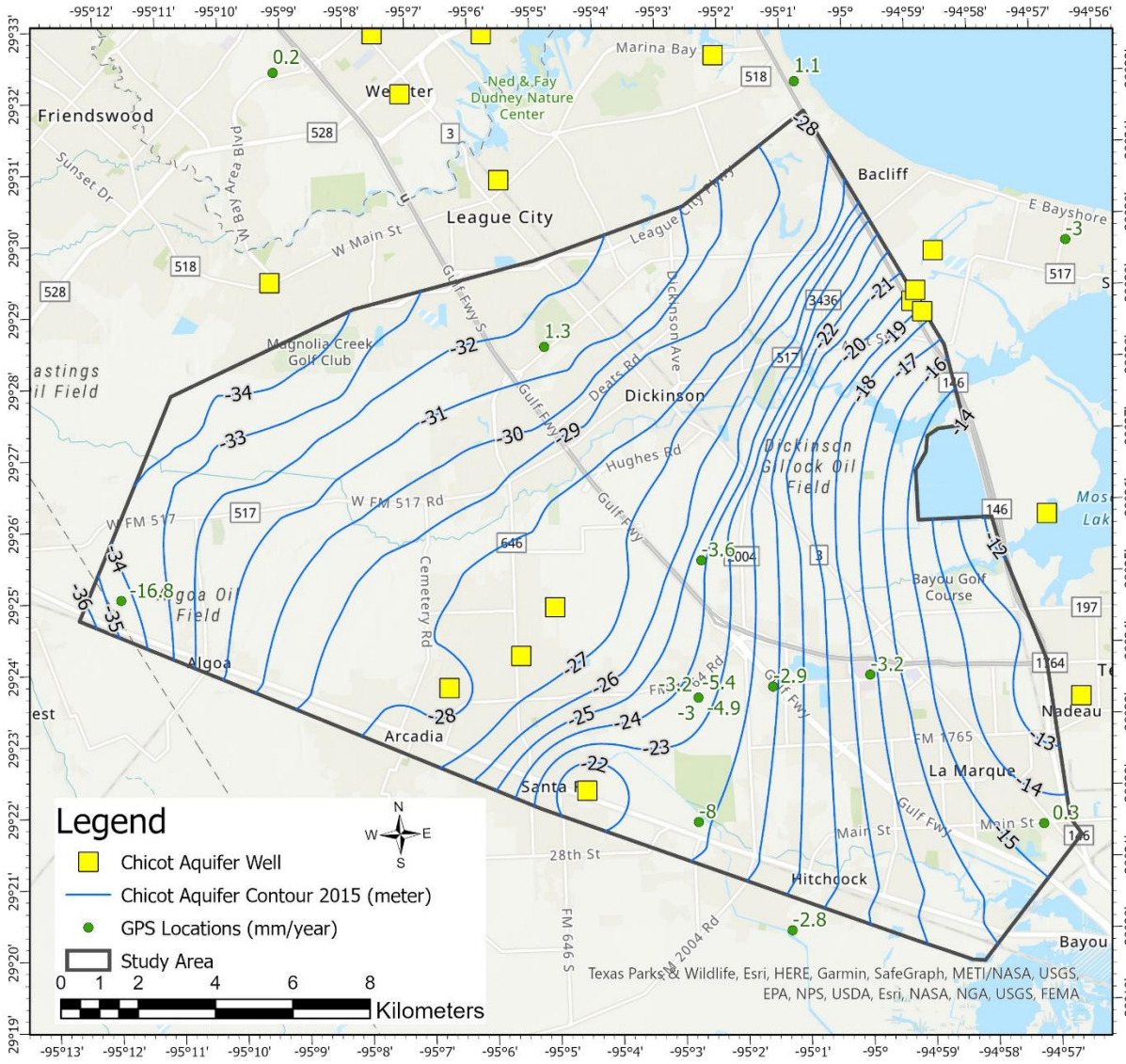

Figure 5-13: Chicot Aquifer hydraulic head levels in the year 2015. Contours show the groundwater levels in the aquifer during the year 2015 overlain on the current vertical GPS ground deformation trends. Aquifer contours display negative values representing depth below the surface. GPS negative values display subsidence while positive values display uplift or swell.

The Chicot aquifer surface determined as of 2019 is contoured in Figure 5-14. The contours show the groundwater levels in the aquifer during the year 2000 overlain on the current vertical GPS ground deformation trends. The aquifer contours display negative values representing depth below the surface. The hydraulic head levels of the Chicot aquifer are

generally less than 30 meters below the land surface in the Greater Dickenson - La Marque area. The northwest corner of the study area exceeds 30 meters below land surface reaching 35 meters below the land surface on the boarder of the study area. From the northwest to the southeast section of the Greater Dickenson - La Marque area the hydraulic head levels become shallower and mimic the sloping geometry towards the Gulf of Mexico similar to what was seen in the previous years.

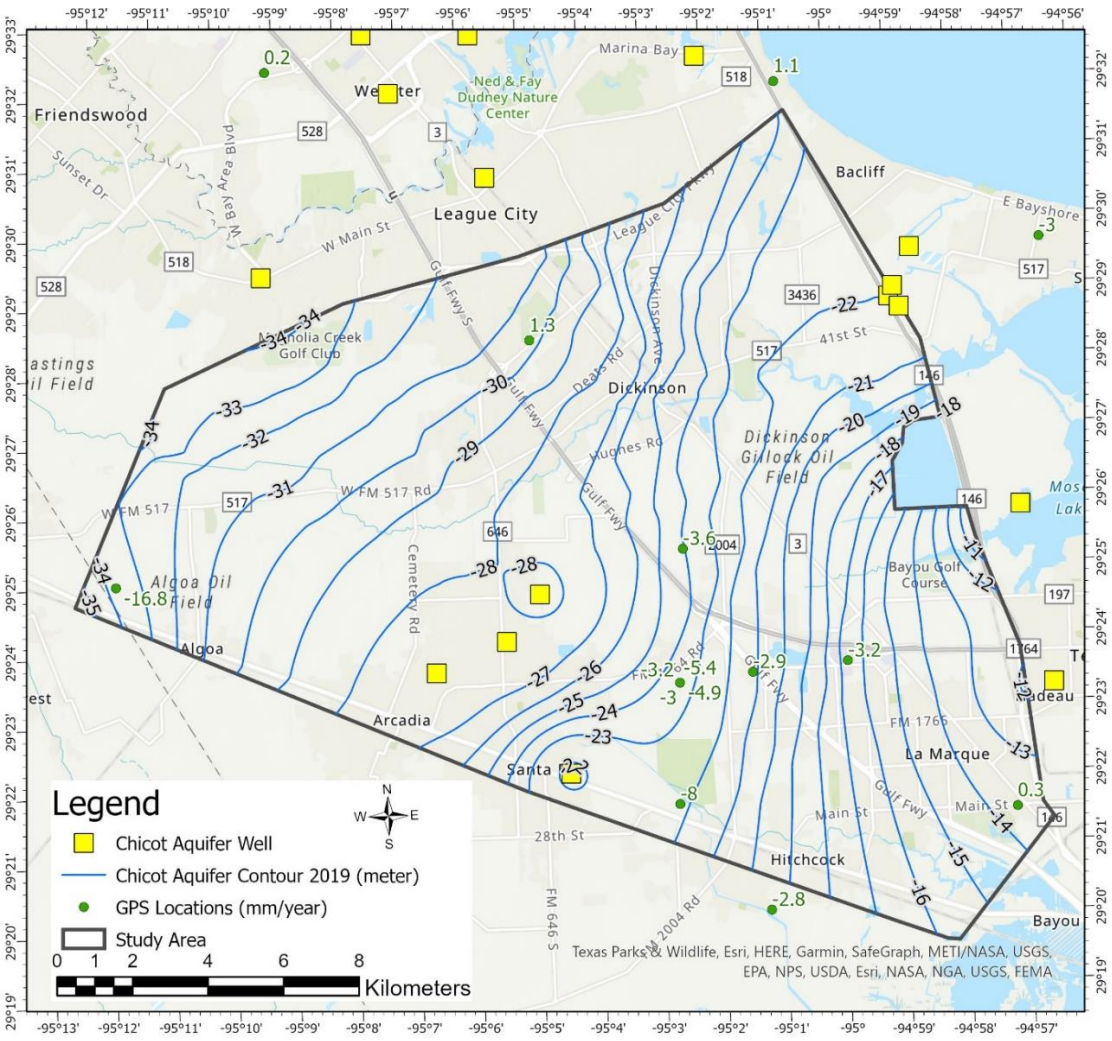

Figure 5-14: Chicot Aquifer hydraulic head levels in the year 2019. Contours show the groundwater levels in the aquifer during the year 2019 overlain on the current vertical GPS ground deformation trends. Aquifer contours display negative values representing depth below the surface. GPS negative values display subsidence while positive values display uplift or swell.

The Evangeline aquifer points determined as of 2000 are displayed in Figure 5-15. The arrows and color ramp show the groundwater levels in the aquifer during the year 2000 overlain with the current vertical GPS ground deformation trends. The aquifer positions display negative values representing depth below the surface. The Evangeline aquifer locations show the hydraulic head levels of the Evangeline aquifer are generally less than 40 meters below the land surface in the Greater Dickenson - La Marque area, specifically when evaluating the northeast points, which are collocated with GPS and borehole extensometer locations. In the area surrounding the study area the hydraulic heads range from 52 to 16 meters below the ground surface. From the west to the east section of the Greater Dickenson - La Marque area the hydraulic head levels become shallower towards the Gulf of Mexico, which accounts for the Texas City groundwater well reading of about 16 meters below the ground surface.

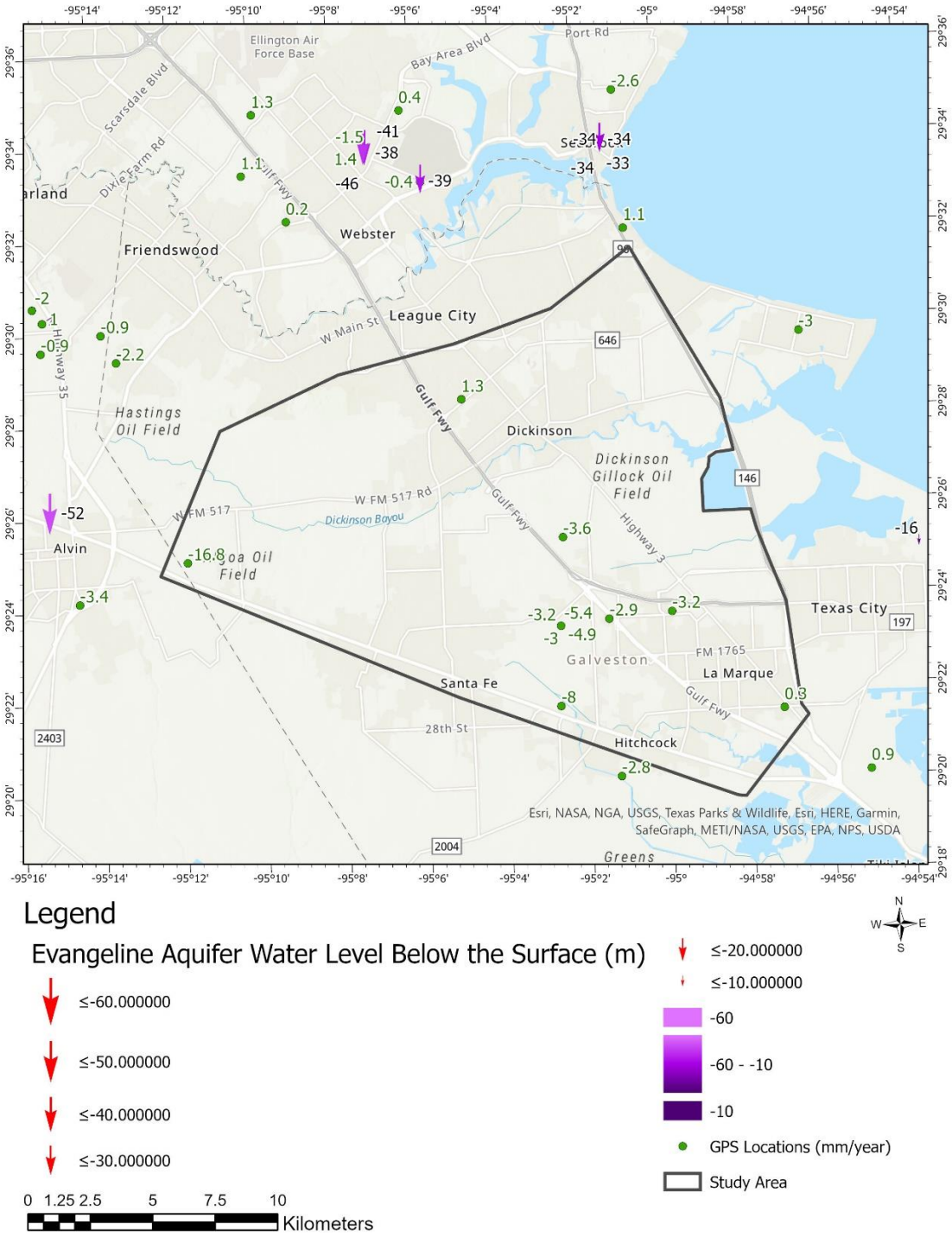

Figure 5-15: Evangeline Aquifer hydraulic head levels in the year 2000. Arrows and color ramp show the groundwater levels in the aquifer during the year 2000 overlain with the current vertical GPS ground deformation trends. Aquifer positions display negative values representing depth below the surface. GPS negative values display subsidence whereas positive values display uplift or swell.

The Evangeline aquifer points determined as of 2005 are displayed in Figure 5-16. The arrows and color ramp show the groundwater levels in the aquifer during the year 2005 overlain with the current vertical GPS ground deformation trends. The aquifer positions display negative values representing depth below the surface. The Evangeline aquifer locations show the hydraulic head levels of the Evangeline aquifer are generally less than 40 meters below the land surface in the Greater Dickenson - La Marque area, specifically when evaluating the northeast points, which are collocated with GPS and borehole extensometer locations. In the area surrounding the study area the hydraulic heads range from 51 to 15 meters below the ground surface. From the west to the east section of the Greater Dickenson - La Marque area the hydraulic head levels become shallower towards the Gulf of Mexico. The 2005 aquifer levels are similar to those in 2000

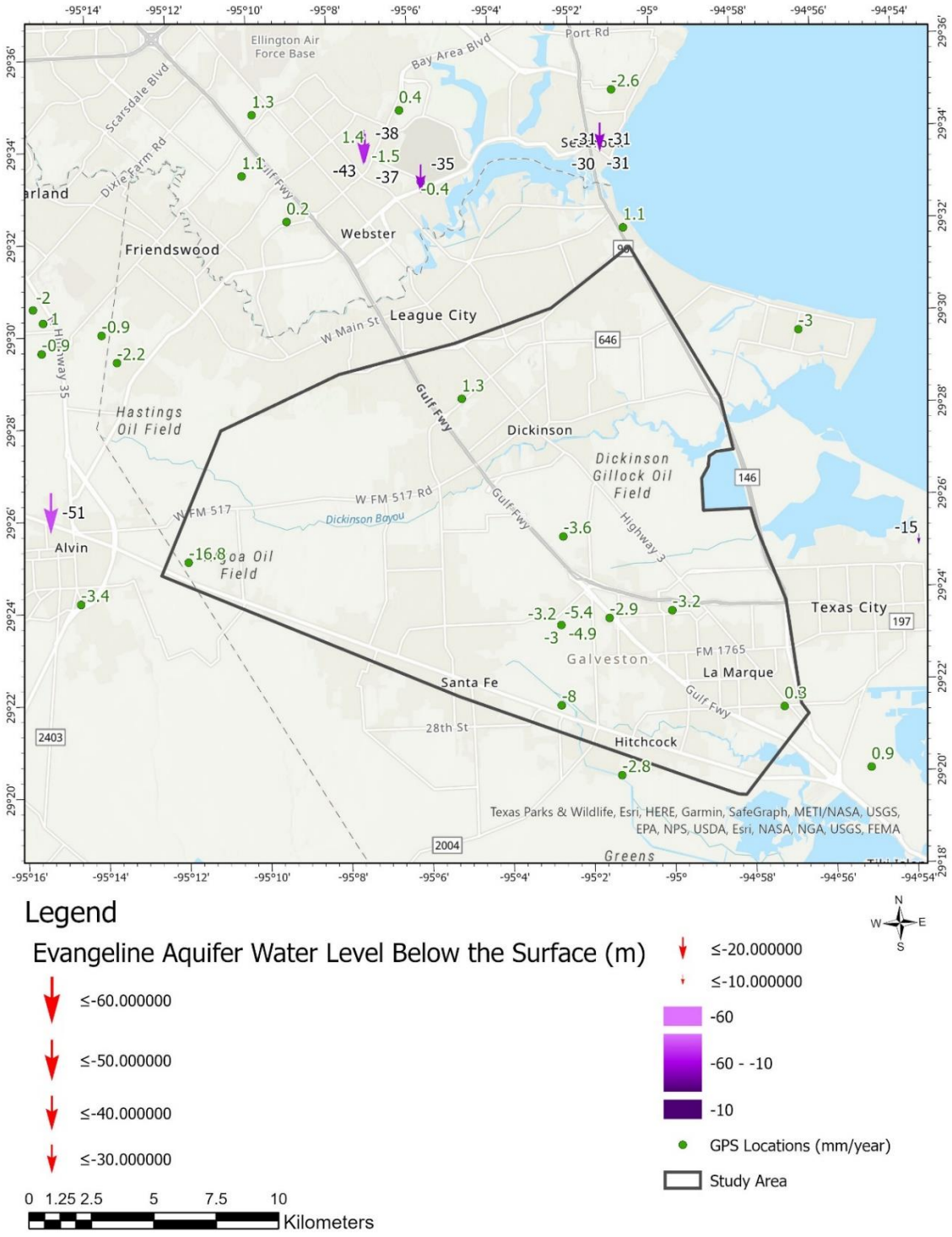

Figure 5-16: Evangeline Aquifer hydraulic head levels in the year 2005. Arrows and color ramp show the groundwater levels in the aquifer during the year 2005 overlain with the current vertical GPS ground deformation trends. Aquifer positions display negative values representing depth below the surface. GPS negative values display subsidence whereas positive values display uplift or swell.

The Evangeline aquifer points determined as of 2010 are displayed in Figure 5-17. The arrows and color ramp show the groundwater levels in the aquifer during the year 2010 overlain with the current vertical GPS ground deformation trends. The aquifer positions display negative values representing depth below the surface. The Evangeline aquifer locations show the hydraulic head levels of the Evangeline aquifer are generally less than 40 meters below the land surface in the Greater Dickenson - La Marque area, specifically when evaluating the northeast points, which are collocated with GPS and borehole extensometer locations. In the area surrounding the study area the hydraulic heads range from 47 to 15 meters below the ground surface. From the west to the east section of the Greater Dickenson - La Marque area the hydraulic head levels become shallower towards the Gulf of Mexico.

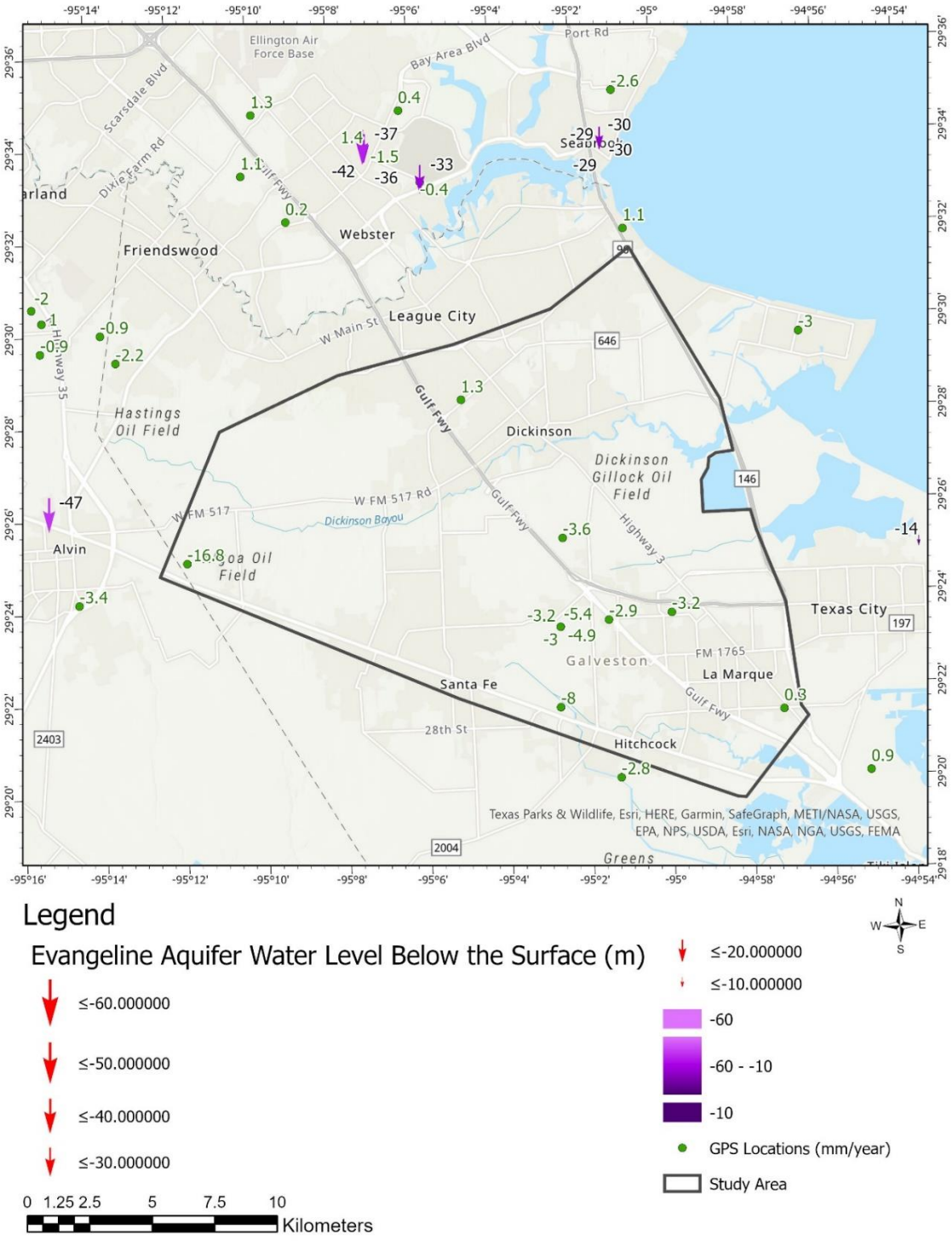

Figure 5-17: Evangeline Aquifer hydraulic head levels in the year 2010. Arrows and color ramp show the groundwater levels in the aquifer during the year 2010 overlain with the current vertical GPS ground deformation trends. Aquifer positions display negative values representing depth below the surface. GPS negative values display subsidence whereas positive values display uplift or swell.

The Evangeline aquifer points determined as of 2015 are displayed in Figure 5-18. The arrows and color ramp show the groundwater levels in the aquifer during the year 2015 overlain with the current vertical GPS ground deformation trends. The aquifer positions display negative values representing depth below the surface. The Evangeline aquifer locations show the hydraulic head levels of the Evangeline aquifer are generally less than 40 meters below the land surface in the Greater Dickenson - La Marque area, specifically when evaluating the northeast points, which are collocated with GPS and borehole extensometer locations. In the area surrounding the study area the hydraulic heads range from 45 to 15 meters below the ground surface. From the west to the east section of the Greater Dickenson - La Marque area the hydraulic head levels become shallower towards the Gulf of Mexico, as seen in the previous years.

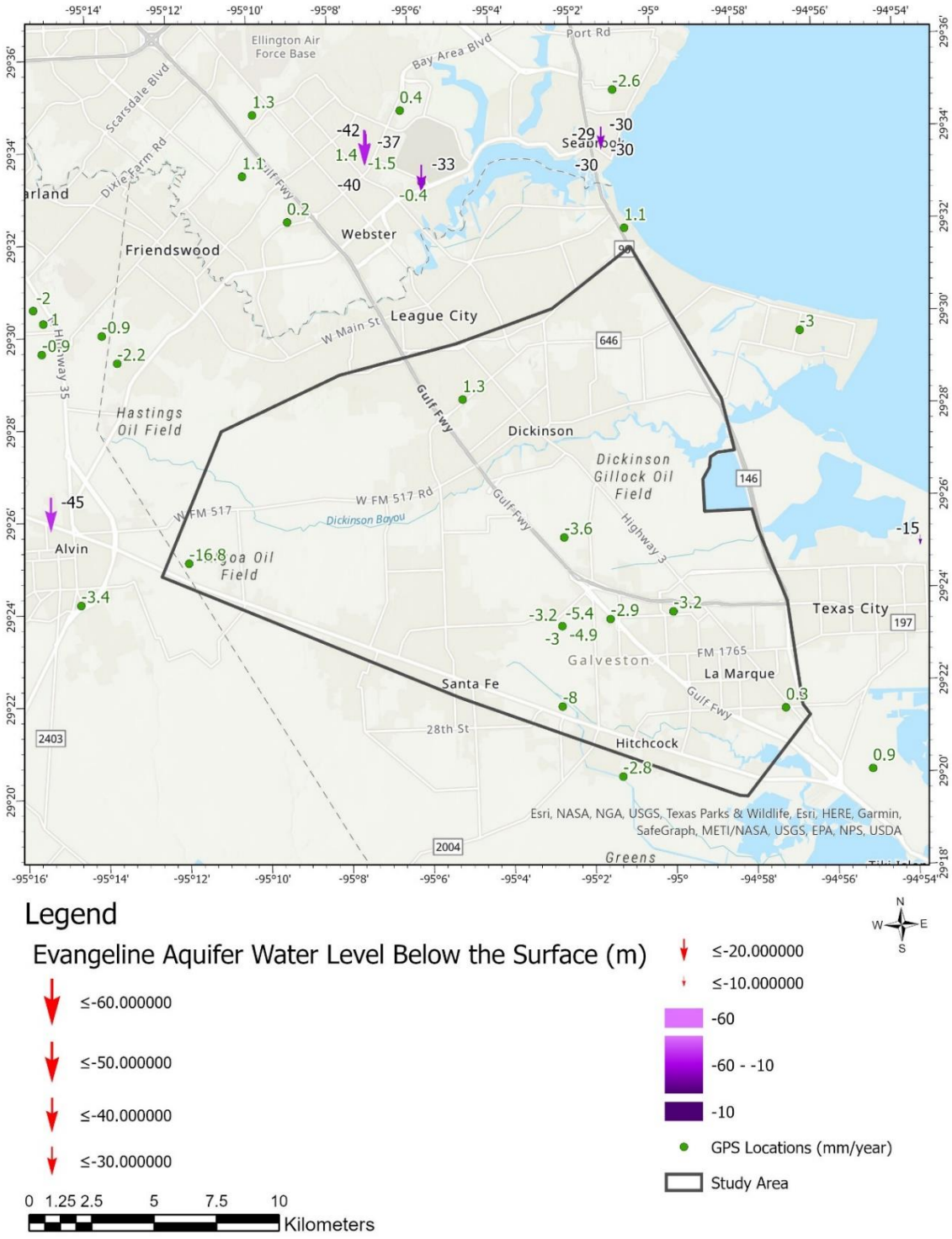

Figure 5-18: Evangeline Aquifer hydraulic head levels in the year 2015. Arrows and color ramp show the groundwater levels in the aquifer during the year 2015 overlain with the current vertical GPS ground deformation trends. Aquifer positions display negative values representing depth below the surface. GPS negative values display subsidence whereas positive values display uplift or swell.

The Evangeline aquifer points determined as of 2019 are displayed in Figure 5-19. The arrows and color ramp show the groundwater levels in the aquifer during the year 2019 overlain with the current vertical GPS ground deformation trends. The aquifer positions display negative values representing depth below the surface. The Evangeline aquifer locations show the hydraulic head levels of the Evangeline aquifer are generally less than 40 meters below the land surface in the Greater Dickenson - La Marque area, specifically when evaluating the northeast points, which are collocated with GPS and borehole extensometer locations. In the area surrounding the study area the hydraulic heads range from 47 to 14 meters below the ground surface. From the west to the east section of the Greater Dickenson - La Marque area the hydraulic head levels become shallower towards the Gulf of Mexico, as seen in the previous years.

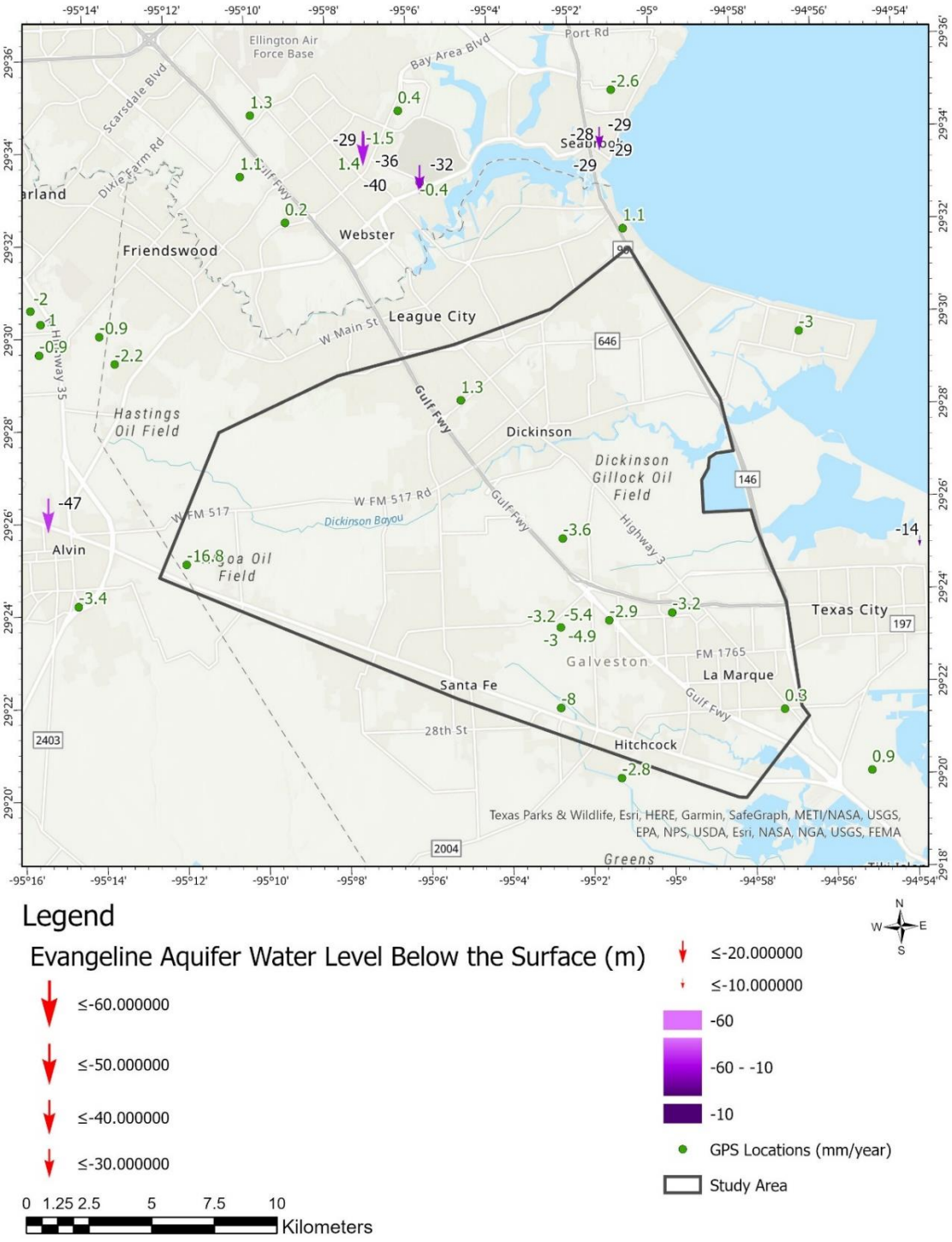

Figure 5-19: Evangeline Aquifer hydraulic head levels in the year 2019. Arrows and color ramp show the groundwater levels in the aquifer during the year 2019 overlain with the current vertical GPS ground deformation trends. Aquifer positions display negative values representing depth below the surface. GPS negative values display subsidence whereas positive values display uplift or swell.

When looking at the trends of the data over the past two decades, it reveals the general increase in the hydraulic head levels. Figure 5-20 displays the contours of the change in hydraulic head levels of the Chicot aquifer between 2000 and 2019. Change in hydraulic head levels was calculated over two decades, a single decade and in divisions of about 5 years. This was created by utilizing the difference function in ArcGIS Pro. Throughout the study area, the change in the location of the hydraulic head was small and rose between one and six meters. The area with 6 meters of increase is collocated with a Chicot aquifer groundwater well. Areas with slowing subsidence had hydraulic head levels raise in total between one and three meters. Also, when looking at the area off to the western corner of the study area with close to 16 mm per year of subsidence, there is only about a two-meter raise in the hydraulic head level. Therefore, the areas of greatest subsidence and rebound experienced little to no rise in the hydraulic head of the Chicot aquifer.

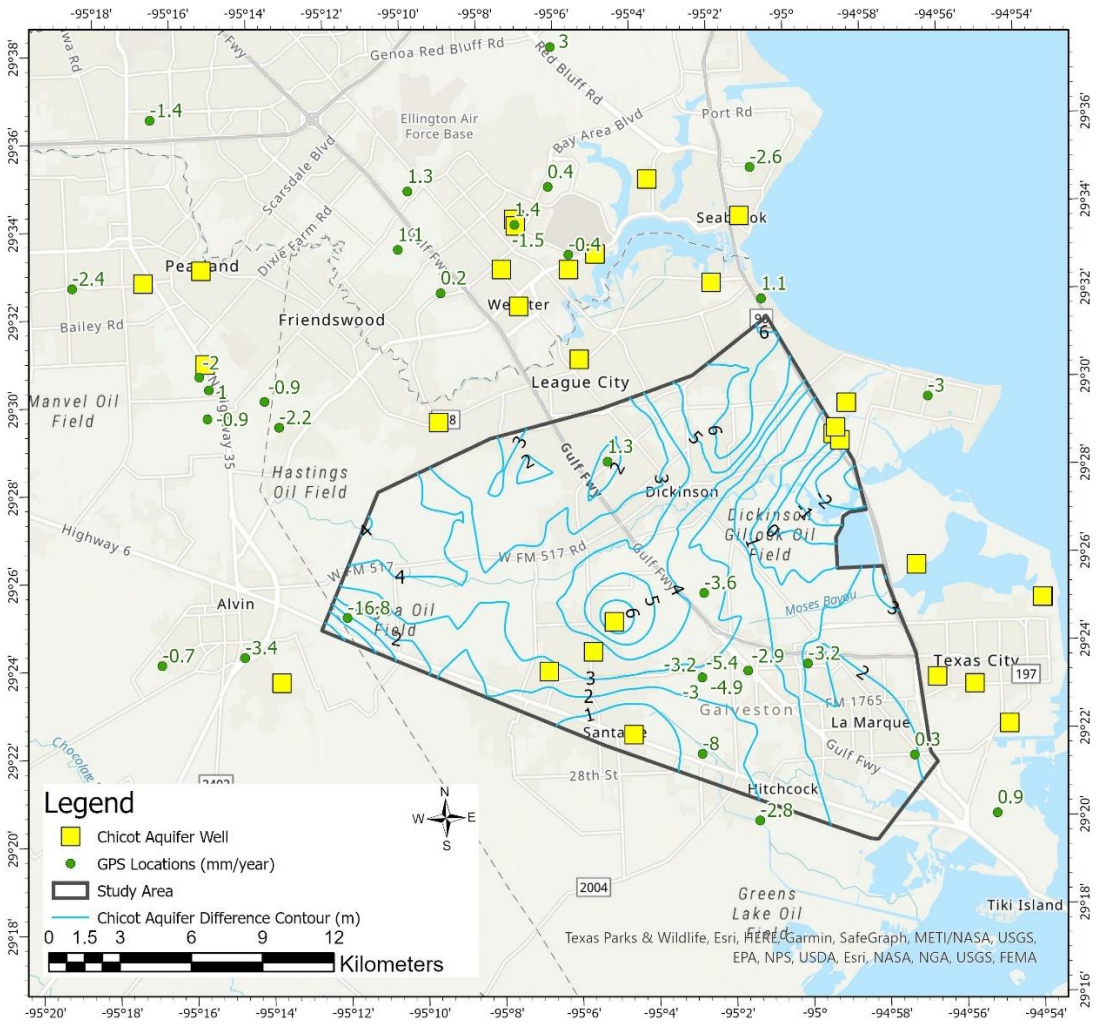

Figure 5-20: Change in hydraulic head levels of the Chicot Aquifer between the years of 2019 and 2000 derived by finding the difference between the hydraulic head levels of 2019 and 2000. Contours show the change in groundwater levels in the aquifer overlain on the current vertical GPS ground deformation trends. Aquifer contours display negative values representing a decrease in hydraulic head levels. Positive values represent an increase in hydraulic head levels. GPS negative values display subsidence while positive values display uplift or swell.

When looking at the trends of the data on a smaller scale, about 5-year periods, it reveals the small steppingstone changes in hydraulic head levels. Figure 5-21 displays the contours of change in hydraulic head levels between 2005 and 2000. The area with the largest change in hydraulic head levels is collocated with a Chicot aquifer well location. Overall, the changes in

hydraulic head levels are similar to that in Figure 5-20 and there is a similar decrease in hydraulic head levels along the coast in the northeast section of the study area.

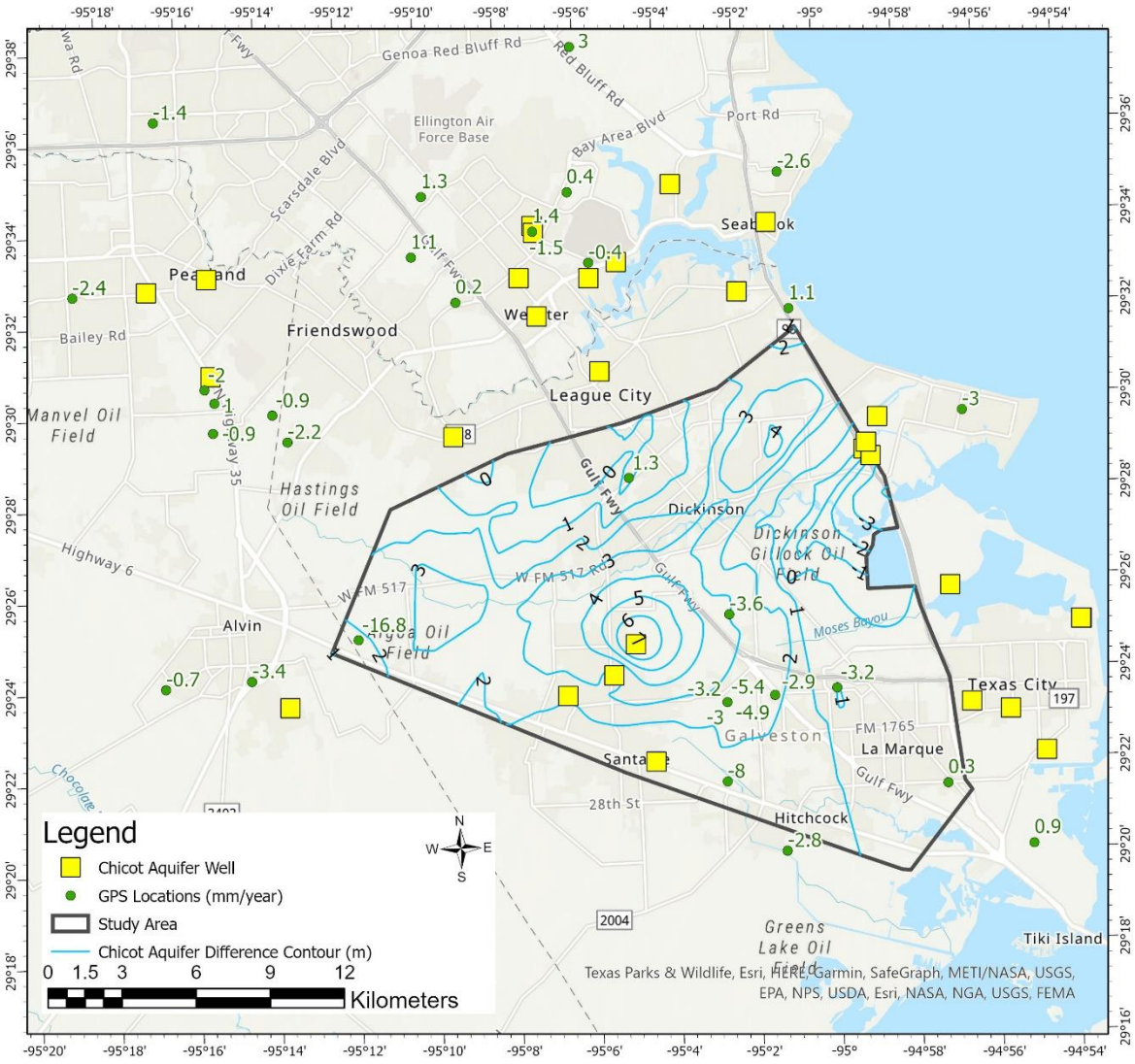

Figure 5-21: Change in hydraulic head levels of the Chicot Aquifer between the years of 2005 and 2000 derived by finding the difference between the hydraulic head levels of 2005 and 2000. Contours show the change in groundwater levels in the aquifer overlain on the current vertical GPS ground deformation trends. Aquifer contours display negative values representing a decrease in hydraulic head levels. Positive values represent an increase in hydraulic head levels. GPS negative values display subsidence while positive values display uplift or swell.

Figure 5-22 displays the values of the change in hydraulic head levels of the Evangeline aquifer between 2000 and 2019 at the Evangeline aquifer well locations surrounding the study area. This was created by utilizing the difference function in ArcGIS Pro. Throughout the study area, the change of the hydraulic head levels rose between two and six meters. The areas showing the most rapid subsidence of the area and the change of hydraulic head levels do not show a visual correlation in the Evangeline aquifer. When looking on a decade scale there was a maximum change of 12 meters. These sharp changes again are attributed to the lack of data available in the area. The same area shows a change of about 0.6 meters of hydraulic head rise and is confirmed by the three other Evangeline Aquifer wells available information. When looking at the trends of the data on a smaller scale, about 5-year periods, it reveals the small steppingstone changes in hydraulic head level., these are displayed in Appendix III. Between each year there were small changes in hydraulic head levels but there was an overall increase in a decade or two decades time.

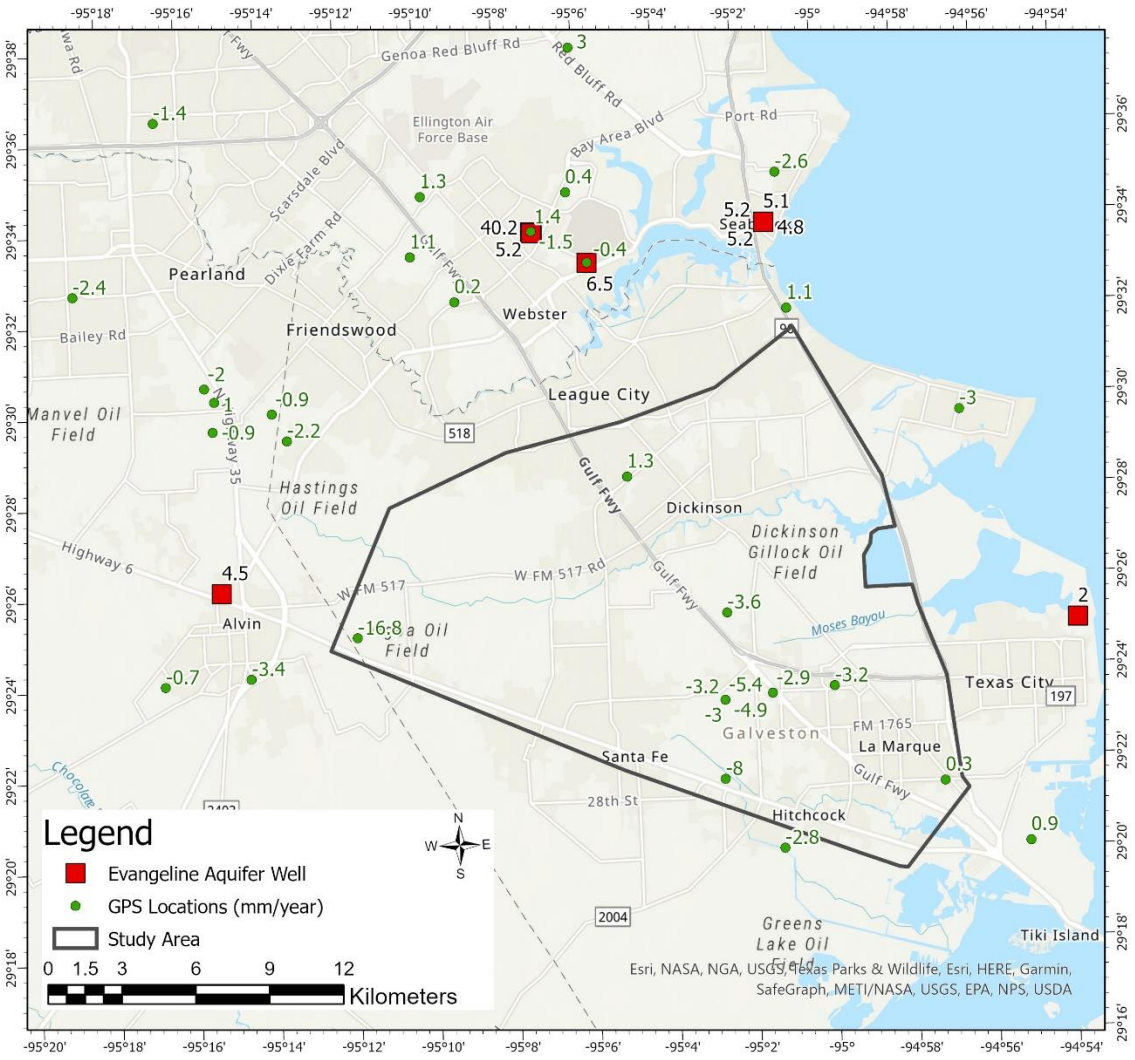

Figure 5-22: Change in hydraulic head levels of the Evangeline Aquifer between the years of 2019 and 2000 derived by finding the difference between the hydraulic head levels of 2019 and 2000. Points show the change in groundwater levels in the aquifer overlain on the current vertical GPS ground deformation trends. Aquifer contours display negative values representing a decrease in hydraulic head levels. Positive values represent an increase in hydraulic head levels. GPS negative values display subsidence while positive values display uplift or swell.

In conclusion, from the data presented there is not a simple or direct correlation between ground deformation and hydraulic head fluctuations in the Dickenson - La Marque area. However, it is important to note that there is a steady increase in hydraulic head levels over the

course of the course of the study duration. In order to fully understand the relationship between ground deformation and hydraulic head levels, the focus needs to shift to the preconsolidation heads.

5.4 Preconsolidation Head Level in the Dickenson – La Marque Area

5.4.1 Previous Work

In 1981 Holzer completed an investigation of the preconsolidation heads in several regions throughout the United States, including the Houston area. Holzer evaluated the ratio of subsidence per unit drop in hydraulic head levels during the beginning of human-induced groundwater production. Each of the sites examined in the region displayed a bilinear relationship between the ratio of subsidence and the water-level decline. Holzer interpreted this bilinear relationship to be a result of the change from elastic to inelastic compaction after hydraulic heads were lowered past the preconsolidation head levels which can cause irreversible subsidence. Initially, aquifer conditions were believed to have been naturally over consolidated. Following groundwater pumping, the initial subsidence per water level decline was considered to match with elastic compaction and the shallower slope of the relationship curve between rate of subsidence and water level decrease. A sharp increase in the subsidence per water level decline resulted in a steep slope and indicated the beginning of inelastic compaction (Holzer, 1981).

In the Houston area, Holzer examined five leveling benchmark sites with nearby well data. These were located towards the Houston Ship Channel. Holzer noted that the predevelopment preconsolidation heads in the area ranged from 31 to 63 meters below the land surface in the Chicot aquifer.

5.4.2 Estimation of Preconsolidation Head

Preconsolidation heads are often estimated through the analysis of groundwater and compaction data or derived through groundwater flow modeling (Galloway et al., 1999). This study aims to utilize available groundwater data in addition to vertical displacement and compaction data from local GPS, wells, and extensometer sites to estimate preconsolidation heads in the Dickenson La-Marque area to better understand the compaction of shallow sediments. Hydraulic-head levels at the onset of rebound or slowing of compaction will be considered to coincide with the preconsolidation-head levels which will be referenced from the compaction curves in Chapter 5. The extensometer data in the area does show the slowing of subsidence since the establishment of the extensometer sites, but there continues to be inelastic compaction occurring. During the early 2000's, there was a rapid slowing of compaction that occurred and even rebound in the area surrounding the Texas City extensometer. This indicates that the hydraulic head levels in those areas are close to reaching the preconsolidation levels. For this study, the year 2000 will serve as the approximate timing of the onset of rebound in the Dickenson - La Marque area.

The general estimate of the preconsolidation head is made by creating the potentiometric surfaces of both the Chicot and Evangeline aquifers during 2000 and analyzing them. The study area has subsidence rates of between 1 and 2 millimeters per year. The Chicot hydraulic heads are between 15 - 37 meters below the surface. When looking at the Evangeline aquifer the hydraulic heads ranged from 33.1 – 51.6 meters below the ground surface. When comparing this to previous studies and documentation from Chapter 1 of the Greater Houston area subsidence as well as Holzer study a one-millimeter rate of subsidence is likely attributed to the inelastic compaction of sediments. When looking at the preconsolidation head that was derived

by Holzer in 1981, the preconsolidation head that was derived was 31 meters below ground surface. This ranged from 0 to 15 meters of the hydraulic head levels of the Evangeline and Chicot aquifer. As noted above the closest location of Holzer's preconsolidation head is outside the study area close to the Houston Ship channel. Given that the preconsolidation head that Holzer arrived at was between 0 and 15 meters of difference there is some credibility of the 2000 hydraulic head as a representation of the preconsolidation head levels in the Dickinson-La Marque area.

6. DISCUSSION

Throughout the Greater Houston area, previous historical compaction had occurred during land subsidence. This study by Jorgenson in 1975 addressed that the majority of the compaction that had occurred was within the layers of the Chicot aquifer due to the amount of clay in the subsurface. This can be seen by analyzing the Clear Lake Borehole extensometer which includes both the shallow and deep extensometer. The compaction did not just take place in one section of the Chicot Aquifer such as the shallow or middle layers but at various locations within the aquifer itself. The shallow and deep extensometer compaction curves closely follow each other throughout its site history.

The UHCC GPS array further gives an understanding of the interaction of the sediments at different levels below the ground surface. At the surface there is a subsidence rate of about 2.11 mm per year whereas between 1 to 10 feet and 0 to 20 feet below the surface there is an uplift or swell of sediments of a rate of 1.64 mm per year. This was derived by looking in relation to the UHC3 GPS unit as described in Chapter 5. This shows the swell of sections of the sediments rather than just looking at surface subsidence. To further confirm the information

provided by the GPS array and other GPS units in the surrounding area multitemporal InSAR data has been used to map ground deformation over the Greater Houston–Galveston area. Comparing the overall trend of ground deformation followed those displayed through the GPS time series analysis as well as those derived from the extensometers in the Greater Houston-Galveston area (Qu et al., 2015).

Alongside the understanding derived from the extensometers and GPS units is the acknowledgement that each hydraulic head varies with depth. Each observational well gives a specific data point for a respective spot in the subsurface, and these observational wells do not necessarily reflect the state of pressure in the entire aquifer and compaction can vary by depth (Gabrysch and Bonnet, 1975). As well, the distribution of compaction with depth is dependent on the vertical distribution of the aquitard material and the decline in pressure at a compacting layer (Holzer, 1981; Jorgenson, 1975). Due to a vertical hydraulic gradient, measurements made by a well screened at a given depth may not reflect the state of hydraulic pressure in the surrounding area of the compacting layer. This ultimately means that the values identified as corresponding to preconsolidation heads in this study may not precisely reflect the true preconsolidation stress of the compacting aquitard material. It will also account for some spatial variation in the estimate of preconsolidation head values and hydraulic head values. When looking at the spatial variation of the hydraulic and preconsolidation head levels in the Dickenson – La Marque area, it is essential to look at UHCC which includes two wells screened in the same aquifer. Specifically, the Red and Blue wells are screened in the Chicot aquifer and the Red and Blue well are 18 meters apart. When looking at these two wells the hydraulic head levels are very similar, and their general trends are the same over time. Plots of the Red and Blue well data are found in Figure 5-9. Therefore, due to the closeness of the preconsolidation

head that was derived from Holzer in the Houston Ship Channel and the considerations mentioned, preconsolidation heads levels in the region should coincide with the hydraulic head levels in the Chicot aquifer around 2000. Subsidence in the Dickenson - La Marque area can be expected to continue to slow as long as the hydraulic head level stays above the preconsolidation head.

7. CONCLUSION

This study investigated the surface deformation and its relation to groundwater withdrawal in the Dickenson - La Marque area. The results from this study are pertinent to plans for future urban development, utilization of groundwater resources, and minimization of urban geological hazards, and provides important guidelines for mitigating subsidence that is occurring in the northern and western parts of the Houston metropolitan region. The analysis of the long-period groundwater, extensometer, and GPS datasets were used to develop the following conclusions.

The regional groundwater head levels for the Chicot and Evangeline aquifer were less than 30 meters below the surface. Groundwater level changes over the past decade have increased in both the Evangeline and Chicot aquifers. From year to year the hydraulic head levels may vary due to drawdown and seasonal variability but looking on a larger time scale the general trend is increasing over the course of a decade.

Borehole extensometers and the UHCC GPS Array give insight into the compaction and inflation of the shallow aquifers. The UHCC GPS Array showed the inflation of the middle sediments between 10 and 30 feet below the surface. As well the shallow and deep Clear Lake borehole extensometer displayed similar rates of compaction leading to the conclusion that the subsidence occurred within the most part of the Chicot and uppermost part of the Evangeline

aquifer. This indicates that subsidence and compaction occurred within the aquifer itself and some inelastic compaction can continue even after groundwater levels have returned above the preconsolidation head levels as shown in the Texas City extensometer.

The general decline in the rate of groundwater withdrawal and overall compaction of sediment correlates with the implementation of the Harris-Galveston Subsidence District regulations after 1975. Initially, the Dickenson - La Marque area included rapid subsidence which coincided with the compaction rates recorded at borehole extensometer locations in the Greater Houston area. After the HGSD initiated their subsidence mitigation plan there has been an overall increase in groundwater levels and a decrease in subsidence rates. The HGSD subsidence mitigation plan called for the decrease in use of groundwater pumping and finding an alternate water source for the demand. When looking at the subsidence rates in the area after these plans were enacted, subsidence levels are now at a millimeter scale and can likely be contributed to GPS vertical error and continued geological compaction that occurs in coastal areas. Therefore, it is likely that the use of the HGSD plan was essential to the decrease in rapid subsidence in the area. Given the success of the HGSD plan in the Dickenson - La Marque area other areas with similar rapid subsidence to the north and west of Houston could benefit from similar plans. As well continued use of the subsidence mitigation plan will keep the groundwater levels above the preconsolidation head levels to keep subsidence and compaction elastic and small in magnitude. As the area's population continues to increase along with the demand for groundwater it, is essential that the local cities and utilities within the HGSD area continue to work towards finding alternative water sources to continue the mitigation of subsidence in the Dickenson - La Marque area.

BIBLIOGRAPHY

Ashworth, J. B., & Hopkins, J. (1995). Aquifers of Texas: Texas water development board report 345. *Austin, TX: Texas Water Development Board*, p. 14.

Baker, E. T. (1978). Stratigraphic and hydrogeologic framework of part of the coastal plain of Texas. *US Geological Survey Numbered Series*, No. 77-712.

Bawden, G. W., Johnson, M. R., Kasmarek, M. C., Brandt, J., & Middleton, C. S. (2012). Investigation of land subsidence in the Houston-Galveston region of Texas by using the global positioning system and interferometric synthetic aperture radar, 1993-2000 (No. 2012-521). *US Geological Survey Scientific Investigations Report 2012-5211*, p. 1-32.

Bird, D. E., Burke, K., Hall, S. A., & Casey, J. F. (2005). Gulf of Mexico tectonic history: hotspot tracks, crustal boundaries, and early salt distribution. *AAPG Bulletin*, v. 89(3), p. 311-328.

Chen, C. T., Hu, J. C., Lu, C. Y., Lee, J. C., & Chan, Y. C. (2007). Thirty-year land elevation change from subsidence to uplift following the termination of groundwater pumping and its geological implications in the metropolitan Taipei Basin, northern Taiwan. *Engineering Geology*, v. 95(1), p. 30-47.

Chowdhury, A. H., & Turco, M. J. (2006). Geology of the Gulf Coast aquifer, Texas. *Texas Water Development Board Report*, p. 365.

Coplin, L. S., & Galloway, D. (1999). Houston-Galveston, Texas. *Land subsidence in the United States: US Geological Survey Circular, 1182*, p. 35-48.

El-Rabbany, A. (2006). Introduction to GPS: The Global Positioning System, 2nd Edition. *Artech House*.

Gabrysch, R. K., & Bonnet, C. W. (1975). Land surface subsidence in the Houston-Galveston region, Texas. *Austin, TX: Texas Water Development Board Report*, p. 188.

Galloway, D. L., & Burbey, T. J. (2011). Review: regional land subsidence accompanying groundwater extraction. *Hydrogeology Journal*, *19*(8), p. 1459-1486.

Galloway, D. L., Jones, D. R., & Ingebritsen, S. E. (1999). Land subsidence in the United States: Reston Virginia, United States geological survey, 177, *US Geological Survey Circular*, 1182.

Galloway, W. E. (2008). Depositional evolution of the Gulf of Mexico sedimentary basin. *Sedimentary Basins of the World*, v. 5, p. 505-549.

GPS Data Archive Interface Version 2. DAI v2 - UNAVCO Data Archive Interface Version 2, UNAVCO, www.unavco.org/data/gps-gnss/data-access-methods/dai2/app/dai2.html.

Guier, W. H., & Weiffenbach, G. C. (1997). Genesis of satellite navigation. *Johns Hopkins APL Technical Digest*, v. 18(2), p. 179.

Holzer, T. L. (1981). Preconsolidation stress of aquifer systems in areas of induced land subsidence. *Water Resources Research*, v. 17(3), p. 693-704.

Jorgensen, D.G. (1975). Analog-model studies of groundwater hydrology in the Houston district, Texas. *Texas Water Development Board Report*, p. 190.

Kasmarek, M. C., & Ramage, J. K. (2015). Water-level altitudes 2015 and water-level changes in the Chicot, Evangeline, and Jasper aquifers and compaction 1973–2014 in the Chicot and Evangeline aquifers, Houston-Galveston Region, Texas. (No. 3337). *US Geological Survey*.

Kasmarek, M. C., & Ramage, J. K. (2012). Water-level altitudes 2012 and water-level changes in the Chicot, Evangeline, and Jasper aquifers and compaction 1973–2011 in the Chicot and Evangeline aquifers, Houston-Galveston region, Texas. US Department of Interior, *US Geological Survey Numbered Series*. No. 3230.

Kasmarek, M. C., & Robinson, J. L. (2004). Hydrogeology and simulation of ground-water flow and land-surface subsidence in the northern part of the Gulf Coast aquifer system, Texas. *US Geological Survey Numbered Series*. No. 2004-5102.

Kasmarek, M. C., and Strom, E. W. (2002). Hydrogeology and simulation of ground-water flow and land surface subsidence in the Chicot and Evangeline aquifers, Houston area, Texas: *U.S. Geological Survey, Water Resources Investigation Report* 02-4022, p. 62.

Kearns, T. J., Wang, G., Bao, Y., Jiang, J., & Lee, D. (2015). Current land subsidence and groundwater level changes in the Houston metropolitan area (2005–2012). *Journal of Surveying Engineering*, *141*(4), 05015002.

Khan, S. D., Huang, Z., & Karacay, A. (2014). Study of ground subsidence in northwest Harris County using GPS, LiDAR, and InSAR techniques. *Natural hazards*, *73*(3), p. 1143-1173.

Lee, D., Kearns, T., Yang, L., & Wang, G. (2014). Compaction of aquifer at different depths: observations from a vertical GPS array in the Coastal Center of the University of Houston, Texas. *AGU Fall Meeting Abstracts*.

Lohman, S. W. (1965). Geology and artesian water supply of the Grand Junction area, Colorado. *US Government Printing Office, No. 451*. p. 92-109

Petitt, B. M., & Winslow, A. G. (1957). Geology and ground-water resources of Galveston County, Texas. *US Government Printing Office*.

Píriz, R., Calle, D., Mozo, A., Navarro, P., Rodríguez, D., & Tobías, G. (2009, September). Orbits and clocks for GLONASS precise-point-positioning. In *Proc. ION GNSS*. 2415-2424.

Qu, F., Lu, Z., Zhang, Q., Bawden, G., Kim, J., Zhao, C., & Qu, W., (2015) Mapping ground deformation over Houston–Galveston, Texas using multi-temporal InSAR, *Remote Sensing of Environment*, 169, p. 290-306.

Rebischung, P., Griffiths, J., Ray, J., Schmid, R., Collilieux, X., & Garayt, B. (2012). IGS08: The IGS realization of ITRF2008. GPS solutions, 16(4), p.483-494.

Ryder, P. D., & Ardis, A. F. (1991). Hydrology of the Texas Gulf Coast aquifer systems. *US Geological Survey*, p. 91-64.

Sneed, M., & Galloway, D. L. (2000). Aquifer-system compaction and land subsidence: measurements, analyses, and simulations-the Holly site, Edwards Air Force Base, Antelope Valley, California (No. 2000-4015). *US Geological Survey. Water Resources Investigation Report* 00-4015.

Terzaghi, K. (1925). Principles of soil mechanics. *Engineering News-Record* 95, (19-27), p. 19-32.

NetR9 Ti-M GNSS Receiver. Trimble Monitoring Solutions, Trimble, monitoring.trimble.com/products-and-solutions/netr9-ti-m-gnss-receiver.

Wang, G., Welch, J., Kearns, T. J., Yang, L., & Serna Jr, J. (2015). Introduction to GPS geodetic infrastructure for land subsidence monitoring in Houston, Texas, USA. *Proceedings of the International Association of Hydrological Sciences*, *372*, p. 297-303.

Wang, G., Turco, M., Soler, T., Kearns, T. J., & Welch, J. (2017). Comparisons of OPUS and PPP solutions for subsidence monitoring in the greater Houston area. *Journal of Surveying Engineering*, *143*(4), 05017005.

Wang, G. (2013). Teaching high-accuracy global positioning system to undergraduates using online processing services. *Journal of Geoscience Education, 61*(2), p. 202-212.

Wang, G., & Soler, T. (2013). Using OPUS for measuring vertical displacements in Houston, Texas. *Journal of Surveying Engineering, 139*(3), p. 126-134.

Wang, G., & Soler, T. (2014). Measuring land subsidence using GPS: ellipsoid height versus orthometric height. *Journal of Surveying Engineering, 141*(2).

Wang, G., Yu, J., Kearns, T. J., & Ortega, J. (2014). Assessing the accuracy of long-term subsidence derived from borehole extensometer data using GPS observations: Case study in Houston, Texas. *Journal of Surveying Engineering, 140*(3).

Watson, D. F., and G. M. Philip. (1985). A refinement of Inverse Distance Weighted Interpolation. *Geoprocessing 2*: p. 315–327.

Yu, J., Wang, G., Kearns, T.J., & Yang, L. (2014). Is there deep-seated subsidence in the Houston-Galveston area?. *International Journal of Geophysics, 2014*, p. 1-10.

Zilkoski, D. B., Hall, L. W., Mitchell, G. J., Kammula, V., Singh, A., Chrismer, W. M., & Neighbors, R. J. (2006). The Harris-Galveston coastal subsidence district/national geodetic survey automated global positioning system subsidence monitoring project. *Proceedings of the US Geological Survey Subsidence Interest Group Conference*, p. 13-28.

Zilkoski, D. B., Hall, L. W., Mitchell, G. J., Kammula, V., Singh, A., Chrismer, W. M., & Neighbors, R. J. (2003). The Harris-Galveston coastal subsidence district/national geodetic survey automated global positioning system subsidence monitoring project. *In Proceedings of the US Geological Survey Subsidence Interest Group Conference* (pp. 13-28).

Zumberge, J. F., Heflin, M. B., Jefferson, D. C., Watkins, M. M., & Webb, F. H. (1997). Precise point positioning for the efficient and robust analysis of GPS data from large networks. *Journal of geophysical research: solid earth*, *102*(B3), p. 5005-5017.

APPENDIX I: VERTICAL COMPONENT DISPLACEMENT GPS TIME-SERIES PLOTS AND DATA TABLE

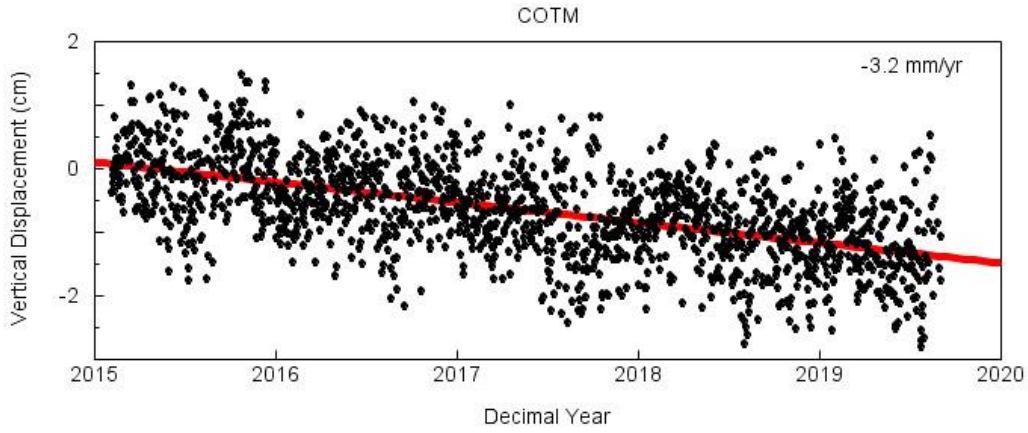

Figure A1: Vertical time series plot of GPS unit COTN. Negative values display subsidence while positive values display uplift or swell.

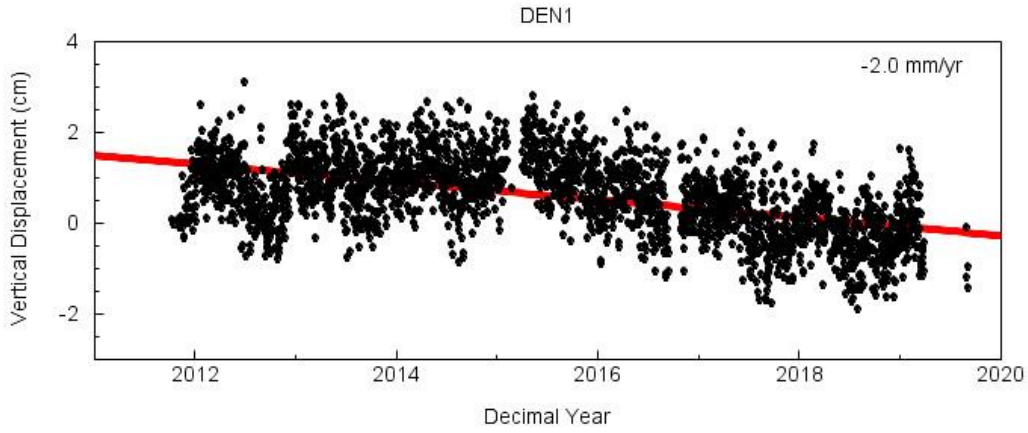

Figure A2: Vertical time series plot of GPS unit DEN1. Negative values display subsidence while positive values display uplift or swell.

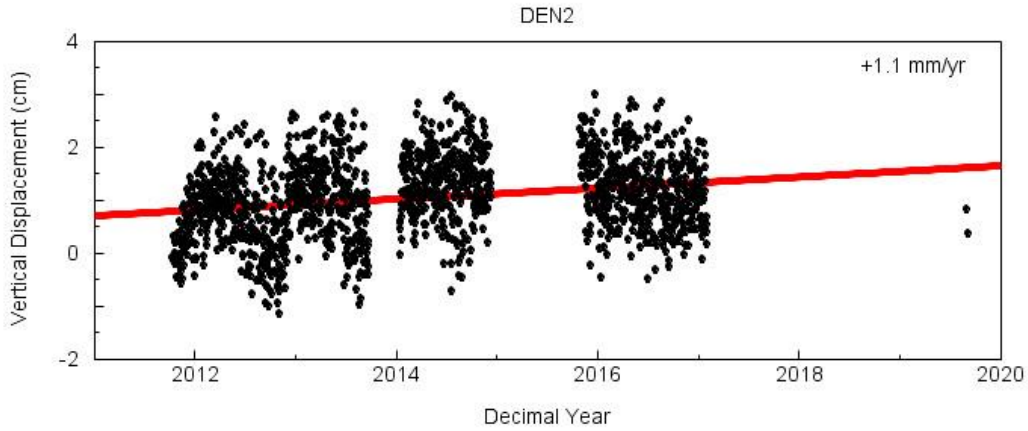

Figure A3: Vertical time series plot of GPS unit DEN2. Negative values display subsidence while positive values display uplift or swell.

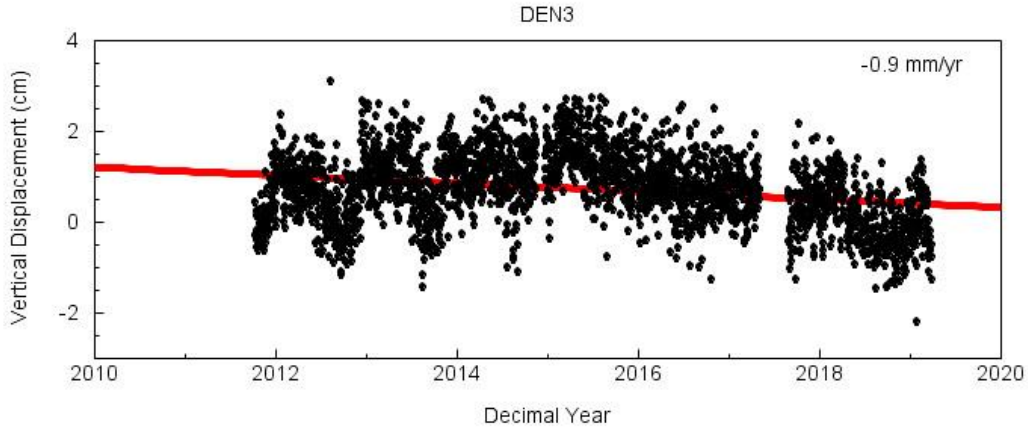

Figure A4: Vertical time series plot of GPS unit DEN3. Negative values display subsidence while positive values display uplift or swell.

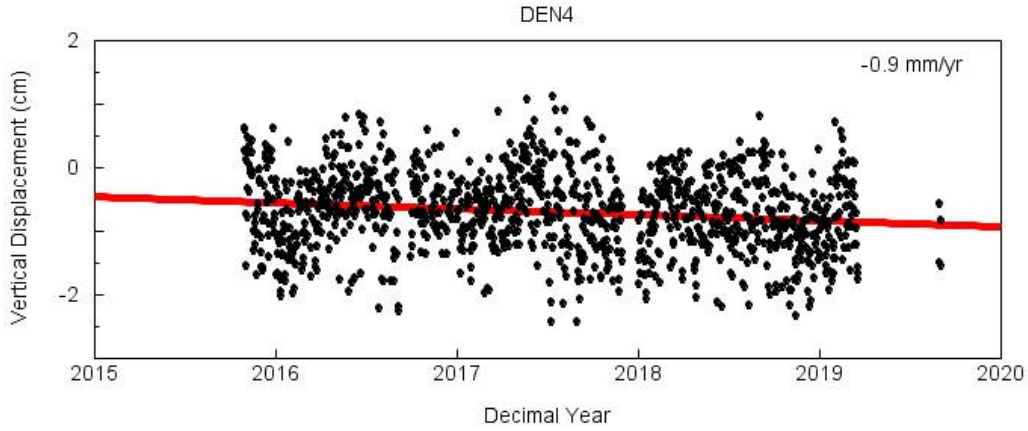

Figure A5: Vertical time series plot of GPS unit DEN4. Negative values display subsidence while positive values display uplift or swell.

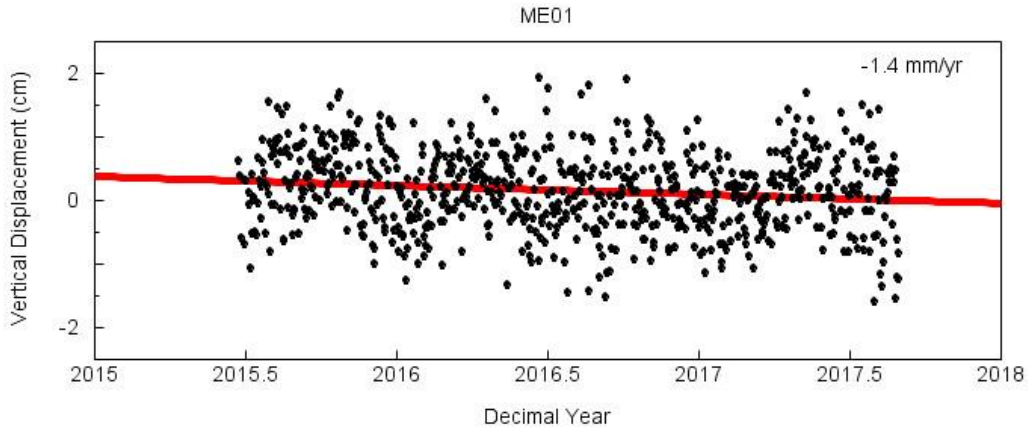

Figure A6: Vertical time series plot of GPS unit ME01. Negative values display subsidence while positive values display uplift or swell.

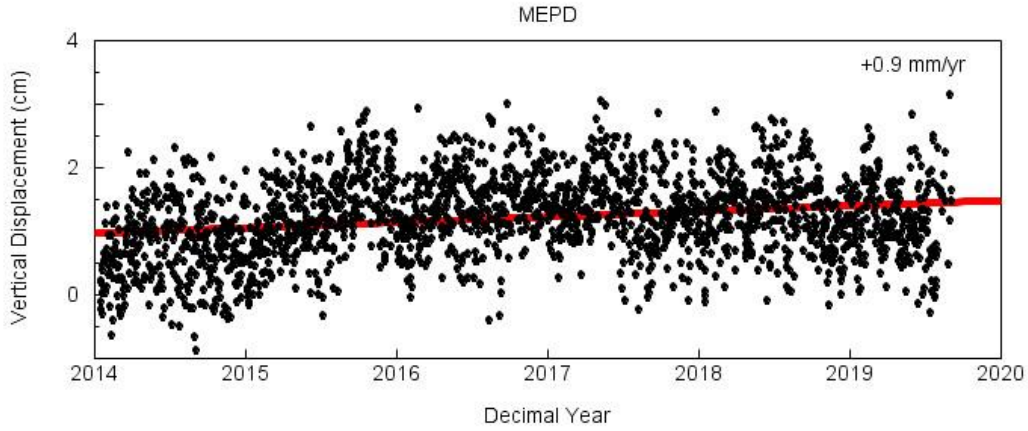

Figure A7: Vertical time series plot of GPS unit MEPD. Negative values display subsidence while positive values display uplift or swell.

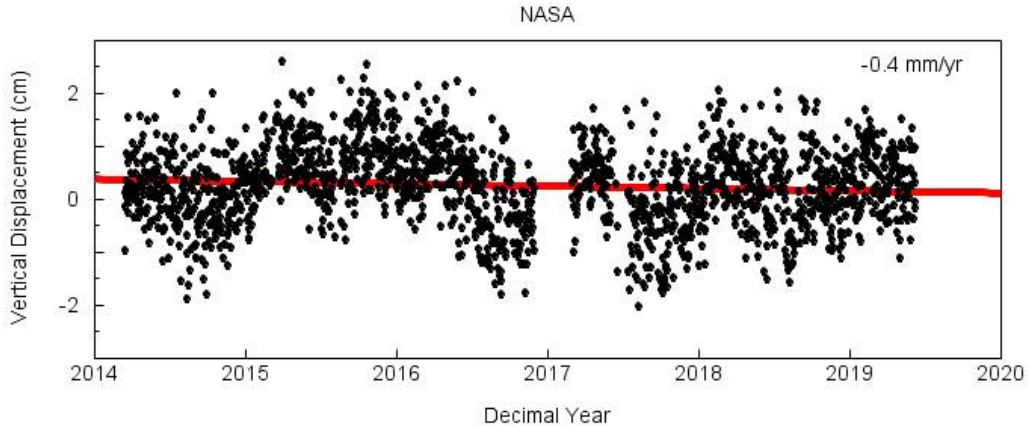

Figure A8: Vertical time series plot of GPS unit NASA. Negative values display subsidence while positive values display uplift or swell.

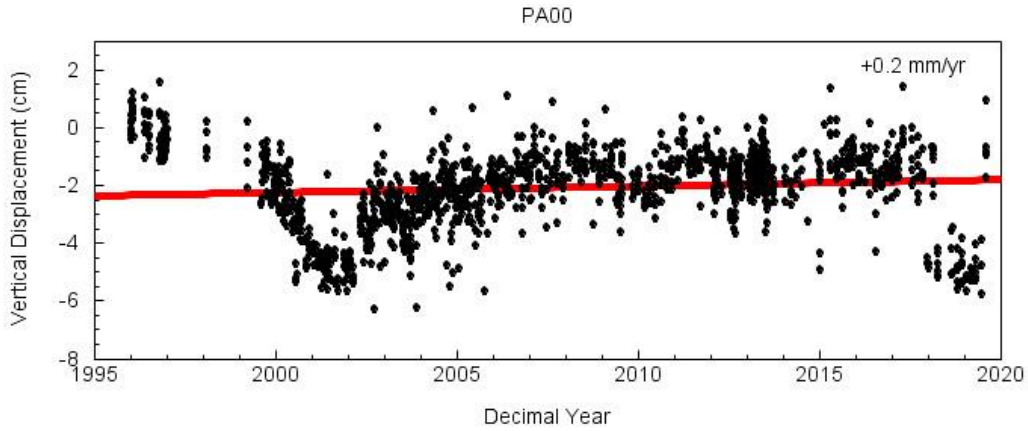

Figure A9: Vertical time series plot of GPS unit PA00. Negative values display subsidence while positive values display uplift or swell.

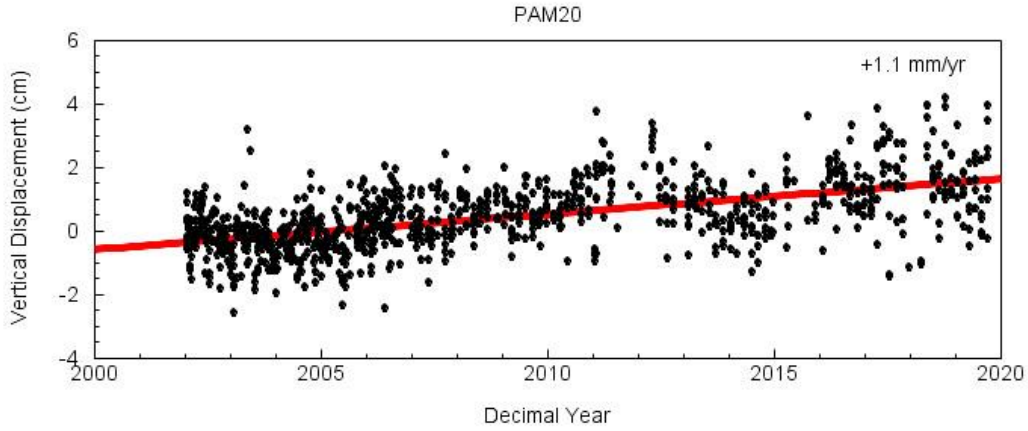

Figure A10: Vertical time series plot of GPS unit PAM20. Negative values display subsidence while positive values display uplift or swell.

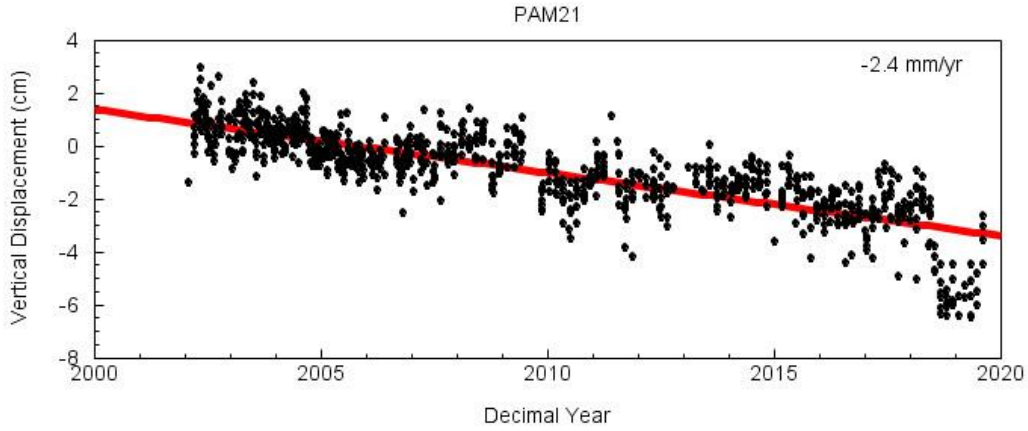

Figure A11: Vertical time series plot of GPS unit PAM21. Negative values display subsidence while positive values display uplift or swell.

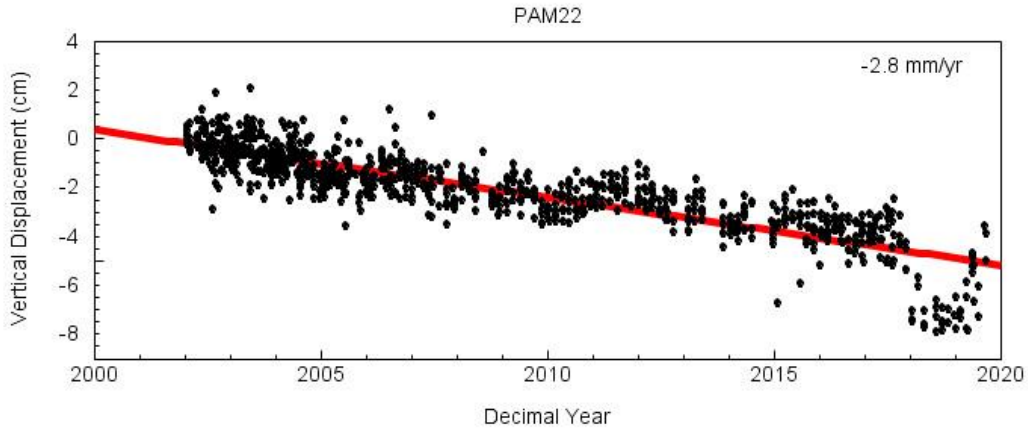

Figure A12: Vertical time series plot of GPS unit PAM22. Negative values display subsidence while positive values display uplift or swell.

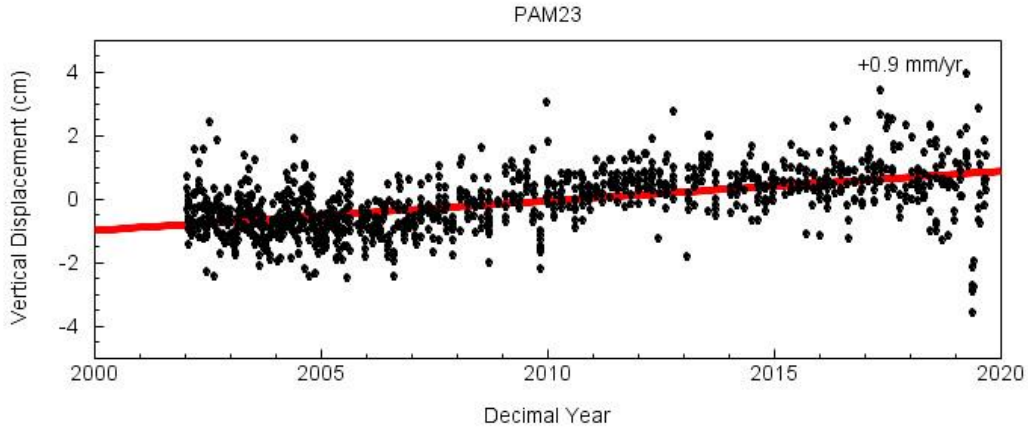

Figure A13: Vertical time series plot of GPS unit PAM23. Negative values display subsidence while positive values display uplift or swell.

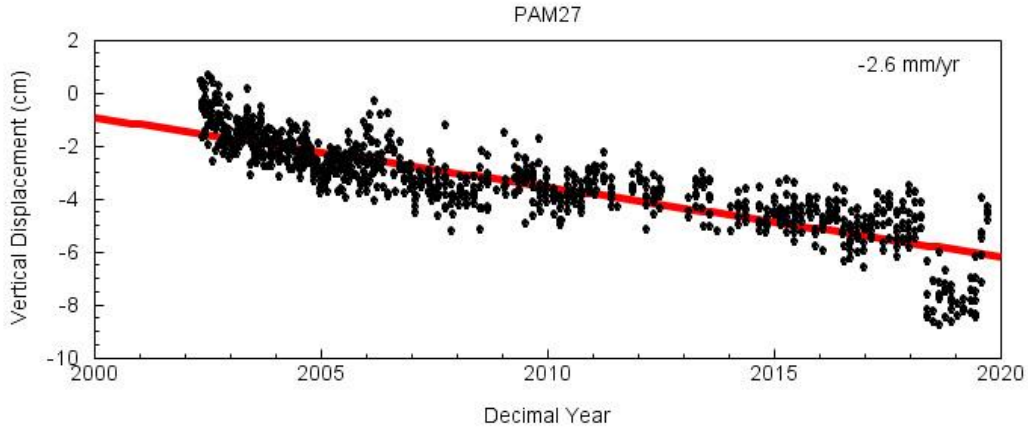

Figure A14: Vertical time series plot of GPS unit PAM27. Negative values display subsidence while positive values display uplift or swell.

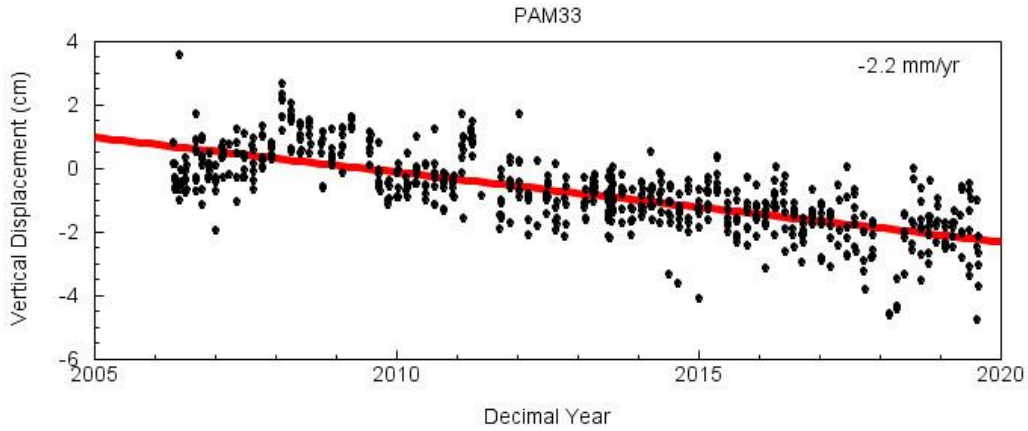

Figure A15: Vertical time series plot of GPS unit PAM33. Negative values display subsidence while positive values display uplift or swell.

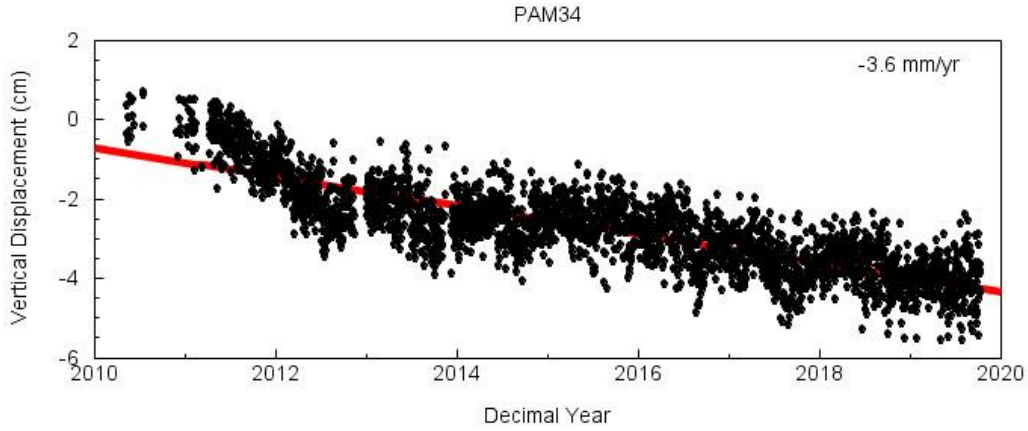

Figure A16: Vertical time series plot of GPS unit PAM34. Negative values display subsidence while positive values display uplift or swell.

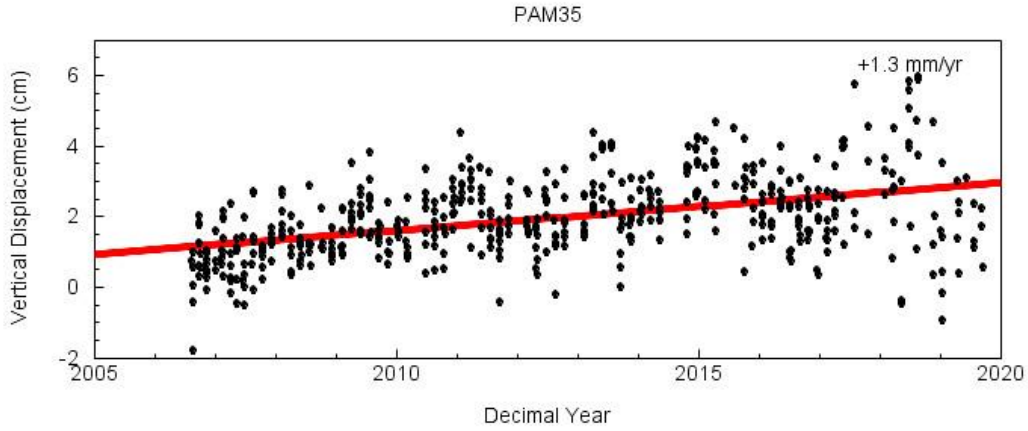

Figure A17: Vertical time series plot of GPS unit PAM35. Negative values display subsidence while positive values display uplift or swell.

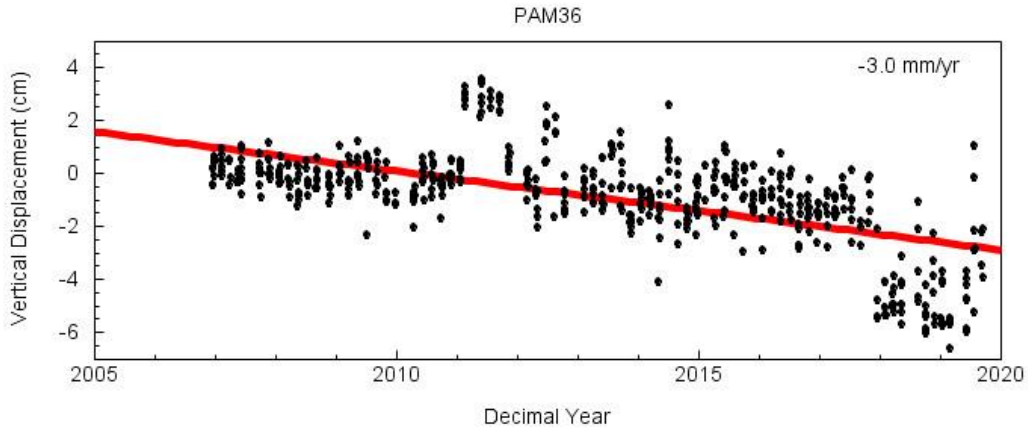

Figure A18: Vertical time series plot of GPS unit PAM36. Negative values display subsidence while positive values display uplift or swell.

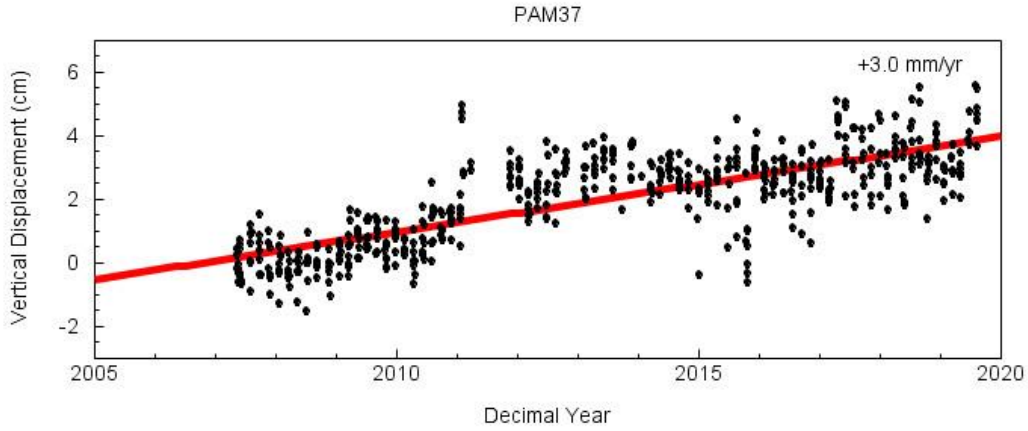

Figure A19: Vertical time series plot of GPS unit PAM37. Negative values display subsidence while positive values display uplift or swell.

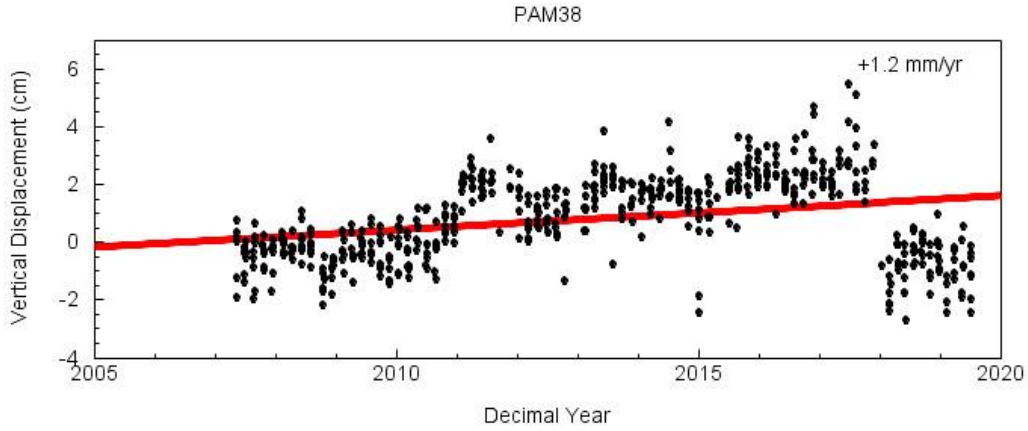

Figure A20: Vertical time series plot of GPS unit PAM38. Negative values display subsidence while positive values display uplift or swell.

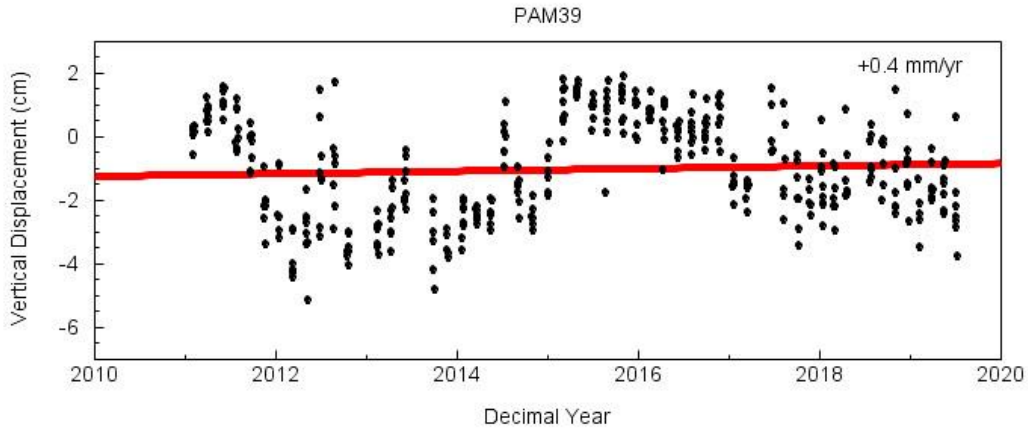

Figure A21: Vertical time series plot of GPS unit PAM39. Negative values display subsidence while positive values display uplift or swell.

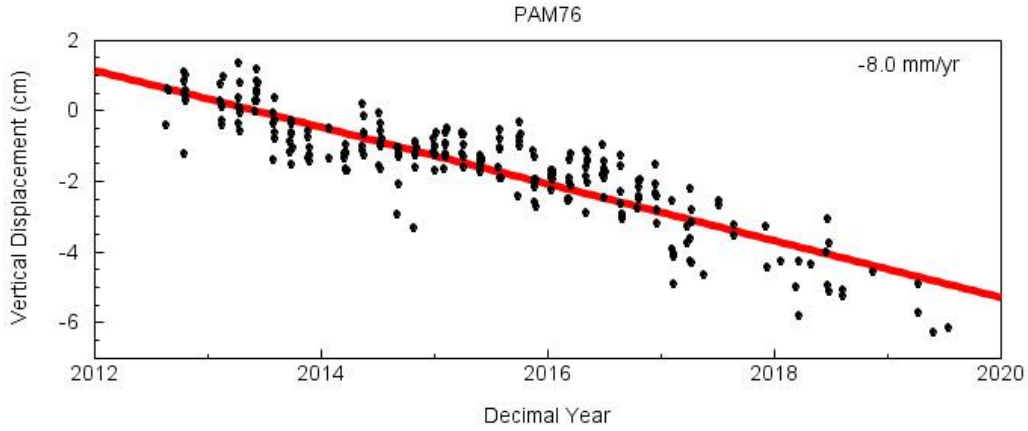

Figure A22: Vertical time series plot of GPS unit PAM76. Negative values display subsidence while positive values display uplift or swell.

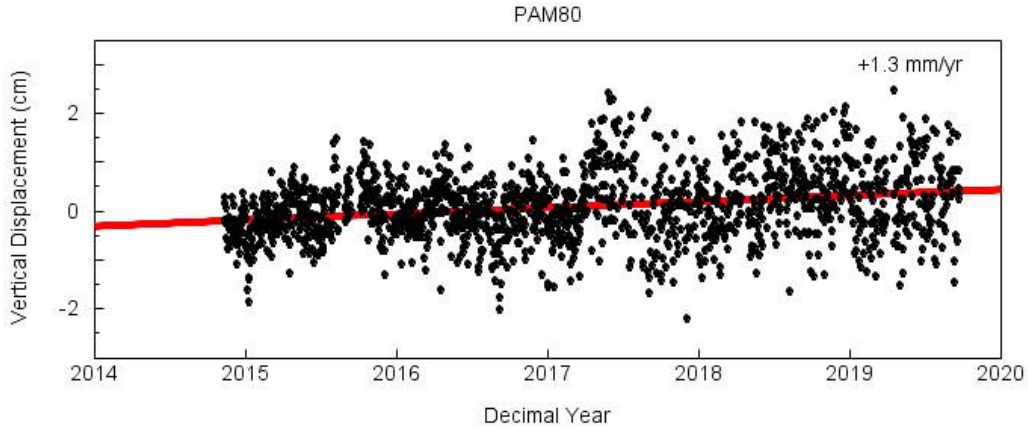

Figure A23: Vertical time series plot of GPS unit PAM80. Negative values display subsidence while positive values display uplift or swell.

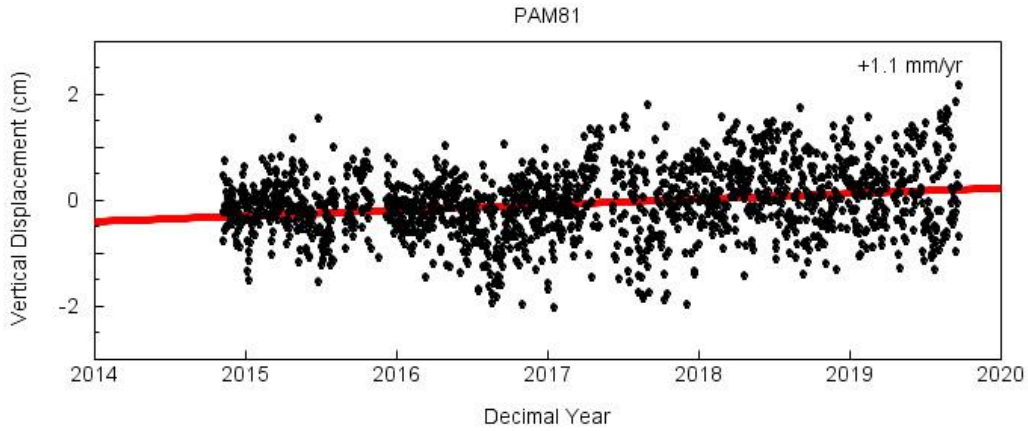

Figure A24: Vertical time series plot of GPS unit PAM81. Negative values display subsidence while positive values display uplift or swell.

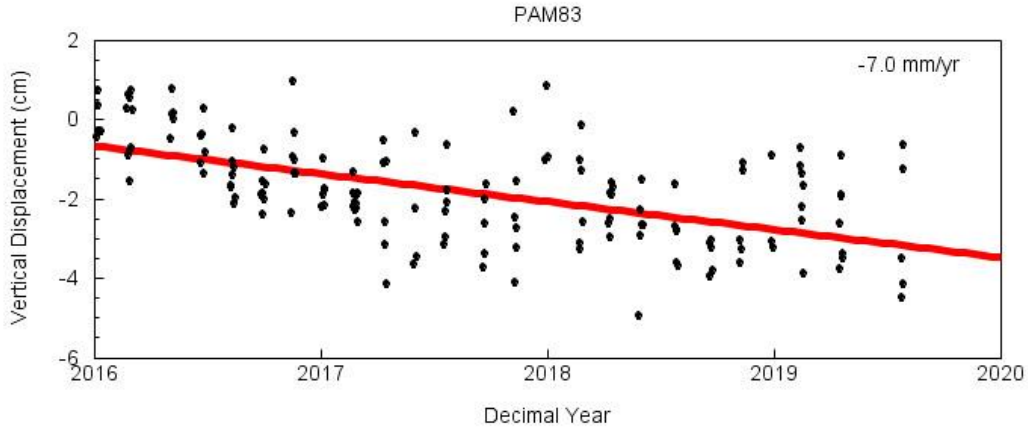

Figure A25: Vertical time series plot of GPS unit PAM83. Negative values display subsidence while positive values display uplift or swell.

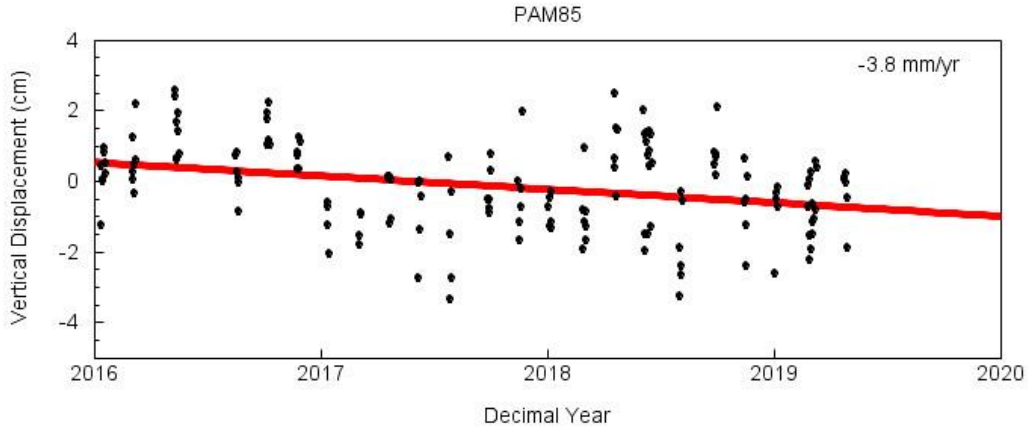

Figure A26: Vertical time series plot of GPS unit PAM85. Negative values display subsidence while positive values display uplift or swell.

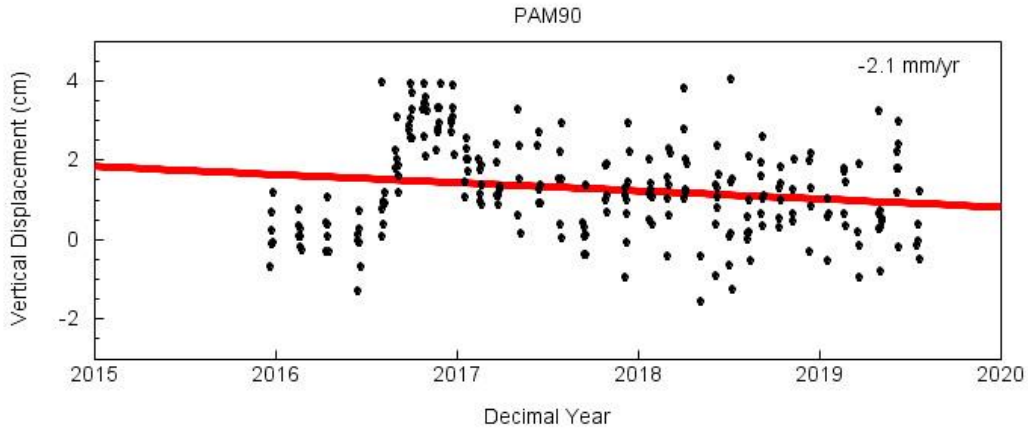

Figure A27: Vertical time series plot of GPS unit PAM90. Negative values display subsidence while positive values display uplift or swell.

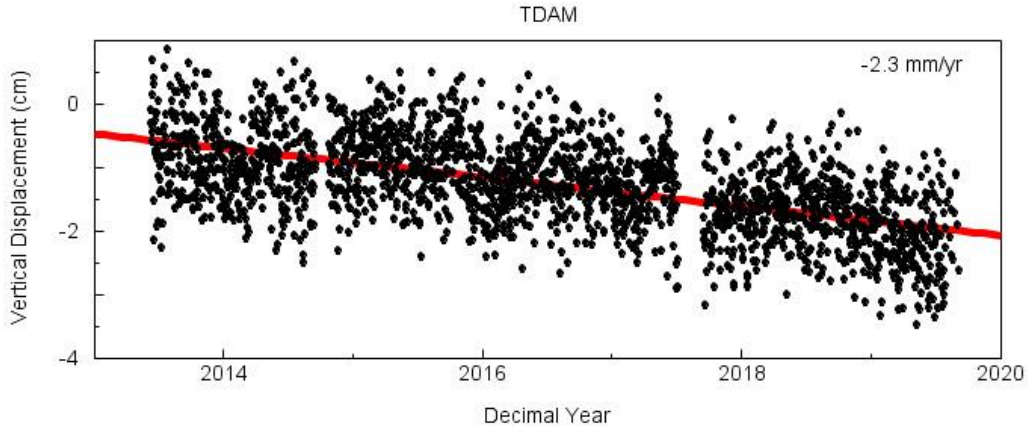

Figure A28: Vertical time series plot of GPS unit TDAM. Negative values display subsidence while positive values display uplift or swell.

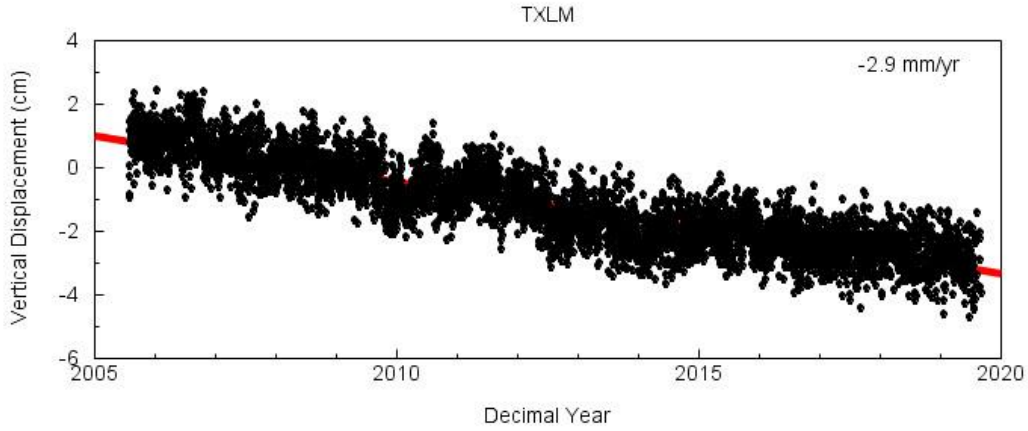

Figure A29: Vertical time series plot of GPS unit TXLM from beginning of recording to 2020. Negative values display subsidence while positive values display uplift or swell.

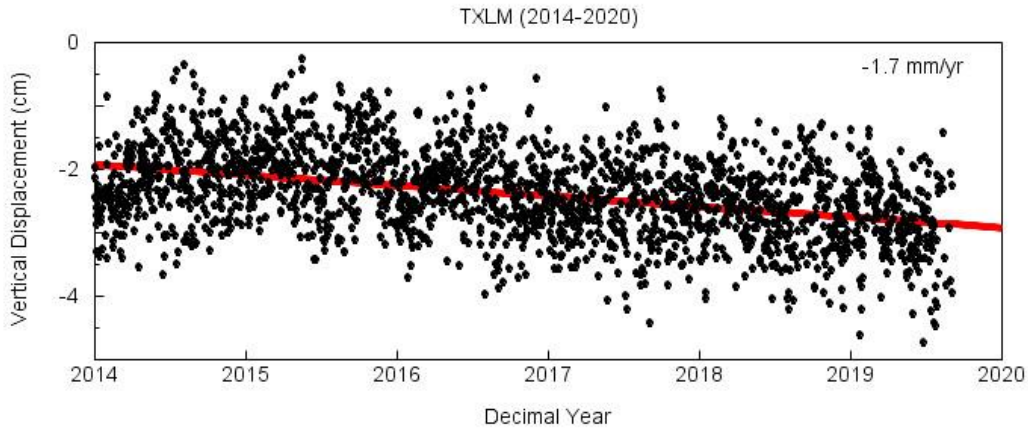

Figure A30: Vertical time series plot of GPS unit TXLM from 2014 to 2020. Negative values display subsidence while positive values display uplift or swell.

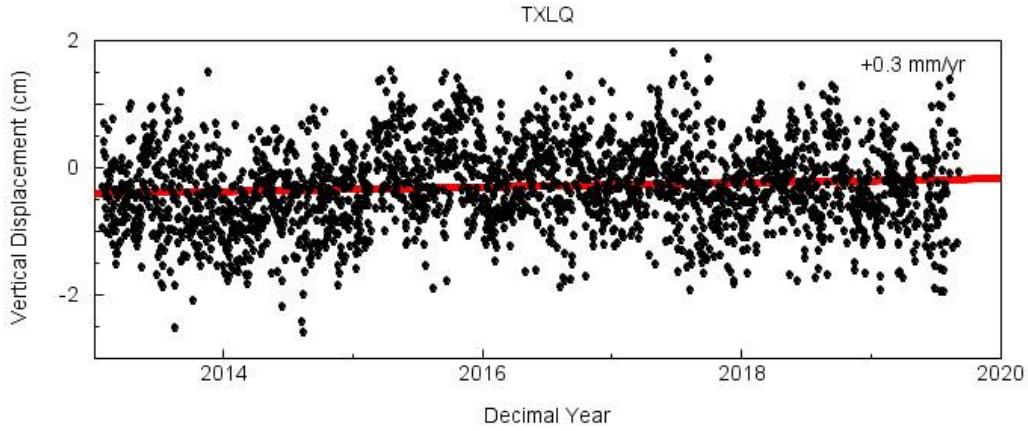

Figure A31: Vertical time series plot of GPS unit TXLQ. Negative values display subsidence while positive values display uplift or swell.

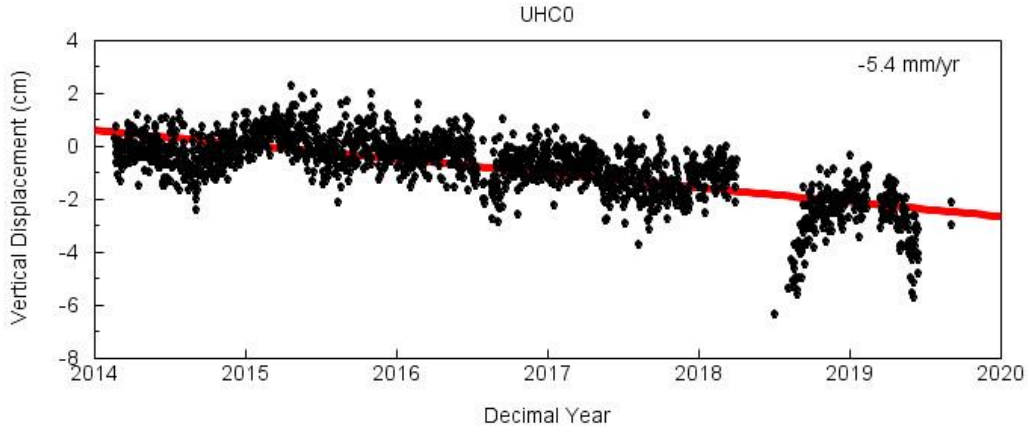

Figure A32: Vertical time series plot of GPS unit UCH0. Negative values display subsidence while positive values display uplift or swell.

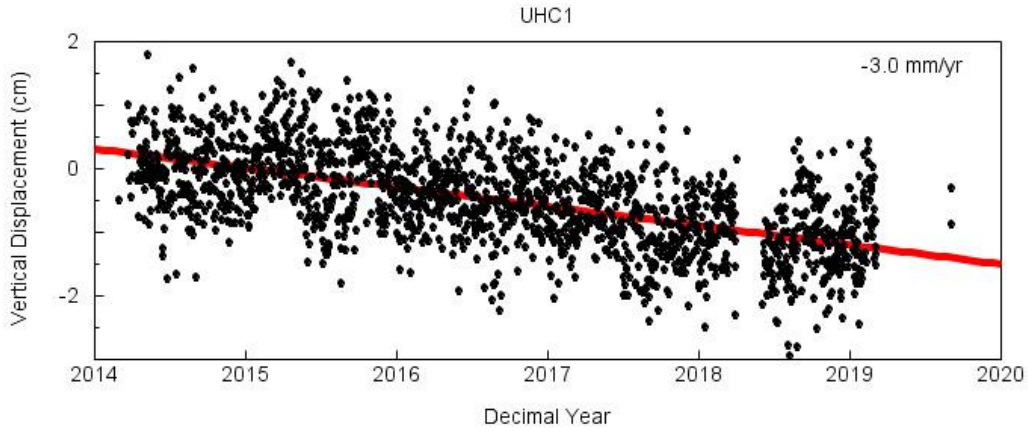

Figure A33: Vertical time series plot of GPS unit UHC1. Negative values display subsidence while positive values display uplift or swell.

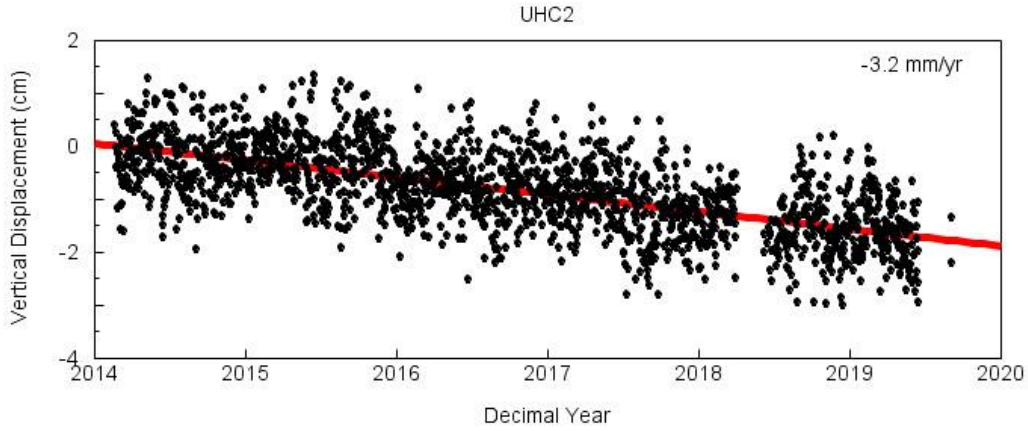

Figure A34: Vertical time series plot of GPS unit UHC2. Negative values display subsidence while positive values display uplift or swell.

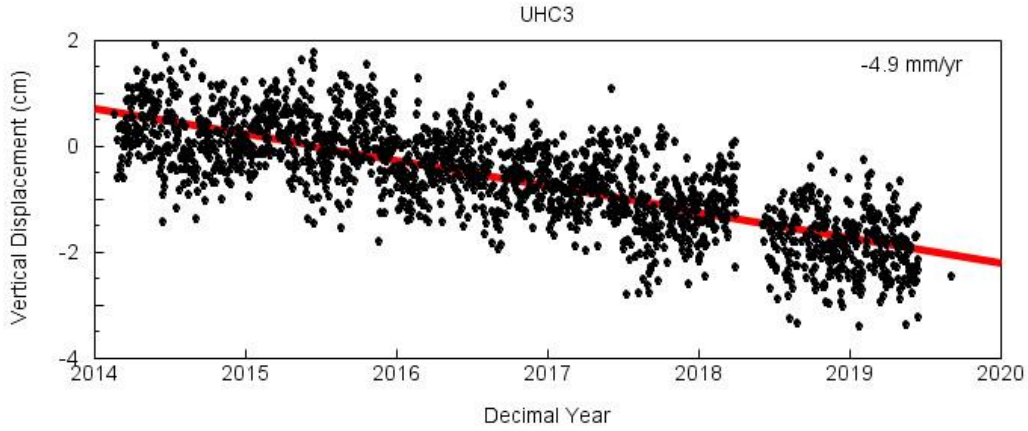

Figure A35: Vertical time series plot of GPS unit UHC3. Negative values display subsidence while positive values display uplift or swell.

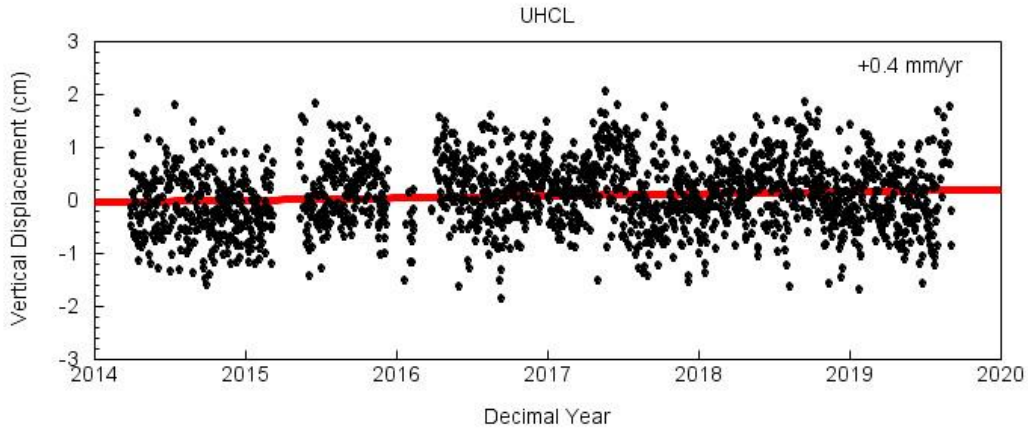

Figure A36: Vertical time series plot of GPS unit UHCL. Negative values display subsidence while positive values display uplift or swell.

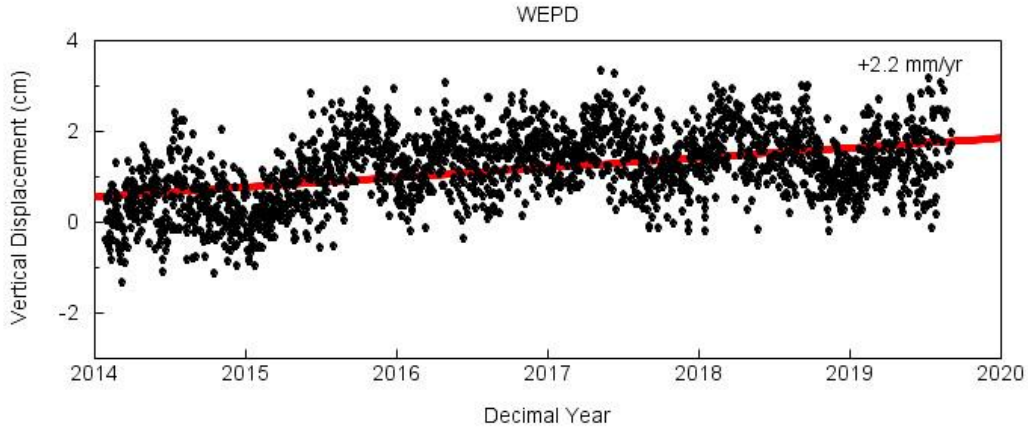

Figure A37: Vertical time series plot of GPS unit WEPD. Negative values display subsidence while positive values display uplift or swell.

Table A1 GPS Stations

GPS	Longitude (Degree)	Latitude (Degree)	History (years)	Vertical Displacement Rate (mm/yr)	Within Study Area
COTM	-94.998	29.394	5.007	-3.174	YES
PA34	-95.042	29.422	9.641	-3.631	YES
PA35	-95.082	29.473	13.356	1.349	YES
PA76	-95.045	29.361	7.188	-8.040	YES
PA93	-95.197	29.417	2.721	-16.840	YES
TXLM	-95.024	29.392	14.524	-2.875	YES
TXLQ	-94.953	29.358	7.039	0.332	YES
UHC0	-95.044	29.39	5.966	-5.428	YES

Table A1 (continued)

UHC1	-95.044	29.39	5.823	-3.024	YES
UHC2	-95.044	29.39	5.966	-3.233	YES
UHC3	-95.044	29.39	5.949	-4.885	YES
ADKS	-95.586	29.791	26.586	0.383	NO
ALEF	-95.635	29.692	5.845	-8.114	NO
ALVN	-95.278	29.401	4.778	-0.685	NO
ANG5	-95.485	29.301	16.071	-1.491	NO
ANG6	-95.485	29.302	16.09	-2.200	NO
AULT	-95.745	29.998	4.547	-10.320	NO
CFHS	-95.632	29.919	4.509	-16.209	NO
CFJV	-95.556	29.882	4.331	-11.508	NO
CMFB	-95.729	29.681	5.695	-4.781	NO
COH1	-95.543	29.67	8.701	-1.198	NO
COH2	-95.412	29.629	11.097	-0.644	NO
COH6	-95.185	30.04	6.489	-5.378	NO
CSTA	-95.512	29.796	2.177	-1.447	NO
CSTE	-95.511	29.796	4.717	-7.511	NO
DEN1	-95.258	29.51	7.838	-1.965	NO
DEN2	-95.254	29.505	7.88	1.050	NO
DEN3	-95.255	29.494	7.888	-0.881	NO
DEN4	-95.23	29.5	3.86	-0.935	NO
DEV1	-91.733	28.178	6.453	-12.558	NO
DISD	-95.74	29.289	4.624	-0.892	NO
DMFB	-95.584	29.623	5.333	-8.381	NO
DWI1	-95.404	29.014	10.705	-0.768	NO
FSFB	-95.63	29.556	5.733	-0.818	NO
GAL7	-94.737	29.33	7.488	-2.800	NO
GSEC	-95.528	30.197	4.348	-7.344	NO
HCC1	-95.561	29.788	7.19	-7.764	NO
HCC2	-95.562	29.788	6.694	-8.829	NO
HPEK	-95.716	29.755	5.708	-11.285	NO
HSMN	-95.47	29.8	6.806	-5.440	NO
JGS2	-94.891	30.045	7.641	0.461	NO
KKES	-95.595	29.85	4.405	-12.271	NO
KPCD	-95.924	29.926	3.392	-5.407	NO
KPCS	-95.924	29.926	3.253	-4.047	NO
LCI1	-95.443	29.807	7.641	-3.947	NO
LDBT	-96.779	30.089	6.511	0.403	NO
LGC1	-94.075	30.045	6.573	-1.861	NO
LKHU	-95.146	29.913	26.589	0.551	NO
MDWD	-95.595	29.771	6.801	-6.558	NO
ME01	-95.276	29.608	2.196	-1.407	NO
MEPD	-95.24	29.658	6.064	0.859	NO
MRHK	-95.745	29.804	5.708	-16.178	NO

Table A1 (continued)

NASA	-95.096	29.552	5.687	-0.436	NO
NBRY	-96.467	30.666	7.641	-0.392	NO
NETP	-95.334	29.791	26.589	0.936	NO
OKEK	-95.803	29.725	5.528	-8.841	NO
P100	-95.198	29.934	0.685	0.000	NO
P101	-95.378	28.945	0.164	0.000	NO
P102	-95.641	29.149	0.321	0.000	NO
P103	-95.311	29.151	0.014	0.000	NO
P104	-95.421	29.37	0.014	0.000	NO
P105	-95.416	29.492	0.318	0.000	NO
P106	-95.4	29.552	0.301	0.000	NO
P107	-95.459	29.157	0.323	0.000	NO
PA00	-95.152	29.539	23.745	0.222	NO
PA01	-95.617	29.912	25.778	-28.200	NO
PA02	-95.416	30.001	25.469	-26.000	NO
PA03	-95.613	29.821	25.592	-23.900	NO
PA04	-95.597	29.63	25.126	-12.200	NO
PA05	-95.586	29.791	23.207	-15.200	NO
PA06	-95.678	29.816	22.304	-26.200	NO
PA07	-95.577	29.936	20.682	-26.000	NO
PA08	-95.476	29.98	20.351	-21.600	NO
PA09	-95.071	30.038	20.575	-4.600	NO
PA10	-95.799	29.566	20.731	-3.800	NO
PA11	-95.865	30.032	20.523	-7.300	NO
PA12	-95.263	30.06	19.071	-5.536	NO
PA13	-95.49	30.195	19.033	-16.448	NO
PA14	-95.644	29.474	19.044	-5.571	NO
PA16	-95.527	29.544	18.948	-3.696	NO
PA17	-95.615	30.091	19.104	-16.964	NO
PA18	-95.678	29.965	16.909	-20.125	NO
PA19	-95.805	29.841	18.991	-9.618	NO
PA20	-95.013	29.533	17.825	1.112	NO
PA21	-95.312	29.545	17.811	-2.385	NO
PA22	-95.021	29.335	17.896	-2.761	NO
PA23	-94.918	29.335	17.88	0.932	NO
PA24	-95.041	29.669	17.742	1.868	NO
PA26	-94.938	29.21	17.8	-1.253	NO
PA27	-95.016	29.583	17.515	-2.630	NO
PA28	-94.918	29.751	17.688	0.959	NO
PA29	-95.822	29.769	12.619	-16.984	NO
PA30	-95.902	29.689	12.589	-4.341	NO
PA31	-95.848	29.398	12.474	2.233	NO
PA32	-95.707	29.541	12.375	0.103	NO
PA33	-95.224	29.49	13.578	-2.192	NO

Table A1 (continued)

PA36	-94.942	29.494	12.896	-2.980	NO
PA37	-95.101	29.631	12.515	3.002	NO
PA38	-95.223	29.649	12.564	1.187	NO
PA39	-95.339	29.645	8.83	0.407	NO
PA40	-95.463	29.493	12.548	-5.605	NO
PA41	-95.476	29.662	12.581	-6.068	NO
PA42	-95.635	29.732	12.573	-6.146	NO
PA43	-95.111	29.093	13.449	-0.393	NO
PA44	-95.687	29.88	12.622	-11.888	NO
PA45	-95.385	29.876	12.63	-3.365	NO
PA46	-95.6	30.03	12.655	-20.068	NO
PA47	-95.424	30.09	12.603	-18.355	NO
PA48	-95.672	30.045	12.669	-15.054	NO
PA49	-94.702	29.422	13.329	-3.710	NO
PA50	-94.856	29.848	12.797	-1.053	NO
PA51	-95.284	29.933	12.638	-5.127	NO
PA52	-95.177	29.852	12.638	-0.643	NO
PA53	-95.057	29.908	11.794	-1.302	NO
PA54	-95.034	29.801	13.088	-0.459	NO
PA55	-95.177	29.794	13.197	1.524	NO
PA56	-95.817	29.903	12.551	-5.994	NO
PA57	-95.722	29.684	10.649	-3.853	NO
PA58	-95.715	29.485	9.137	-1.782	NO
PA59	-95.74	29.617	9.142	-3.144	NO
PA60	-95.82	29.686	7.871	-7.360	NO
PA61	-95.972	29.675	8.83	-3.403	NO
PA62	-95.974	29.593	8.83	-5.001	NO
PA63	-95.547	29.508	8.471	-2.738	NO
PA65	-95.107	30.106	7.489	-8.936	NO
PA66	-95.767	30.017	8.679	-15.966	NO
PA67	-95.855	29.532	8.605	-4.917	NO
PA68	-95.587	30.185	7.551	-11.567	NO
PA69	-95.459	30.199	8.12	-12.715	NO
PA70	-95.424	30.291	8.236	-5.712	NO
PA71	-95.579	30.353	8.121	-6.644	NO
PA72	-95.242	30.147	7.953	-0.552	NO
PA73	-95.73	30.193	7.871	-9.471	NO
PA74	-95.231	29.736	7.874	1.168	NO
PA75	-95.031	29.758	7.426	-2.585	NO
PA77	-95.85	29.979	6.668	-8.695	NO
PA78	-96.016	29.739	5.627	-6.482	NO
PA79	-95.471	29.035	4.597	0.862	NO
PA80	-95.165	29.578	5.134	1.251	NO
PA81	-95.17	29.556	5.142	1.055	NO

Table A1 (continued)

PA82	-95.731	29.296	3.428	-7.054	NO
PA83	-95.182	29.262	3.882	-7.016	NO
PA84	-95.37	29.297	3.715	-1.908	NO
PA85	-95.278	29.343	3.869	-3.806	NO
PA86	-95.458	29.258	3.427	-7.692	NO
PA87	-95.677	29.058	3.85	-6.115	NO
PA88	-95.438	29.446	3.715	-6.598	NO
PA89	-95.799	29.566	4.23	-5.332	NO
PA90	-95.16	29.71	3.926	-2.053	NO
PA91	-95.493	29.783	3.404	-10.868	NO
PA92	-95.501	29.881	3.409	-4.975	NO
PA94	-95.524	29.722	2.622	-3.973	NO
PA95	-95.294	29.808	2.701	2.265	NO
PA96	-95.748	29.724	2.37	3.888	NO
PA97	-95.847	29.785	1.836	-23.860	NO
PA98	-95.82	29.803	1.819	-21.390	NO
PA99	-95.579	29.986	1.819	0.817	NO
PWES	-95.511	30.199	4.881	-7.752	NO
RDCT	-95.495	29.81	6.543	-5.871	NO
ROD1	-95.527	30.072	13.101	-11.364	NO
RPFB	-95.514	29.484	5.331	-1.916	NO
SESG	-95.43	29.987	5.426	-8.773	NO
SHSG	-95.43	30.054	5.383	-10.774	NO
SISD	-96.174	29.762	4.928	-4.029	NO
SPBH	-95.515	29.802	6.801	-6.362	NO
TDAM	-94.817	29.314	6.669	-2.275	NO
THSU	-95.34	29.714	7.149	0.464	NO
TMCC	-95.395	29.702	16.718	3.376	NO
TSFT	-95.48	29.806	6.724	-4.938	NO
TXAC	-94.671	29.778	8.98	-0.157	NO
TXAG	-95.419	29.164	14.524	-0.453	NO
TXAV	-95.242	29.403	2.957	-3.441	NO
TXB6	-94.937	29.757	5.771	-0.968	NO
TXBC	-95.972	29	10.699	-1.871	NO
TXBH	-95.946	29.786	2.954	-5.308	NO
TXBM	-94.18	30.162	17.566	-2.700	NO
TXBX	-96.397	30.718	6.913	8.018	NO
TXBY	-96.371	30.686	7.283	-0.600	NO
TXCM	-96.577	29.703	9.667	-1.875	NO
TXCN	-95.441	30.349	14.48	-11.885	NO
TXCV	-95.094	30.335	7.439	-4.986	NO
TXCY	-95.626	30.096	2.713	-12.560	NO
TXDY	-94.893	30.031	0.799	-1.141	NO
TXED	-96.634	28.968	10.201	-0.337	NO

Table A1 (continued)

TXEX	-95.119	29.564	9.115	1.448	NO
TXEX	-95.119	29.564	8.726	-1.459	NO
TXGA	-94.773	29.328	14.524	-1.300	NO
TXGV	-94.789	29.285	4.414	1.000	NO
TXH2	-94.391	29.563	4.014	-1.806	NO
TXHE	-96.063	30.099	14.524	-5.780	NO
TXHN	-95.596	30.742	8.86	-0.217	NO
TXHS	-95.556	29.716	7.573	-6.288	NO
TXHU	-95.433	29.779	11.828	-3.100	NO
TXHV	-95.553	30.721	4.641	1.088	NO
TXKO	-94.332	30.395	8.334	0.387	NO
TXKY	-95.829	29.822	4.775	-9.316	NO
TXLG	-96.848	29.917	8.567	-1.710	NO
TXLI	-94.771	30.056	14.524	0.898	NO
TXMG	-95.964	28.983	6.795	-2.425	NO
TXNV	-96.067	30.382	7.641	-3.651	NO
TXPS	-99.082	28.889	12.32	-1.846	NO
TXPV	-96.619	28.638	9.812	0.197	NO
TXRN	-95.829	29.543	4.898	-2.722	NO
TXRO	-95.807	29.519	5.859	-14.400	NO
TXRS	-95.805	29.519	8.657	-2.320	NO
TXTG	-95.297	29.898	4.638	-4.081	NO
TXVA	-96.91	28.835	15.003	-0.835	NO
TXVC	-96.958	28.834	4.794	-0.098	NO
TXWH	-96.112	29.325	9.678	-3.974	NO
TXWI	-94.371	29.806	4.619	-4.711	NO
TXWN	-96.092	29.329	5.101	-1.349	NO
UH01	-95.345	29.722	7.332	-0.910	NO
UH02	-95.457	30.315	5.09	-6.075	NO
UHCL	-95.104	29.578	5.862	0.403	NO
UHCR	-95.757	29.728	5.725	-9.006	NO
UHDT	-95.359	29.766	6.541	-1.616	NO
UHEB	-96.066	29.526	5.509	-1.935	NO
UHEP	-95.327	29.719	5.739	-1.466	NO
UHF1	-95.483	30.236	5.714	-5.289	NO
UHJF	-95.483	30.236	5.706	-3.174	NO
UHKD	-95.748	29.724	0.882	-14.977	NO
UHKS	-95.748	29.724	1.44	5.636	NO
UHL1	-94.978	30.058	5.747	1.949	NO
UHRI	-95.403	29.719	5.774	-2.866	NO
UHSL	-95.652	29.575	5.917	-2.815	NO
UHWL	-94.978	30.058	5.659	-0.800	NO
UTEX	-95.568	29.786	7.584	-7.357	NO
WCHT	-95.581	29.783	6.809	-10.742	NO

Table A1 (continued)

WDVW	-95.533	29.79	6.784	-6.354	NO
WEPD	-95.229	29.688	6.029	2.168	NO
WHCR	-95.505	30.194	5.325	-5.259	NO
ZHU1	-95.331	29.962	17.062	-7.742	NO

APPENDIX II: GROUNDWATER DATA TABLE

Table A2: Chicot Aquifer Data

ID	Depth to Water Year 2000 (m)	Depth to Water Year 2005 (m)	Depth to Water Year 2010 (m)	Depth to Water Year 2015 (m)	Depth to Water Year 2019 (m)	Within Study Area
KH-64-33-103		-21.671	-21.831		-21.446	YES
KH-64-33-109		-23.104	-21.991		-21.298	YES
KH-65-48-204	-22.199	-20.519	-20.275	-21.251	-21.833	YES
KH-65-40-704	-31.035	-28.310	-26.950	-27.322	-27.904	YES
KH-65-40-802	-35.003	-27.720	-27.469	-27.895	-28.276	YES
KH-65-40-707		-28.211	-27.743	-28.295	-27.823	YES
BH-81-06-301				-13.914	0.000	NO
LJ-60-61-601	-20.309	-19.754	-20.138		-20.278	NO
LJ-60-60-712		-40.654	-45.333		-43.727	NO
BH-81-06-214	-12.369	-14.963	-13.780	-12.366	-9.869	NO
LJ-65-24-115		-52.426	-44.806	-50.292	-54.864	NO
BH-81-04-202	-15.630	-14.661	-14.963	-15.298	-16.349	NO
BH-81-06-406	-11.238	-16.599	-9.866	-9.318	-8.786	NO
BH-81-06-607				-12.997	-12.800	NO
BH-81-06-408	-10.967	-16.103	-9.885	-8.818	-8.306	NO
BH-65-61-607				-12.009	-7.291	NO
BH-65-61-923				-12.701	-8.644	NO
BH-65-59-813				-12.043	-9.857	NO
BH-65-59-810				-10.720	-8.629	NO
BH-65-59-501	-3.319	-2.225	-2.707	-2.822	-2.344	NO
BH-65-53-513	-20.010	-19.477		-20.278	-22.689	NO
BH-65-47-401	-23.150	-21.860		-22.799	-22.939	NO
BH-65-46-702	-13.350	-14.204		-13.237	-3.856	NO
BH-65-55-205				-17.395	-17.662	NO
LJ-65-24-211		-37.490	-34.290		-32.961	NO
LJ-65-24-501	-39.170	-36.238	-34.462		-33.859	NO
LJ-65-11-809					-50.173	NO
KH-64-41-312	-15.115	-15.938	-13.554	-15.286	-11.893	NO
BH-65-39-705				-39.450	-38.271	NO

Table A2 (continued)

KH-64-33-802	-13.356	-12.245	-11.541	-11.390	-11.322	NO
KH-64-33-807	-16.987	-15.805	-15.242	-15.264	-14.745	NO
KH-64-33-501	-13.417	-12.474	-12.596	-10.500	-6.858	NO
LJ-65-13-221	-82.636	-86.301	-64.352	-62.197	-60.207	NO
KH-64-33-110			-24.699		-21.933	NO
KH-64-33-101		-22.647	-22.886		-23.948	NO
LJ-65-24-202		-37.186	-27.280		-34.499	NO
KH-65-32-902	-35.610	-31.349	-30.151		-28.666	NO
BH-65-30-604	-55.169	-54.870	-56.351	-51.883	-51.155	NO
BH-65-30-902	-51.328	-44.955	-42.715	-35.982	-32.437	NO
BH-65-30-615		-50.201	-50.661	-46.296	-46.640	NO
BH-65-30-731				-39.636	-42.687	NO
KH-65-32-713		-33.421	-32.233	-32.644	-31.853	NO
LJ-60-60-103	-33.982	-39.368	-46.345	-38.310		NO
BH-65-50-504	-15.033	-13.454		-15.386		NO
KH-65-39-310		-37.204	-35.239	-35.503	-35.131	NO
LJ-65-32-739		-38.435	-36.085	-35.768	-35.076	NO
LJ-60-62-716		-36.128	-32.783		-33.534	NO
LJ-65-32-407	-40.203	-35.515	-34.052	-34.147	-33.424	NO
LJ-65-32-430		-37.128	-36.795	-29.316	-29.944	NO
LJ-65-19-201	-41.215	-44.940			-43.599	NO
LJ-60-59-405			-38.667	-40.459	-39.472	NO
LJ-65-08-103		-34.324	-34.927		-34.317	NO
LJ-65-07-601		-50.703	-43.282		-40.413	NO
LJ-65-32-422	-37.216	-35.049	-31.361	-31.477	-30.590	NO
LJ-65-21-150	-93.497	-79.045	-60.701	-56.237	-58.701	NO
LJ-65-32-410	-42.142	-37.862	-36.027	-35.762	-34.330	NO
LJ-65-32-519	-38.326	-33.824	-32.239	-32.214	-31.419	NO
LJ-64-09-505		-27.289	-25.978		-30.693	NO
LJ-65-16-602		-33.440	-30.879			NO
LJ-65-24-902	-37.454	-33.683	-31.911		-29.346	NO
LJ-65-15-920		-36.567	-34.459		-34.698	NO
LJ-65-16-814		-35.366	-30.318		-28.986	NO
LJ-65-12-801	-63.728	-54.727	-53.627		-50.774	NO
LJ-65-24-209	-38.094	-34.637	-33.040		-33.540	NO
LJ-65-24-216	-5.080	-3.922	-3.849	-3.880	-3.687	NO
LJ-65-24-215		-30.207	-28.815	-28.975	-6.386	NO
LJ-65-20-814				-72.135	-64.474	NO
LJ-65-23-220			-35.966			NO
LJ-65-24-811		-35.339	-33.409		-32.915	NO
LJ-65-32-426	-32.591	-34.908	-33.037	-31.664	-27.062	NO

Table A2 (continued)

LJ-65-32-628	-5.531	-5.123	-5.094	-5.015	-3.547	NO
LJ-65-32-629	-22.584	-21.273	-20.091	-20.091	-19.525	NO
KH-64-33-921	-3.535	-3.593	-3.305	-3.224	-3.436	NO
KH-64-33-920	-15.927	-14.630	-14.021	-14.298	-14.088	NO
KH-64-33-918	-15.728	-14.757	-14.021	-13.750	-13.273	NO
KH-64-33-917	-11.506	-10.521	-9.441	-9.992	-9.656	NO
KH-64-33-916		-9.954	-9.380	-9.113	-8.800	NO
KH-64-33-915	-7.670	-7.235	-6.759	-6.441	-6.181	NO
LJ-65-16-923	-25.387	-23.728	-22.827	-22.923	-22.212	NO
LJ-65-16-922	-6.804	-6.443	-6.396	-6.416	-6.139	NO
LJ-65-16-925	-33.571	-30.892	-29.603	-30.185	-29.284	NO
LJ-65-16-930	-35.555	-32.543	-31.122	-31.593	-30.747	NO
LJ-65-16-933	-4.306	-3.405	-3.085	-3.189	-2.512	NO
LJ-65-21-229	-75.426	-66.962	-67.297	-56.962	-68.335	NO
LJ-65-21-228	-53.364	-50.918	-50.003	-47.330	-47.919	NO
LJ-65-14-745	-45.844	-43.488	-42.808	-41.114	-40.932	NO
LJ-65-23-320	-43.019	-39.088	-37.857	-37.356	-36.617	NO
LJ-65-07-902	-28.113	-26.054	-25.118	-25.735	-24.492	NO
LJ-65-14-738	-65.420	-56.944	-54.998	-52.008	-52.670	NO
LJ-65-12-729	-51.164	-51.200	-50.806	-48.057	-46.845	NO
LJ-65-12-725	-5.451	-3.848	-3.571	-3.682	-3.735	NO

Table A3: Evangeline Aquifer Data

ID	Depth to Water Year 2000 (m)	Depth to Water Year 2005 (m)	Depth to Water Year 2010 (m)	Depth to Water Year 2015 (m)	Depth to Water Year 2019 (m)
BH-65-38-609	-51.554	-51.398	-47.025	-45.144	-47.025
LJ-65-32-401	-38.787	-34.752	-33.093	-33.494	-32.327
LJ-65-32-425	-41.085	-37.928	-36.855	-36.738	-0.917
LJ-65-32-427	-41.158	-38.017	-36.959	-36.861	-35.976
LJ-65-32-424	-46.099	-43.237	-42.240	-41.605	-29.441
LJ-65-32-625	-34.086	-31.028	-29.793	-29.717	-28.965
LJ-65-32-626	-34.029	-31.285	-29.771	-29.654	-28.840
LJ-65-32-627	-33.116	-30.821	-28.968	-29.053	-28.273
LJ-65-32-630	-33.963	-29.577	-28.882	-29.610	-28.776
KH-64-33-919	-16.358	-14.984	-14.396	-14.649	-14.365
LJ-65-32-428	-38.202	-36.785	-36.255	-40.141	-40.209

APPENDIX III: CHANGE IN HYDRAULIC HEAD LEVELS

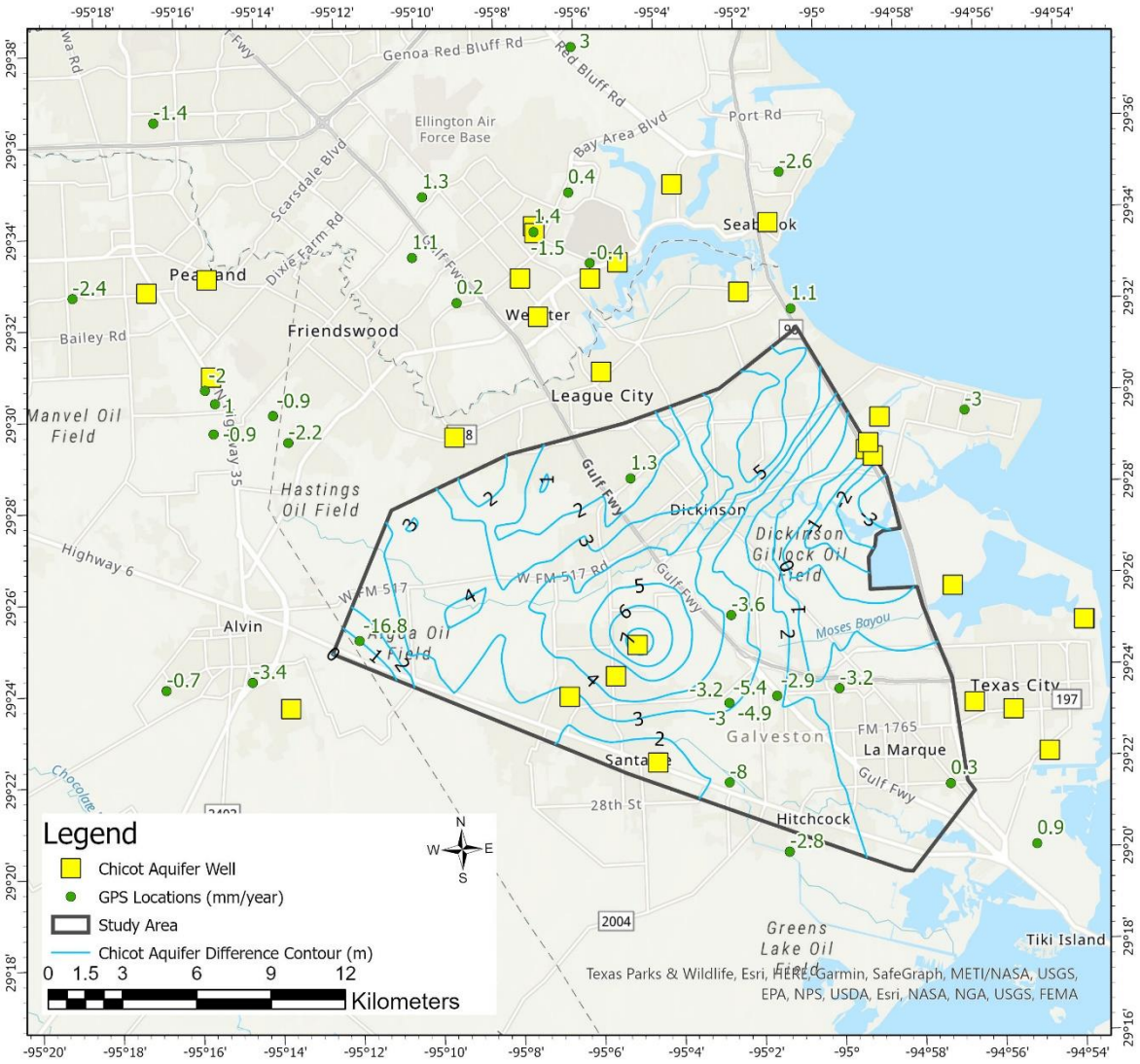

Figure A38: Change in hydraulic head levels of the Chicot Aquifer between the years of 2010 and 2000 derived by finding the difference between the hydraulic head levels of 2010 and 2000. Contours show the change in groundwater levels in the aquifer overlain on the current vertical GPS ground deformation trends. Aquifer contours display negative values representing a decrease in hydraulic head levels. Positive values represent an increase in hydraulic head levels. GPS negative values display subsidence while positive values display uplift or swell.

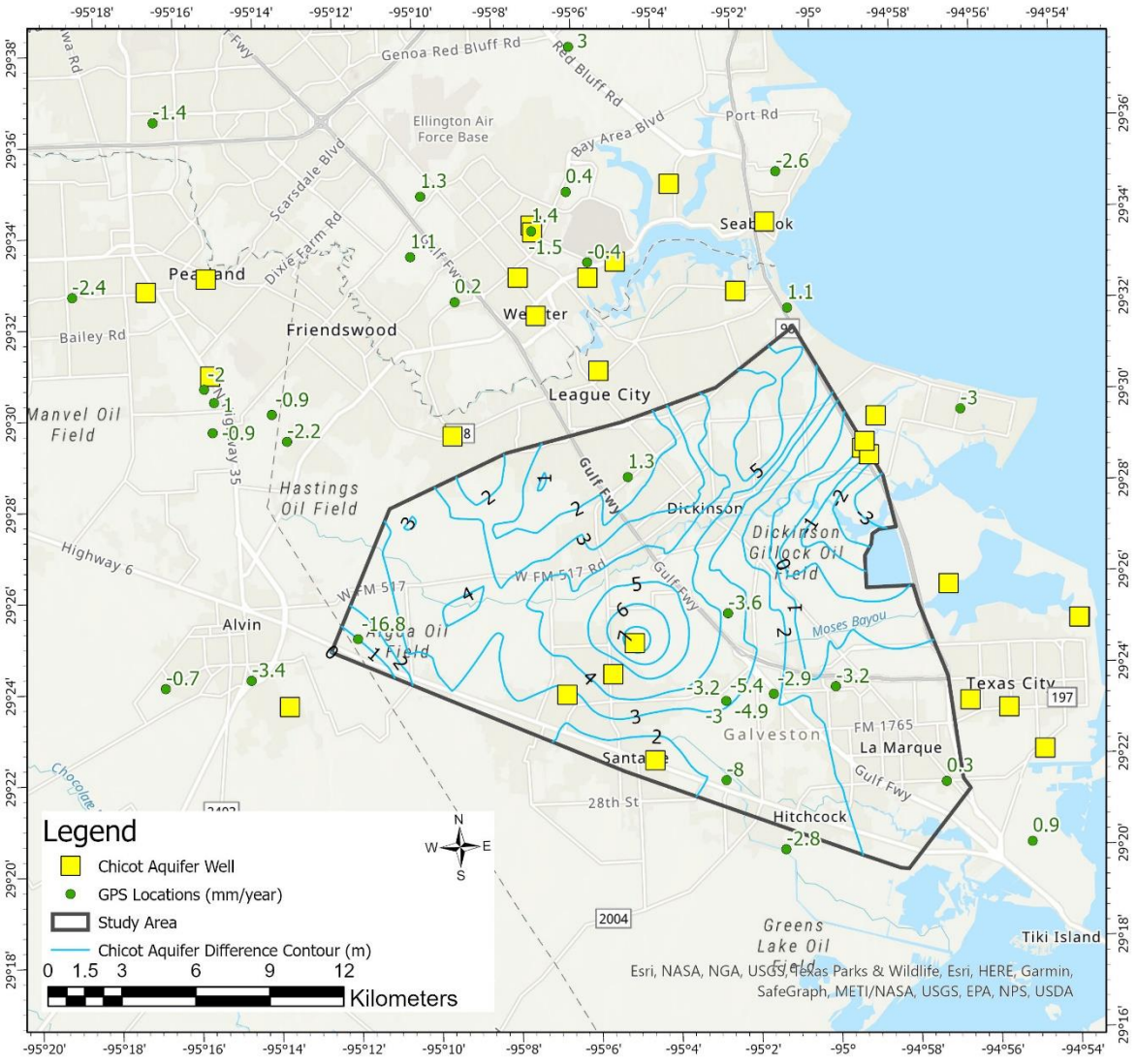

Figure A39: Change in hydraulic head levels of the Chicot Aquifer between the years of 2019 and 2010 derived by finding the difference between the hydraulic head levels of 2019 and 2010. Contours show the change in groundwater levels in the aquifer overlain on the current vertical GPS ground deformation trends. Aquifer contours display negative values representing a decrease in hydraulic head levels. Positive values represent an increase in hydraulic head levels. GPS negative values display subsidence while positive values display uplift or swell.

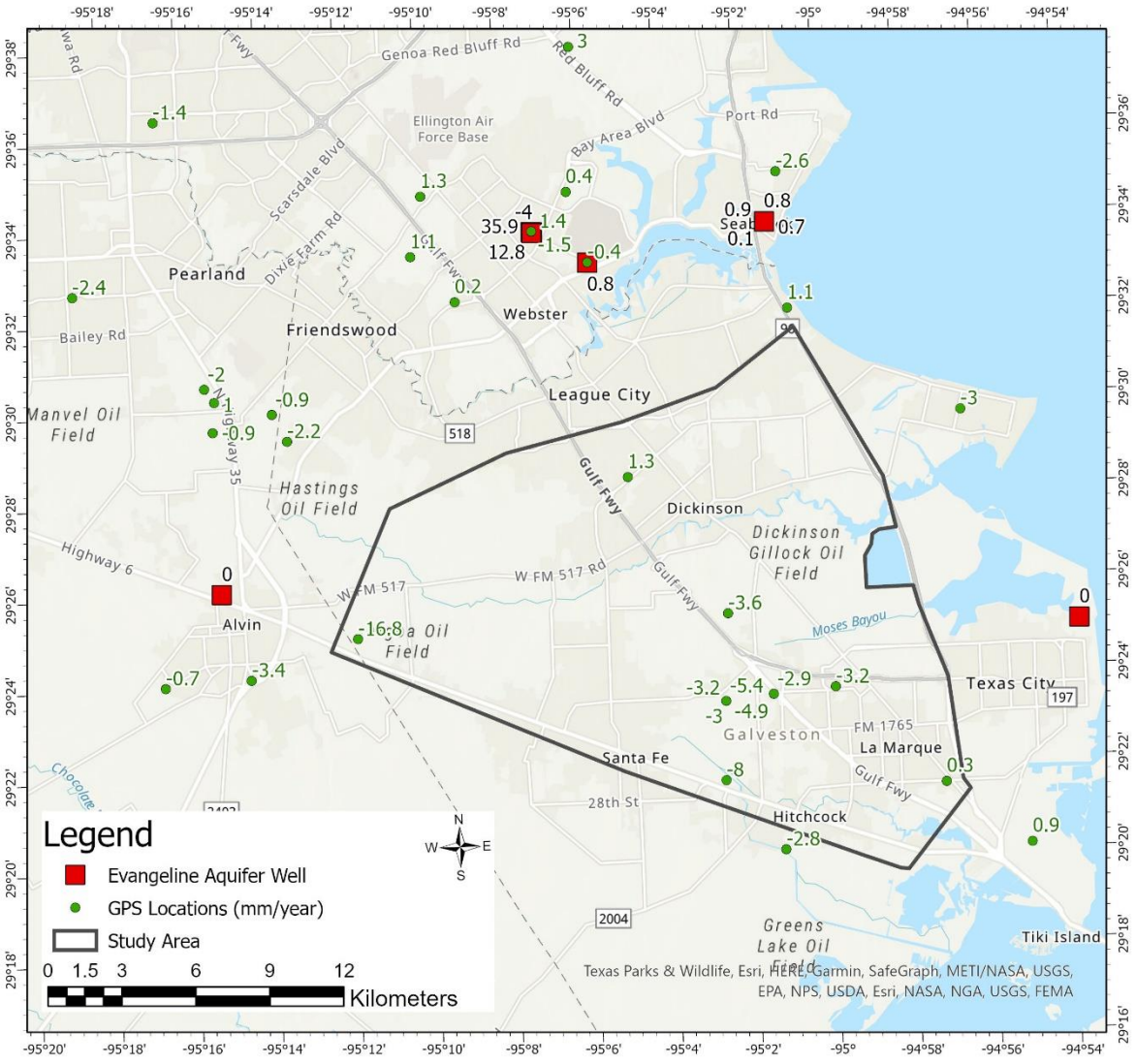

Figure A40: Change in hydraulic head levels of the Evangeline Aquifer between the years of 2019 and 2010 derived by finding the difference between the hydraulic head levels of 2019 and 2010. Points show the change in groundwater levels in the aquifer overlain on the current vertical GPS ground deformation trends. Aquifer contours display negative values representing a decrease in hydraulic head levels. Positive values represent an increase in hydraulic head levels. GPS negative values display subsidence while positive values display uplift or swell.

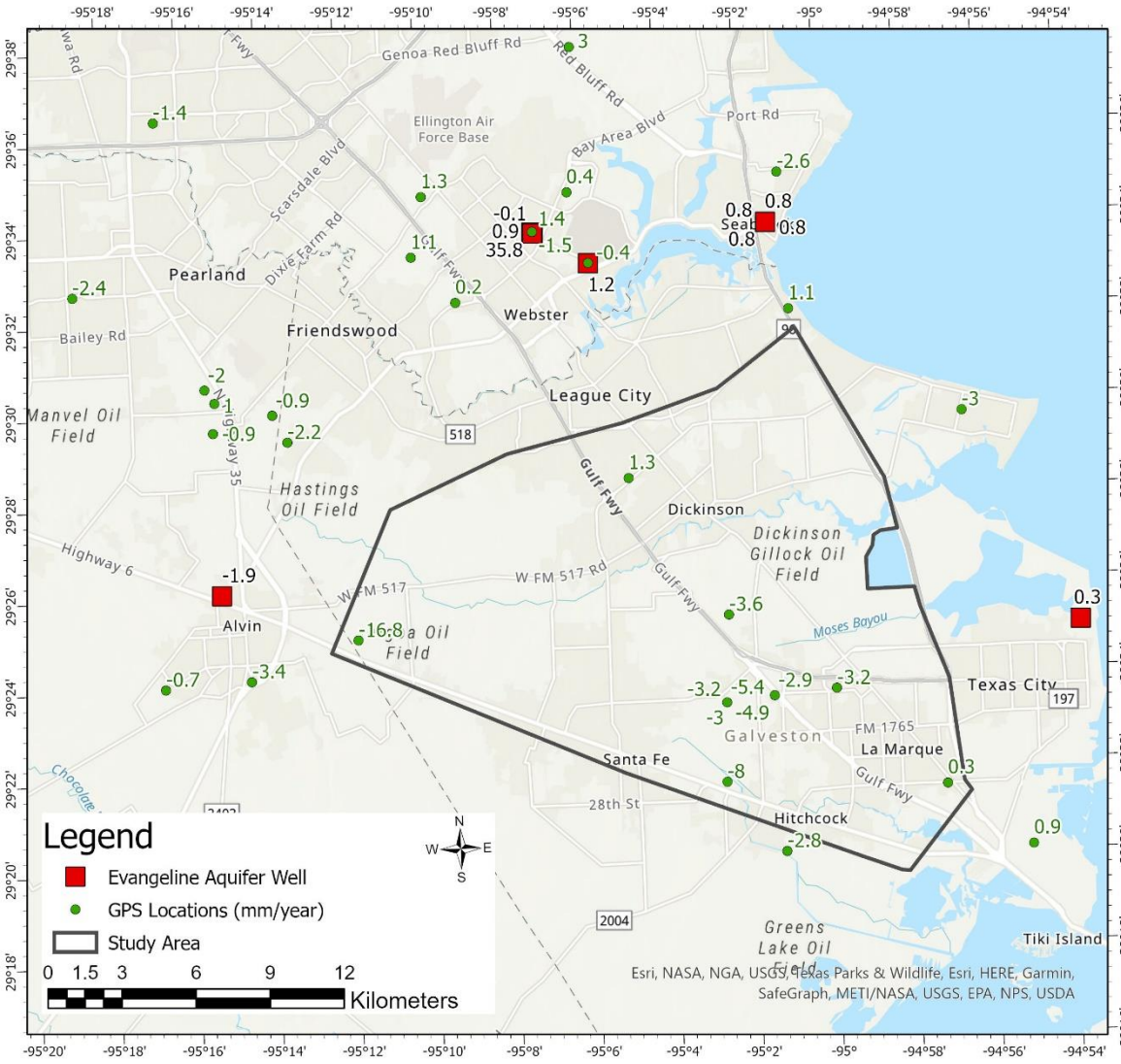

Figure A41: Change in hydraulic head levels of the Evangeline Aquifer between the years of 2019 and 2015 derived by finding the difference between the hydraulic head levels of 2019 and 2015. Points show the change in groundwater levels in the aquifer overlain on the current vertical GPS ground deformation trends. Aquifer contours display negative values representing a decrease in hydraulic head levels. Positive values represent an increase in hydraulic head levels. GPS negative values display subsidence while positive values display uplift or swell.

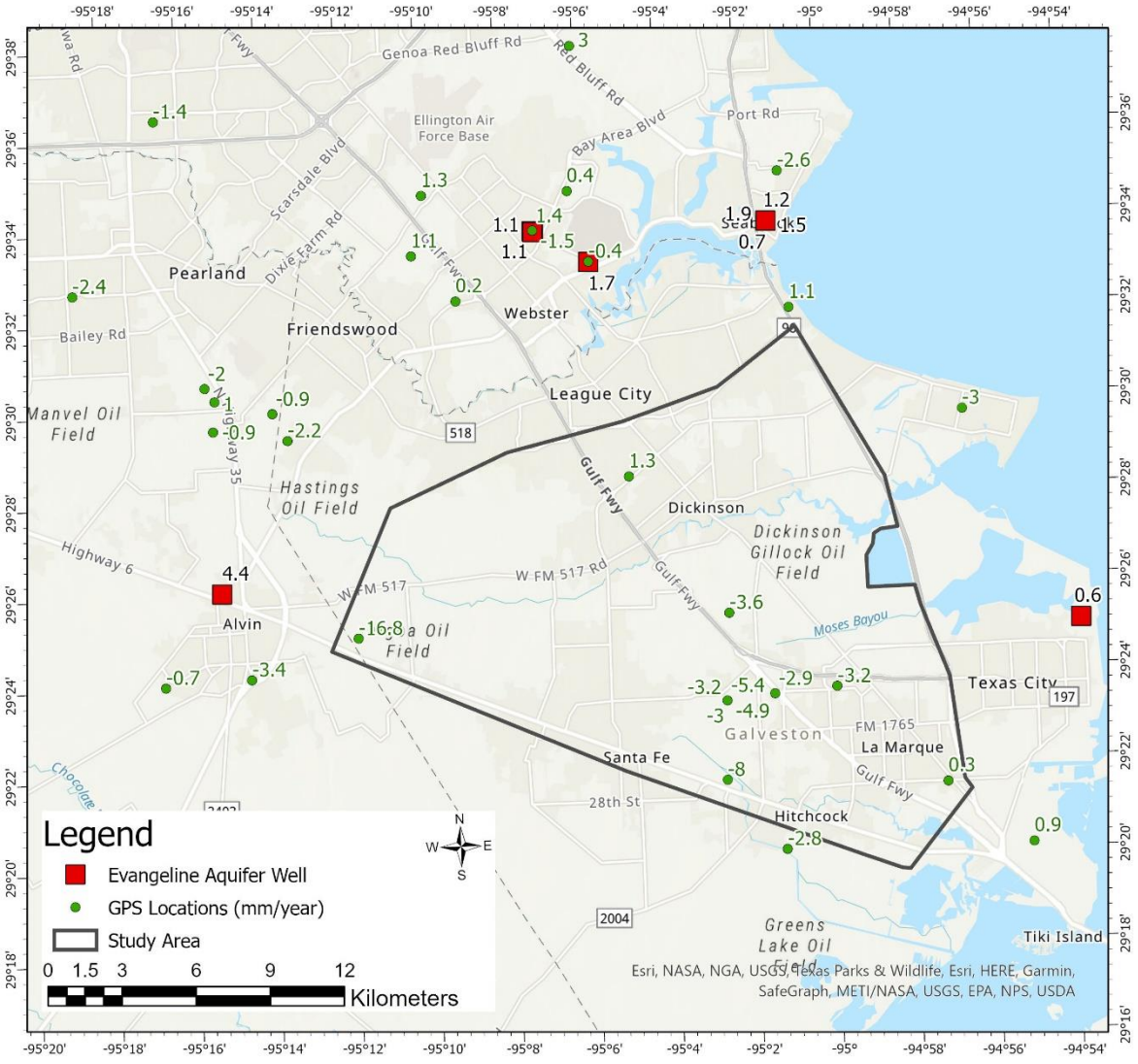

Figure A42: Change in hydraulic head levels of the Evangeline Aquifer between the years of 2010 and 2005 derived by finding the difference between the hydraulic head levels of 2010 and 2005. Points show the change in groundwater levels in the aquifer overlain on the current vertical GPS ground deformation trends. Aquifer contours display negative values representing a decrease in hydraulic head levels. Positive values represent an increase in hydraulic head levels. GPS negative values display subsidence while positive values display uplift or swell.

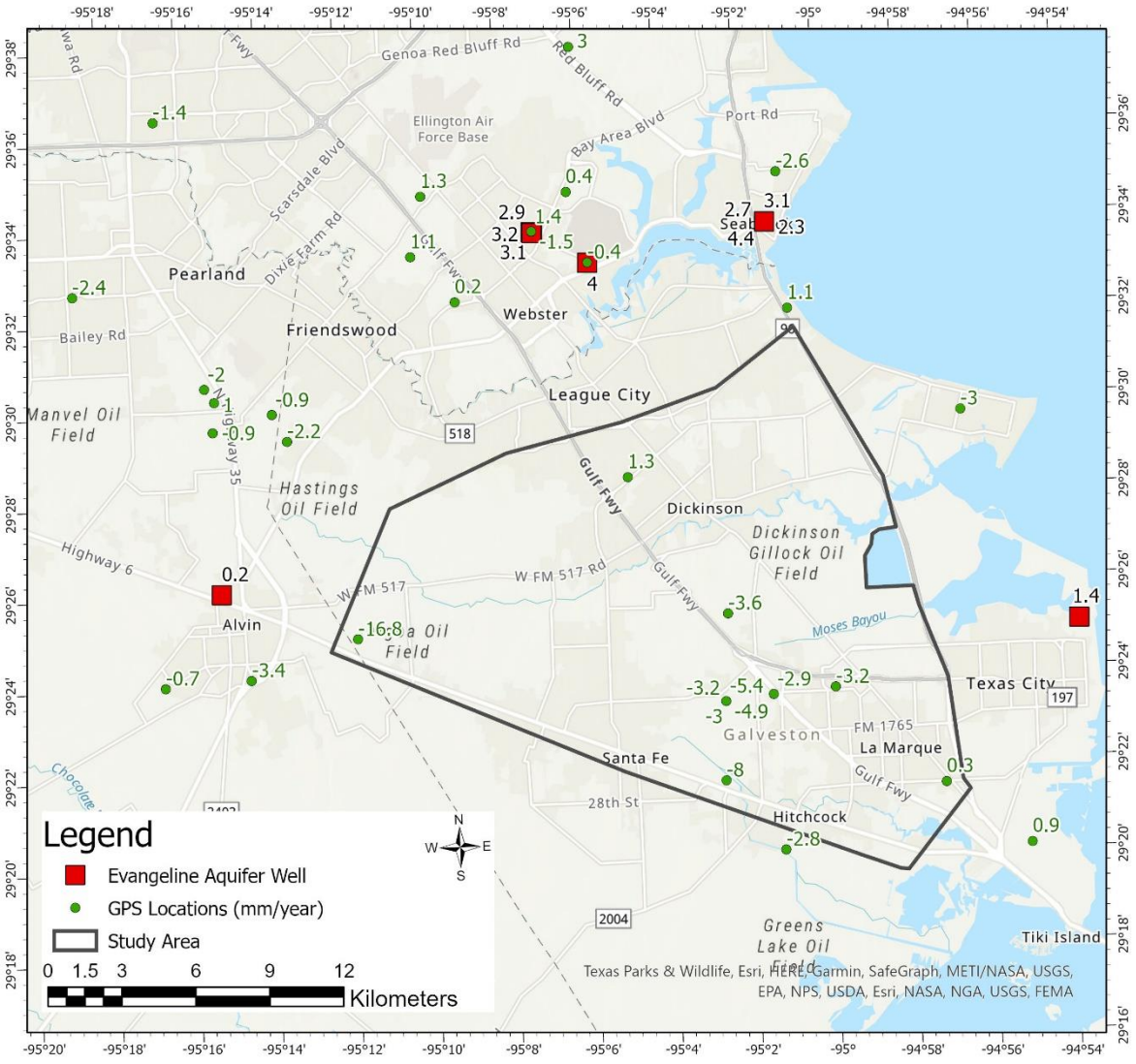

Figure A43: Change in hydraulic head levels of the Evangeline Aquifer between the years of 2005 and 2000 derived by finding the difference between the hydraulic head levels of 2005 and 2000. Points show the change in groundwater levels in the aquifer overlain on the current vertical GPS ground deformation trends. Aquifer contours display negative values representing a decrease in hydraulic head levels. Positive values represent an increase in hydraulic head levels. GPS negative values display subsidence while positive values display uplift or swell.

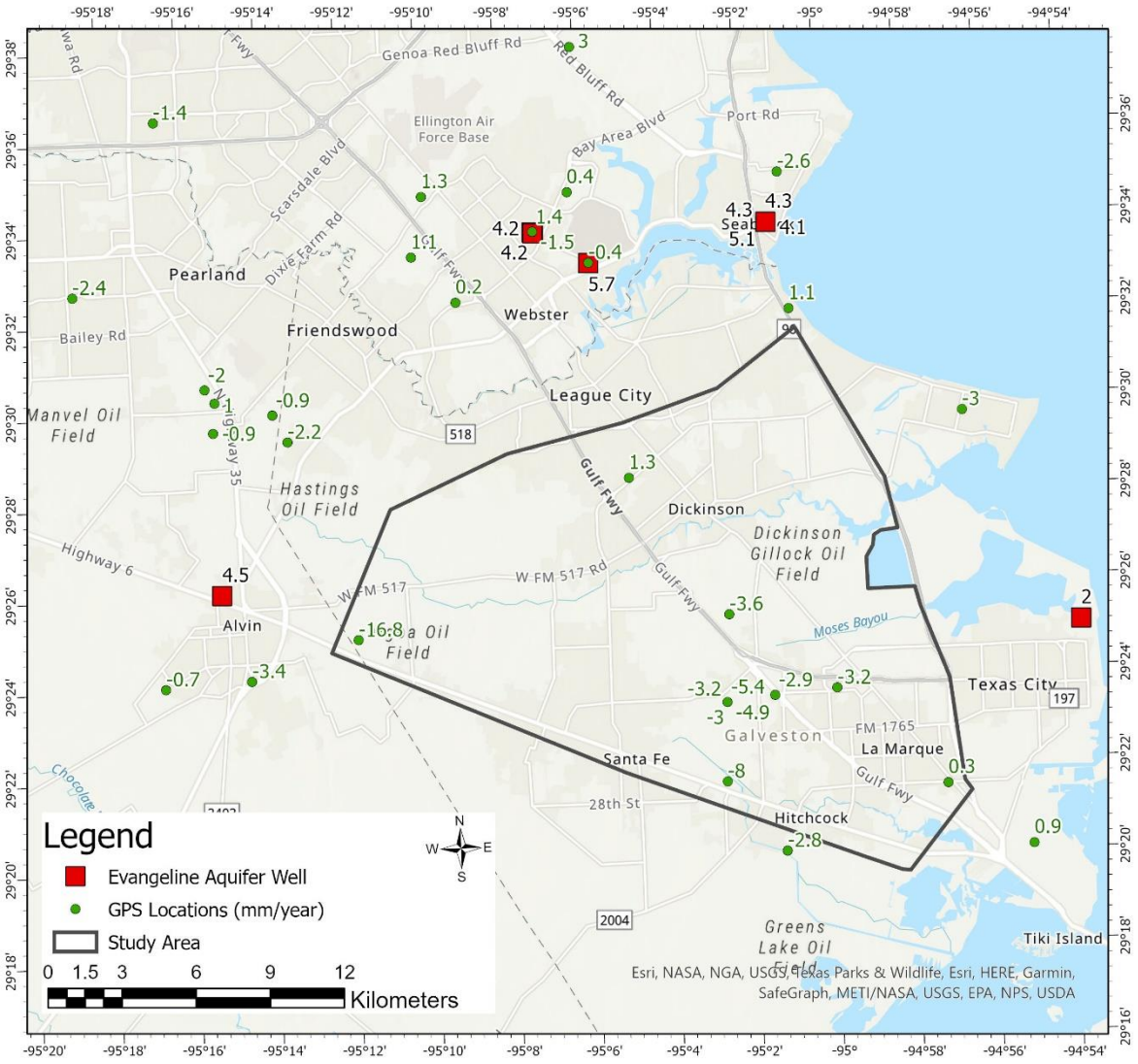

Figure A44: Change in hydraulic head levels of the Evangeline Aquifer between the years of 2010 and 2000 derived by finding the difference between the hydraulic head levels of 2010 and 2000. Points show the change in groundwater levels in the aquifer overlain on the current vertical GPS ground deformation trends. Aquifer contours display negative values representing a decrease in hydraulic head levels. Positive values represent an increase in hydraulic head levels. GPS negative values display subsidence while positive values display uplift or swell.